

# Deep Ultraviolet Photodetector: Materials and Devices

Wannian Fang<sup>1,2</sup>, Qiang Li<sup>1,2,\*</sup> , Jiaying Li<sup>2</sup>, Yuxuan Li<sup>2</sup>, Qifan Zhang<sup>2</sup>, Ransheng Chen<sup>2</sup>, Mingdi Wang<sup>2</sup>, Feng Yun<sup>2</sup> and Tao Wang<sup>3</sup> 

- <sup>1</sup> Key Laboratory of Physical Electronics and Devices for Ministry of Education and Shaanxi Provincial Key Laboratory of Photonics & Information Technology, Xi'an Jiaotong University, Xi'an 710049, China; wannian333@stu.xjtu.edu.cn
- <sup>2</sup> School of Electronic Science and Engineering, Xi'an Jiaotong University, Xi'an 710049, China; 1549159852@stu.xjtu.edu.cn (J.L.); masterleo@stu.xjtu.edu.cn (Y.L.); zqf951005@stu.xjtu.edu.cn (Q.Z.); chenransheng@stu.xjtu.edu.cn (R.C.); wangmingdi1999@stu.xjtu.edu.cn (M.W.); fyun2010@xjtu.edu.cn (F.Y.)
- <sup>3</sup> Department of Electronic and Electrical Engineering, University of Sheffield, Mappin Street, Sheffield S1 3JD, UK; t.wang@sheffield.ac.uk
- \* Correspondence: liqiang2014@mail.xjtu.edu.cn

**Abstract:** The application of deep ultraviolet detection (DUV) in military and civil fields has increasingly attracted the attention of researchers' attention. Compared with the disadvantages of organic materials, such as complex molecular structure and poor stability, inorganic materials are widely used in the field of DUV detection because of their good stability, controllable growth, and other characteristics. Rapid advances in preparing high-quality ultrawide-bandgap (UWBG) semiconductors have enabled the realization of various high-performance DUV photodetectors with different geometries, which provide an avenue for circumventing numerous disadvantages in traditional detectors. Herein, the development history and types of DUV detectors are briefly introduced. Typical UWBG detection materials and their preparation methods, as well as their research and application status in the field of DUV detection, are emphatically summarized and reviewed, including III-nitride semiconductors, gallium oxide, diamond, etc. Finally, problems pertaining to DUV detection materials, such as the growth of materials, the performance of devices, and their future development, are also discussed.

**Keywords:** ultrawide-bandgap semiconductor; deep ultraviolet photodetector; boron nitride; aluminum nitride; aluminum gallium nitride; gallium oxide; diamond



**Citation:** Fang, W.; Li, Q.; Li, J.; Li, Y.; Zhang, Q.; Chen, R.; Wang, M.; Yun, F.; Wang, T. Deep Ultraviolet Photodetector: Materials and Devices. *Crystals* **2023**, *13*, 915. <https://doi.org/10.3390/cryst13060915>

Academic Editor: Dmitri Donetski

Received: 31 March 2023

Revised: 8 May 2023

Accepted: 2 June 2023

Published: 5 June 2023



**Copyright:** © 2023 by the authors. Licensee MDPI, Basel, Switzerland. This article is an open access article distributed under the terms and conditions of the Creative Commons Attribution (CC BY) license (<https://creativecommons.org/licenses/by/4.0/>).

## 1. Introduction

Photodetectors are important photoelectric devices that realize sensing detection through photoelectric signal transformation and have been widely used in flame sensing, conversion communication, environmental monitoring, video imaging, night vision imaging, military tracking, medical detection, and other fields [1,2]. Ultraviolet with a wavelength less than 280 nm is defined as a deep ultraviolet band that will be absorbed by ozone in the atmosphere before entering the earth. Almost no signal background exists in this band on the earth, which is also called a solar-blind band. The application fields represented by ultraviolet short-range secure communication, shipborne guidance, ozone layer monitoring, and water pollution treatment need the continuous development, maturity, transformation, and application of deep ultraviolet (DUV) detection technology. Therefore, further research and development of DUV detection technology have attracted the extensive attention of researchers in relevant fields, whether in daily life or in the construction of modern national defense.

Traditionally, the detection of DUV light is achieved by photomultiplier tubes (PMTs), thermal detectors, narrow-bandgap semiconductor photodiodes, or charge-coupled devices (CCDs) [3–6]. The biggest advantage of PMTs is that they are very sensitive to ultraviolet photons and invisible for wavelengths that are greater than their response cutoff edge. However, because of their large volume and weight and the need for high voltage (more

than 100 V) as a support when working, they exhibit relatively high power consumption, making them an inconvenient ultraviolet detection method. Pyrometers and bolometers in thermal detectors are usually used for the calibration of DUV areas and have also proved to be as useful as absolute radiometric standards. However, they are not suitable for fast-response and wavelength-selective DUV detection. In contrast, semiconductor photodiodes and CCDs can operate only with moderate voltage, and more importantly, small, portable, and low-cost semiconductor photodiodes usually show good linearity, sensitivity, and high-speed operation capabilities [6]. Despite these outstanding characteristics, it is undeniable that these devices also have their own shortcomings. For example, the band gap of silicon materials is 1.12 eV. Therefore, when used for DUV detection, expensive gratings are needed to block visible light and infrared light, which leads to a significant loss of the effective area of the system and greatly increases the cost.

Compared with narrow-bandgap materials, the optical response wavelength of detectors made of new ultrawide-bandgap (UWBG) semiconductor materials is naturally located in the deep ultraviolet band, so the expensive filter structure is not needed. In addition, these UWBG semiconductors normally have the advantages of good thermal conductivity, high sensitivity, and strong chemical stability. At present, inorganic materials used for DUV detection mainly include III-nitride semiconductors, diamond, and other materials. Each material has its own advantages and disadvantages, and the important parameters of these materials are listed in Table 1.

**Table 1.** Important parameters of different UWBG semiconductor materials [7,8].

Material	$E_g$ (eV)	Thermal Conductivity ( $W\ cm^{-1}\ K^{-1}$ )	Melting Point (K)	Electron Saturation Velocity ( $10^7\ cm\ S^{-1}$ )	Mobility ( $cm^2\ V^{-1}\ S^{-1}$ ) Electrons/Holes	Dielectric Constant	Break Down Field ( $10^5\ V\ cm^{-1}$ )
Si	1.12	1.5	1683	1	1400/600	11.8	3
AlN	6.2	3.19	>2400	1.4	135/14	8.1	20
AlGaN	3.4–6.2						
BN	5.9	2.35 in plane $2.3 \times 10^{-2}$ out of plane	2970		-/35 in plane	6.85 in plane 5.06 out of plane	80
Ga <sub>2</sub> O <sub>3</sub>	4.9	0.27		2	300/-	10	80
Diamond	5.5	20	3773	2.7	2200/1600	5.5	100

Photodetectors can generally be divided into the following types: photoconductive detectors, photovoltaic detectors, and phototransistors [5,6]. These types of detectors are based on different operating principles and have their own advantages. Basic photoconductive detectors are formed by using the photoconductive material as the channel and placing the metal with Ohmic contact as the electrode at both ends of the channel. Additionally, there is often a light gain mechanism, that is, a type of charge carrier that can cycle through the external circuit many times before recombining the carrier with the opposite charge type, resulting in an increase in photocurrent and a decrease in response speed [5]. Photovoltaic detectors mainly include MSM type, Schottky barrier type, and p-n (p-i-n) junction type [9]. MSM detectors are made up of double “back-to-back” semiconductor Schottky barriers by using an interdigitated electrode with planar linearity on top of an active light collection region. When under DC bias, one of the Schottky barriers will be forward biased and the other reverse biased, so the dark current is quite small. Due to the low capacitance per unit area and limited transit time, MSM photodiodes also have an intrinsic rapid response ability. Schottky detectors consist of a semitransparent Schottky contact and an Ohmic contact and have many advantages, such as high responsivity, high quantum efficiency, low dark current, short response time, and possible zero-bias operations. The p-n (p-i-n) junction type shares some similarities with Schottky photodiodes in that both devices exploit the photovoltaic effect. When forward bias is applied in the p-n

junction, the dark current is far greater than the photocurrent, and the detector is unable to work due to unilateral conductivity characteristics. Under reverse bias, the dark current is suppressed, and moreover, the carrier transit time and diode capacitance are reduced, which is beneficial to the improvement of sensitivity [10,11]. Phototransistors are special photoconductive detectors that separate the photoconductive material of the detector from the grid with a thin dielectric layer. The applied grid voltage can adjust the carrier density through the field effect and can make the dark current of the device in the “off” state [12,13]. The schematic structure of these devices is illustrated in Figure 1.

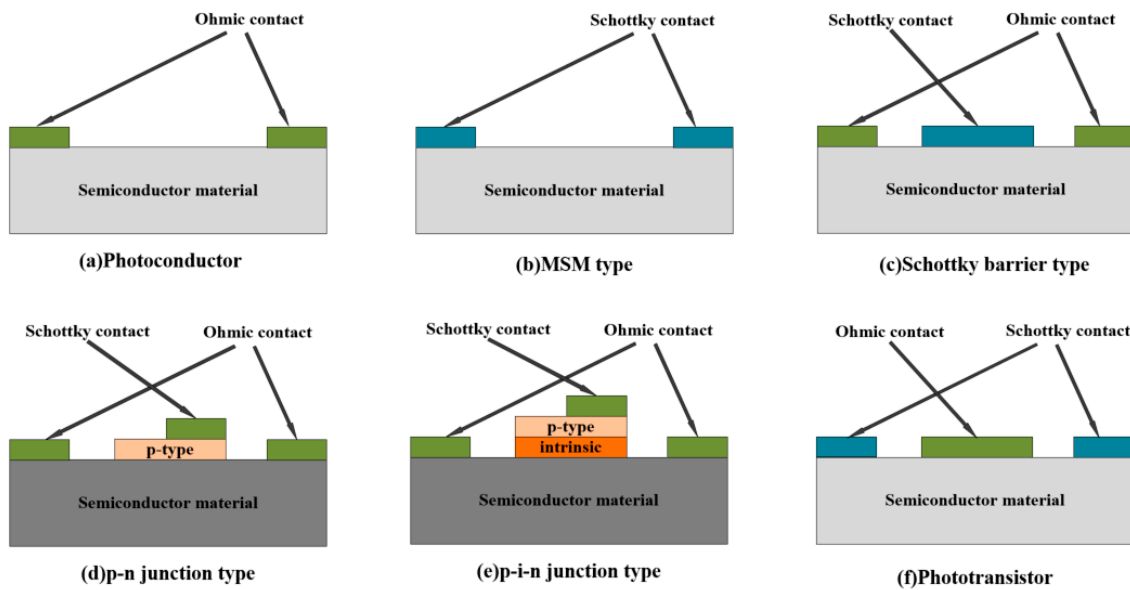


**Figure 1.** Schematic structure of the different types of wide-bandgap semiconductor UV detectors: (a) Photoconductor; (b) MSM type; (c) Schottky barrier type; (d) p-n junction type; (e) p-i-n junction type; (f) Phototransistor.

In order to characterize the performance of DUV photodetectors with different materials and structures, the important parameters are summarized in Table 2 [5]. High-performance ultraviolet detectors need to have high responsivity, quantum efficiency, and response speed, as well as a signal-to-noise ratio. The performance of the detector mainly depends on the inherent performance of its material. The ability of a material to convert optical signals into electrical signals is determined by the generation, separation, transmission and recombination of its internal electron–hole pairs.

**Table 2.** Performance parameters of deep ultraviolet photodetector [5].

Quantity	Symbol	Unit	Definition
Responsivity	R	$A W^{-1}, V W^{-1}$	The ratio of photogenerated current or voltage to the incident light power
External quantum efficiency/internal quantum efficiency	EQE/IQE	/	In a photodiode, the ratio of the recombination number of electron–hole pairs that generate photocurrent to the number of incident/absorbed photons
Photoconductive gain	G	/	In a photoconductor, the ratio of the number of electrons collected by the electrode to the number of incident photons
Dark current	$I_{dark}$	A	Current flowing in the photodetector without light

Table 2. Cont.

Quantity	Symbol	Unit	Definition
Response speed	$\tau_r/\tau_d$	s	Rise time ( $\tau_r$ ) and decay time ( $\tau_d$ ) are defined as the time needed for the photoresponse to increase from 10% to 90% or drop from 90% to 10% of its peak value
Noise current	$I_{\text{noise}}$	A Hz <sup>-1/2</sup>	The random root means square fluctuation in current when bandwidth is limited to 1 Hz
Noise-equivalent power	NEP	W Hz <sup>-1/2</sup>	The minimum impinging optical power required to achieve a signal-to-noise ratio of unity in a 1 Hz bandwidth
Specific detectivity	$D^*$	cm Hz <sup>-1/2</sup> W <sup>-1</sup> /Jones	A parameter for comparing the sensitivity between photodetectors with different device area A and bandwidth B. $D^* = (AB)^{-1/2}/\text{NEP}$
Response rejection ratio	$R_a/R_b$	/	The ratio between responsivity at light wavelength-a and that at light wavelength-b

This paper mainly focuses on the research of DUV detection materials, briefly introduces the development history and types of DUV photodetectors, and emphatically summarizes the preparation methods of DUV detection materials and their applications in the field of detection. Some problems existing in DUV detection materials at present are put forward, and future development is also discussed and prospected.

## 2. DUV Photodetectors Based on Boron Nitride Material

Hexagonal boron nitride (h-BN) has been researched for more than one century. The structural and physical properties of h-BN have been investigated before cubic BN (c-BN) and wurtzite BN. Graphite-like h-BN and diamond-like c-BN phases were brought about by  $sp_2$  and  $sp_3$  hybridization of the chemical bonding of both atomic species, respectively [8].

In fact, h-BN material is very suitable for making DUV detectors because of its extraordinary physical properties, including wide band gap (~6 eV), high-temperature stability, large thermal conductivity, high band-edge absorption coefficient ( $7.5 \times 10^5 \text{ cm}^{-1}$ ), and low dielectric constant. The main challenge in the development of h-BN-based DUV photodetectors is the significant difficulties in obtaining high-quality h-BN films [14,15].

### 2.1. BN Nanostructures

Nanometer boron nitride materials have different forms, such as nanotubes, nanoparticles, nanobelts, nanosheets, nanofibers, nanowires, etc. Among them, boron nitride nanosheets (BNNSs) with a structure similar to graphene have excellent optical properties and are suitable for making deep ultraviolet emitters and various optoelectronic nanodevices [16]. Compared with chemical vapor deposition (CVD), the pulsed laser deposition (PLD) technique can greatly avoid pollution or internal stress during the synthesis of crystalline BNNSs [17,18]. High-quality crystalline BNNSs for UV detection are mostly grown on silicon wafers or molybdenum substrates by the PLD technique [18–24].

Photoconductors based on BNNSs have attracted much attention for their simple device structure and convenient preparation process [19–22]. Sajjad et al. reported the synthesis of some atomic-layer BNNSs using the  $\text{CO}_2$ -PLD technique and their application for deep ultraviolet photodetection [19]. At 300 K, a single sharp excitonic peak centered at 233 nm appeared during cathodoluminescence (CL) spectroscopy, as shown in Figure 2a. The initial experimental tests and typical responses of the developed prototype BNNS-based photoconductor were shown in Figure 2b,c, respectively. In another study, the same group optimized the PLD method to synthesize high-quality single-crystal BNNSs [20]. The dark current of BNNS-based UV photoconductors was less than 0.4 nA at 50 V and 3 nA at 200 V. The quick response time dropped to 0.6 ms, and the visible rejection ratio was up to  $10^8$ . Aldalbahi et al. synthesized 2D boron nitride/tungsten nitride (BN-WN) nanocomposites for tunable bandgap structures and devices [21]. The responsivity and the

response time of the DUV photodetectors based on these nanocomposites were 1.17 A/W and lower than 2 ms, respectively.

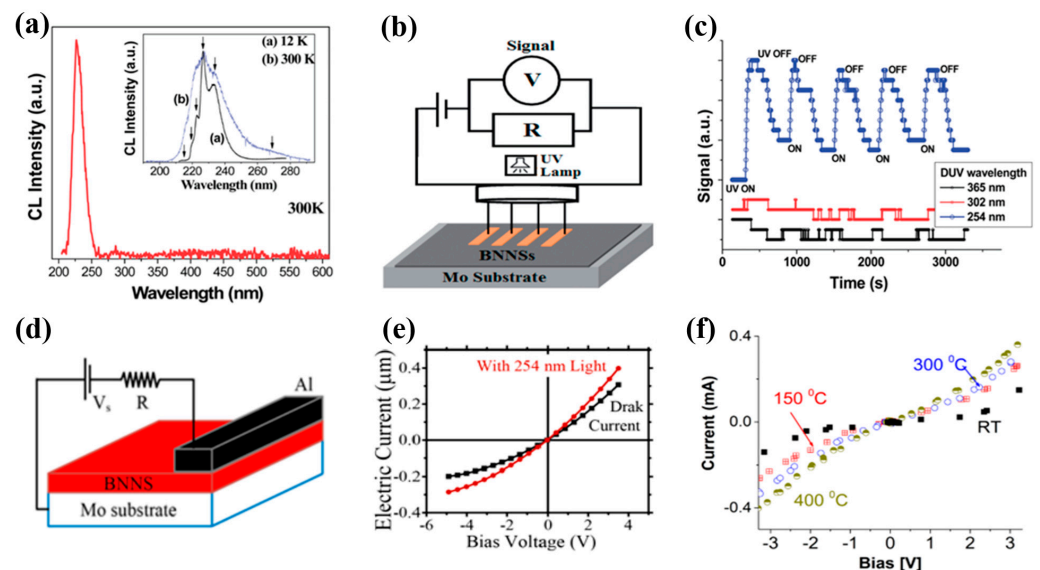


**Figure 2.** (a) CL spectrum of BNNSs. Inset shows results between normalized DUV CL spectra of BNNSs measured at 12 K—(a) and 300 K—(b). (b) Electrical circuit diagram for DUV tests. (c) Typical responses of a BNNS-based DUV photodetector prototype [19]. Vertical structure MSM BNNS DUV photodetector: (d) schematic structure; (e) electric current as a function of bias voltage [23]. (f) Measured dark current as a function of applied bias voltage at different temperatures [24].

Zhou et al. fabricated a vertical metal–semiconductor–metal (MSM) structure of a solar-blind DUV photodetector based on BNNSs, as shown in Figure 2d [23]. The dark current was less than 300 nA at 4 V (Figure 2e). When UV light was applied with an intensity of  $1.0 \text{ mW/cm}^2$ , a responsivity of  $1.5 \text{ mA/W}$  at  $-5 \text{ V}$  bias was obtained with an active surface area of  $\sim 20 \text{ mm}^2$ . Rivera et al. used BNNSs as a sensing material for planar MSM photodetectors (PDs) by exploring the energy bandgap shift in a new BNNS arrangement on a silicon substrate [24]. The BNNS material exhibited high conductivity and photosensitivity in the DUV region and was also sensitive to the UVB region, indicating a lower bandgap width than that of bulk or thin films. Even at temperatures as high as  $400 \text{ }^\circ\text{C}$ , the DUV photodetector performed extremely well, as shown in Figure 2f, making it an ideal candidate for UV sensing in high-temperature environments. Self-powered DUV photodetectors based on high-quality BNNSs with Schottky contact structures were designed and fabricated [18]. The Schottky photodetector demonstrated to possess excellent performance, including low dark current ( $0.4 \text{ nA}$ ), high responsivity ( $296 \text{ mA/W}$  at  $0 \text{ V}$ ), and high stability. In addition, the effect of plasma treatment on the induced photocurrent response of the detector was also studied. It can be found from the experimental data that plasma treatment significantly improved the induced photocurrent and response time.

## 2.2. BN Thin Films

Photodetectors based on h-BN films have been widely studied by many groups, among which MSM devices account for a large proportion due to their intrinsic lower dark current and faster response speed. The film preparation method for ultraviolet detection so far includes ion-beam sputtering deposition (IBSD) [14,25–27], mechanically exfoliated [28,29], low-pressure chemical vapor deposition (LPCVD) [30], atmospheric-pressure chemical vapor deposition (APCVD) [31–33], metal–organic chemical vapor deposition (MOCVD) [34], metal–organic vapor phase epitaxy (MOVPE) [35], and magnetron sputtering [36].

IBSD is a mature industry technology with good compatibility and standard semiconductor manufacturing processes. Liu et al. synthesized two-dimensional (2D) h-BN on Cu

foils with controllable layers by IBSD [14]. From the Raman spectra in Figure 3a, the lower density of domain boundaries and higher crystalline quality of the h-BN layers could be obtained by a higher substrate temperature. DUV photodetectors showed a high on/off ratio of  $>10^3$  under 212 nm light, which were fabricated from the transferred h-BN layers on SiO<sub>2</sub>/Si substrates (Figure 3b,c). Gao et al. grew wafer-scale 2D h-BN layers directly on catalyst-free sapphire substrates through IBSD [25]. The N-terminated sapphire surface formed by the surface nitridation process can promote the nucleation of h-BN, while N<sup>+</sup> sputtering with IBSD can make up for the deficiency of N. The photoconductive detector based on high-quality h-BN layers with Ti/Au electrodes exhibited better performance, with a high on/off ratio of 6800, a detectivity exceeding  $1.8 \times 10^{10}$  Jones, and a fast response time of  $\sim 1$  ms. Li et al. attempted the direct growth of h-BN films on silicon, sapphire, and quartz substrates by IBSD at the temperature of  $\sim 500$  °C without a catalyst [27]. The fabricated h-BN thick films were smooth and continuous without obvious pinholes and cracks. The DUV photodetector with a 500 nm thick h-BN film on a quartz substrate exhibited a high responsivity of  $0.5 \text{ A W}^{-1}$  and a large specific detectivity of  $6.92 \times 10^9$  Jones.

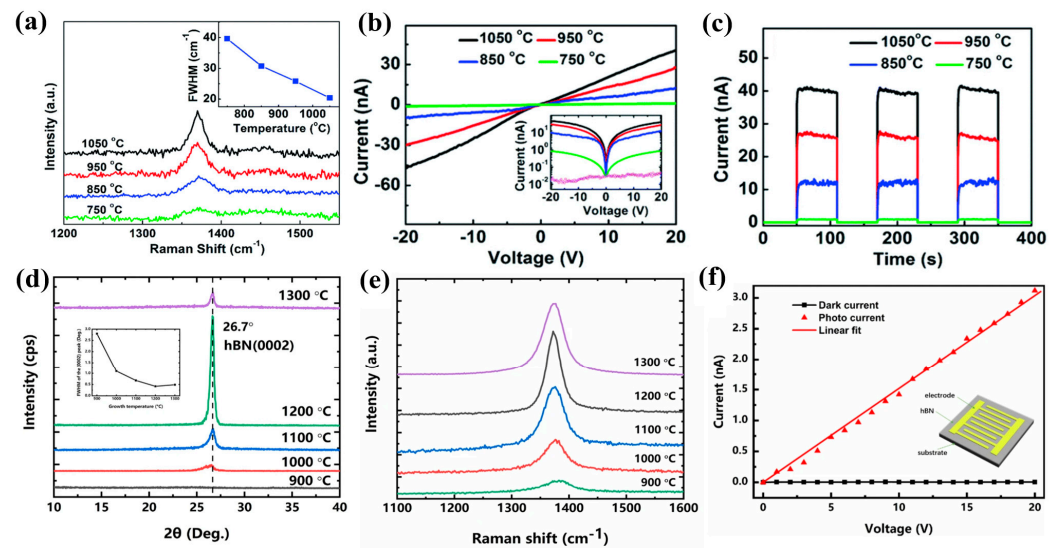


**Figure 3.** (a) Raman spectra of the h-BN films with different substrate temperatures. Inset shows the FWHM of the h-BN Raman peak as a function of the substrate temperature. (b) I–V curves of the photodetectors fabricated from the h-BN layers with different substrate temperatures ( $212 \text{ nm}$ ,  $1.59 \text{ mW mm}^{-2}$ ). Inset shows the logarithmic scale of I–V curves. (c) I–t curves of the photodetectors with different substrate temperatures, measured at  $20 \text{ V}$  under  $212 \text{ nm}$  laser irradiation [14]. (d) XRD patterns of h-BN films deposited by LPCVD on silicon substrates at different temperatures. Inset shows the dependence of the FWHMs of the (0002) peaks on the growth temperature. (e) Raman spectra of the h-BN samples at various deposition temperatures. (f) I–V characteristics of the intrinsic h-BN photodetector ( $2.3 \mu\text{m}$  thick) measured at room temperature in dark and under UV-enhanced. Inset shows the schematic view of h-BN MSM photodetector [30].

In addition to photoconductive devices, MSM devices based on h-BN films have been widely studied [26,28–31]. For instance, Zhang et al. used an electrode at the bottom of a thin layered h-BN [28], which solved the contradiction between the electrode area and the photosensitive area. The device exhibited excellent performance in specific detectivity, exceeding  $3.68 \times 10^8$  Jones at  $215 \text{ nm}$ . Zheng et al. fabricated a high-performance MSM-structured 2D few-layered h-BN photodetector, which showed extremely high vacuum ultraviolet (VUV) response selectivity ( $R_{160}/R_{250}$  was up to  $10^4$ ) [29]. Typically, it presented high sensitivity (EQE = 2133%, at  $20 \text{ V}$ ) under the extremely weak  $160 \text{ nm}$  light of  $3.25 \text{ pW}$ . This photoresponsivity was attributed to the high carrier collection efficiency and existing surface trap states of few-layer h-BN.

Wafer-scale growth of h-BN films is crucial for industrial applications. CVD is a promising method to grow continuous h-BN thin films with high crystallinity at a reasonable cost [15,30,31,37]. For instance, Chen et al. successfully prepared c-axis-oriented polycrystalline h-BN films with a micrometer-scale thickness on (100) silicon substrates by LPCVD [30]. X-ray diffraction (XRD) and Raman spectra (Figure 3d,e) were used to investigate the effect of temperature on the crystalline quality of the h-BN films, which indicated that the stoichiometric polycrystalline h-BN films were synthesized at 1200 °C. A DUV photodetector was fabricated on h-BN film with a thickness of 2.3 μm, which exhibited a photo-to-dark-current ratio of ~312 at 20 V bias under the light of 224 nm (Figure 3f). Feng et al. proposed a method to prepare h-BN thin films by APCVD [31]. Samples with a size of several hundred micrometers were obtained, which were much larger than the previously reported results via the same method. Large-area, clean, and homogeneous two-dimensional multilayer h-BN films with different thicknesses have been prepared on Au foils by APCVD [32]. This sensitive solar-blind h-BN photodetector exhibits ultrahigh rejection ratios ( $R_{220\text{nm}}/R_{280\text{nm}} > 103$  and  $R_{220\text{nm}}/R_{290\text{nm}} > 104$ ), a low dark current (102 fA), and a large detectivity ( $3.9 \times 10^{10}$  Jones).

Flexible electronics are expected to play a key role in connecting human life with multi-functional intelligent electronic devices due to their adaptability to different shapes, surfaces, and even the human body. Li et al. fabricated MSM devices based on 1~2.5 μm thick BN layers grown by MOVPE on 2-inch sapphire substrates [35]. The detector showed a low dark current of 2 nA under 100 V and a  $100 \pm 20\%$  photoconductivity yield for DUV light illumination, which presented great potential for the development of flexible (opto-)electronics in the future. Veeralingam et al. synthesized high-purity 2D h-BN nanosheets by a one-step solid-state reaction and drop-casted them onto Cu(111) [38]. From the photocurrent density vs. voltage curve depicted in Figure 4a, the rectifying behavior from the Schottky junction can be observed at the interface of h-BN and copper. Figure 4b shows the trend in the rise and fall of the photocurrent for successive on/off cycles, and Figure 4c indicates the stable response to different bending times. The results illustrate good switching behavior and flexible durability featuring the repeatability of the device response to light. Moreover, the as-fabricated Schottky photodetector exhibited a responsivity of 5.022 A/W, a quantum yield of 2945%, and a specific detectivity of  $6.1 \times 10^{12}$  Jones. Because of traditional plastic or paper substrates with low thermal conductivity, thermal management issues found in most flexible devices have become crucial for large-scale integration or high-temperature applications [39]. Lin et al. used nanopaper with high thermal conductivity as a substrate by applying 2D h-BN nanosheets and 1D nanofibrillated cellulose on it to form a flexible DUV photodetector. Figure 4d shows the schematic of the fabrication process [40]. The devices demonstrated a superior photodetectivity of  $8.05 \times 10^{10}$  cm Hz<sup>1/2</sup>/W, a short response time of 0.267 s, and stable photoelectric characteristics under different bending conditions (Figure 4e). Due to the thermal conductivity of boron nitride paper being much higher than that of plastic/paper substrates, the photodetectors could operate at high temperatures up to 200 °C with good response (Figure 4f).

In general, chemical doping is regarded as the most effective and feasible approach for tailoring the properties of semiconductors. Carbon (C) is a very suitable dopant for h-BN since it is a perfect match in the lattice and bond length between h-BN and carbon. Through controlling the sputtering atmosphere, Wang et al. synthesized h-BN atomic layers with various C concentrations varying from 0 to 10.2 at% [26]. The h-BN phase remained stable when a small amount of C was incorporated into the h-BN layer, the crystalline quality of which was degraded with simultaneous replacement by a boron carbon nitride (h-BCN) alloy (Figure 5a). Furthermore, DUV PDs based on BCN layers were fabricated, and the h-BN-based PD with 7.5 at% C exhibited the best performance with a responsivity of  $9.2 \text{ mA} \cdot \text{W}^{-1}$ . These results were significantly higher than the performance of the intrinsic h-BN device (Figure 5b,c). Prakash et al. presented a metal–insulator–metal

(MIM) structure using BCN [36]. A higher (100 times the dark current) UV photocurrent was achieved in the range of  $-3$  to  $3$  V.

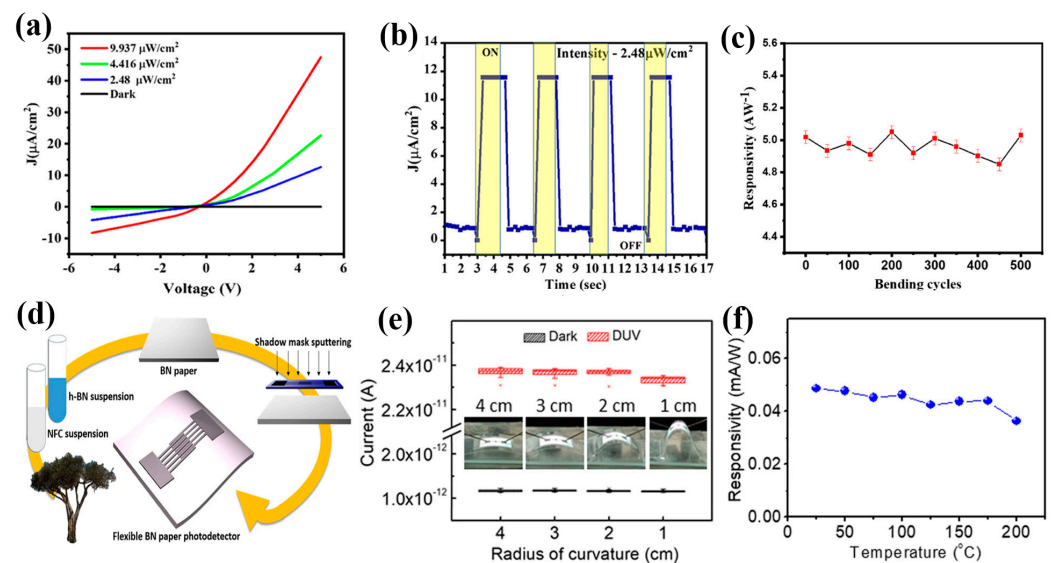


**Figure 4.** (a) Current density–voltage curve of the h-BN DUV photodetector under dark and a 210 nm DUV lamp. (b) Temporal (I–T) response of the h-BN photodetector at 5 V. (c) Responsivity under different bending cycles of the h-BN/Cu device [38]. (d) Schematic of the fabrication process of the flexible BN paper PD. (e) Current distribution of a BN paper PD in different radius of curvature. Inset shows the actual bending images. (f) Responsivity with different temperatures under 185 nm DUV light at an intensity of  $15.28 \text{ mW}/\text{cm}^2$  and 10 V bias [40].

Pure c-BN films have been produced by a variety of methods [41,42]. Deposition of c-BN by the PVD method is the most common, but it leads to induced stress and delamination, limiting the thickness of the grown film. The application of fluorine chemistry can increase the film thickness to  $20 \mu\text{m}$  with a crystallite size of several microns and lower defect density. DUV MSM PDs based on high-quality c-BN films presented a peak responsivity at 180 nm and showed a very sharp cutoff wavelength at 193 nm. The PD revealed a visible rejection ratio (180 nm vs. 250 nm) of more than  $10^4$  [43]. The characteristics of photodetectors exhibited an extremely low dark current, a high breakdown voltage, and high responsiveness, suggesting that c-BN films are very promising for DUV sensing.

### 2.3. BN Heterostructures

Mballo et al. reported the fabrication and application of Mg-doped h-BN layers. The effect of different bis cyclopentadienyl-magnesium ( $\text{Cp}_2\text{Mg}$ ) molar flow rates on Mg incorporation in h-BN was studied. A single (002) peak of h-BN appeared clearly during XRD, and the full width at half maximum (FWHM) increased with Mg doping, as shown in Figure 5d. The Mg doping concentration was up to  $4 \times 10^{18}/\text{cm}^3$  in h-BN from secondary ion mass spectrometry, which led to the electrical conductivity increasing. Mg-doped h-BN/n-type AlGaIn heterostructures were fabricated, the I–V characteristics of which revealed rectifying behavior for temperatures from 123 K to 423 K (Figure 5e). A built-in potential of 3.89 V (Figure 5f) was obtained from the C–V measurements [44].

In conclusion, the research on BN-based DUV photodetectors mainly focuses on two-dimensional nanosheets and thin-film morphology, mostly adopting photoconductive and MSM structures. There are few reports on heterostructures and p–n (p–i–n) devices at present. Table 3 summarizes the performance parameters of h-BN-based DUV photodetectors, such as dark current, on/off ratio, rejection ratio, responsivity, response time, etc.

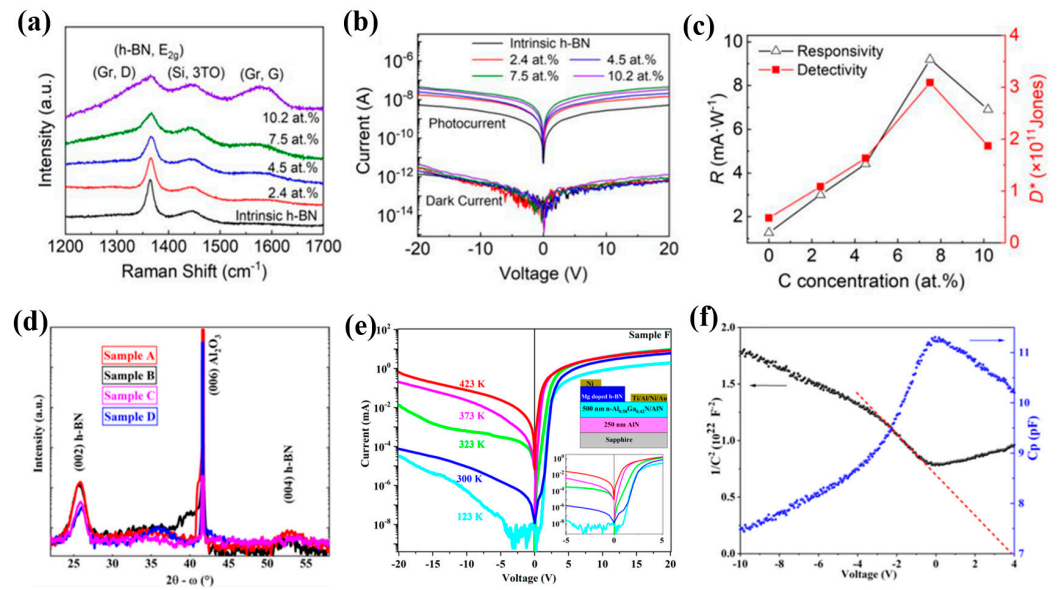


**Figure 5.** (a) Raman spectra of the intrinsic h-BN and the different doping concentrations of h-BN. (b) Semilogarithmic I–V curves of the photodetectors based on h-BN layers with different C concentrations in the dark and under the  $15.9 \text{ mW cm}^{-2}$  laser irradiation. (c) Relationship between the concentration C and the responsivity R or specific detectivity  $D^*$  at 20 V [26]. (d) HR-XRD spectra of the grown h-BN samples. (e) I–V characteristics of Mg-doped BN/n- $\text{Al}_{0.58}\text{Ga}_{0.42}\text{N}$  heterojunction measured at different temperatures. Inset: structure of the heterojunction. (f) Capacitance and  $1/C^2$  plot vs. voltage in Mg-doped h-BN/n- $\text{Al}_{0.58}\text{Ga}_{0.42}\text{N}$  (1 MHz and room temperature) [44].

**Table 3.** Summary of performance parameters of DUV photodetectors based on h-BN.

Device Structure	Fabrication Method	Light Detection/nm	Dark Current	On/Off Ratio	Rejection Ratio	Specific Detectivity/Jones	EQE	Responsivity	Rise Time/Decay Time	Ref.
BNNS Photoconductor	PLD	254	<0.4 nA @50 V		UV/vis	$10^8$			0.6 ms/1.8 ms	[20]
BN-WN nanocomposites Photoconductor	PLD	250						1.17 A/W @2 V	<2 ms	[21]
BNNS MSM	PLD	254	−200 nA					1.5 mA/W @−5 V		[23]
BNNS MSM	PLD	250						9 $\mu\text{A/W@0 V}$		[24]
BNNS Schottky	PLD	250	0.4 nA		250/350	160~200		296 mA/W @0 V	1.6 s/17 s	[18]
BN Nanopaper	-	185							0.267 s/0.393 s	[40]
BN film Photoconductor	IBSD	212						1.33 mA/W @25 V	1.04 ms/1.08 ms	[25]
BN film MSM	IBSD	212		204 > $10^3$	204/250 > $10^3$	$6.92 \times 10^9$		0.5 A/W @35 V		[27]
BN film MSM	IBSD	212		$5.3 \times 10^4$		$3.09 \times 10^{11}$		9.2 mA/W @20 V	<0.5 ms	[26]
BN film MSM	IBSD	212			212/284 $10^3$	$2.4 \times 10^8$		0.1 mA/W @20 V	0.32/0.63 s	[14]
BN film MSM	LPCVD	224	<10 pA @20 V	>312						[30]
BN film MSM	APCVD	220	$10^2$ fA		220/290 $10^4$	$3.9 \times 10^{10}$		3.4 mA/W @20 V	120 ms/160 ms	[32]
BN film MSM	APCVD	210	0.9 pA	45		$8.62 \times 10^9$		5.45 mA/W @5 V	376 ms/198 ms	[33]
BN film MSM	mechanically exfoliated	215				$3.68 \times 10^8$		53.76 $\mu\text{A/W}$ @20 V	0.38 s/0.77 s	[28]
BN film MSM	mechanically exfoliated	160			160/250 $10^4$		2133	2.75 A/W @20 V	0.3 ms/14 ms	[29]
BN film Schottky	solid-state reaction	210		$10^2$		$6.1 \times 10^{12}$	2945	5.022 A/W @5 V	0.2 s/-	[38]

### 3. DUV Photodetectors Based on Aluminum Nitride Material

The first synthesis of aluminum nitride (AlN) by reaction of nitrogen and molten aluminum can be traced back to 1862 [45], which did not receive much attention at that time. Since the 1960s, researchers have been committed to the growth of AlN single crystals [46,47]. As important III-V semiconductors, AlN exhibits high thermal conductivity ( $K \sim 3.19 \text{ W cm}^{-1} \text{ K}^{-1}$ ), high melting point ( $>2300 \text{ }^\circ\text{C}$ ), and large direct bandgap (6.28 eV) [48].

#### 3.1. AlN Nanostructures

Nanomaterials with a large surface-to-volume ratio and higher sensitivity have attracted attention in the photosensitive device application field. In recent years, UV photodetectors based on AlN nanostructures, especially nanowires, have been paid much attention, including photoconductors [49–51], MSM photodetectors [52,53], and Schottky photodiodes [54].

Liu et al. successfully prepared ultralong AlN nanowire (UAN) arrays using the CVD method [49]. Individual ultralong AlN nanowires showed significant photoconductive effects under different excited lights, which was attributed to the dominant molecular sensitization effects, as shown in Figure 6a. It was found that they had a much faster response speed of 1 ms, a higher photocurrent response of  $2.7 \times 10^6$ , and a more reproducible working performance in the air environment (Figure 6b,c). Teker fabricated a single-AlN nanowire DUV photodetector via high-quality AlN nanowires fabricated by the dielectrophoretic assembly method [51]. The DUV photodetector showed a high photocurrent response to the 254 nm UV light under a low operating voltage ( $\leq 3 \text{ V}$ ), with rise and decay time constants of 7.7 s and 11.5 s, respectively.

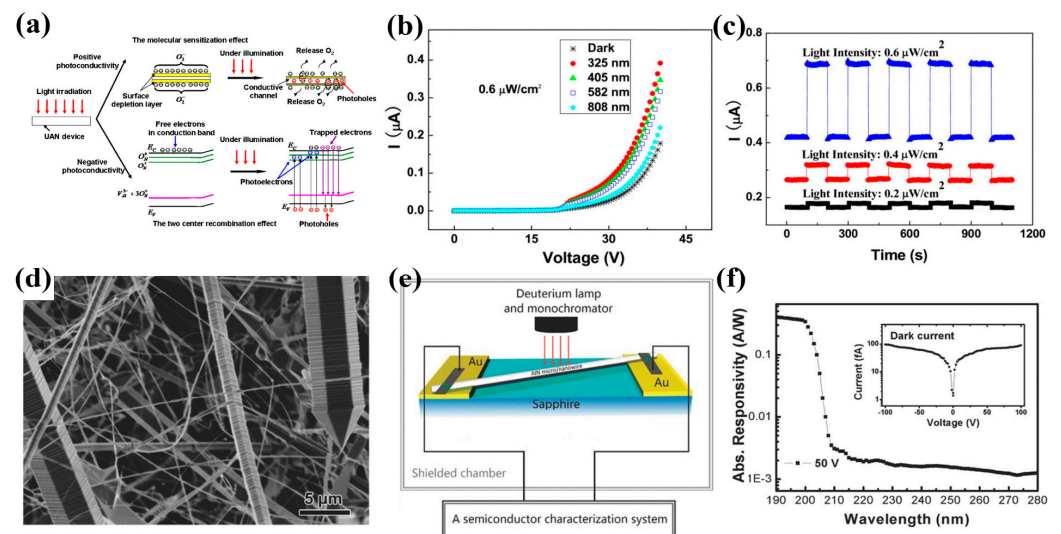


**Figure 6.** (a) Illustration of the photosensitive mechanisms of single UANs. (b) I–V curves of a single UAN at an irradiance of  $0.6 \mu\text{W}/\text{cm}^2$ . (c). Time response of a photocurrent at different light intensities under 325 nm light [49]. (d) SEM images of AlN micro/nanowires. (e) Schematic description of the photodetector. (f) Photoresponse spectrum under different wavelengths. Inset: dark current as function of voltage [52].

From the research results of Zheng et al., high-quality AlN micro/nanowires were grown by a two-step physical vapor transport method, the SEM images of which are shown in Figure 6d [52]. Figure 6e depicts the schematic diagram of a vacuum ultraviolet (VUV) detector fabricated by these micro/nanowires. From the response spectrum in Figure 6f, an ultrashort cutoff wavelength of 193 nm was found in this VUV photodetector. In addition, the fast photoresponse speed ( $<0.1 \text{ s}$ ) and recovery time ( $<0.2 \text{ s}$ ) were obtained. Ali et al. fabricated a flexible UV photodetector based on AlN nanowire networks via a low-cost non-lithographic fabrication scheme [53]. The detector exhibited a good photocurrent

response at 2 V bias, a very fast photoresponse rise time of 0.27 s, and a decay time of 0.41 s to UV light.

Yusuf et al. reported a highly responsive, flexible AlN single-nanowire ultraviolet photodetector [54]. Through a scalable and highly cost-efficient hot-contact method, detection arrays of very small-size devices capable of operating at 0 V and 30 V were achieved. The responsivity, excellent EQE, and detectivity of the detector were 1197.5 mA/W, 584%, and  $2.32 \times 10^{12}$  Jones under 254 nm UV light exposure at 30 V bias.

### 3.2. AlN Thin Films

With the development of semiconductor technology, many methods for growing AlN crystals have been developed, mainly including physical vapor transport (PVT) [55–57], chemical vapor deposition (CVD) [58–60], molecular beam epitaxy (MBE) [61], pulsed laser deposition (PLD) [62,63], and magnetron sputtering [64,65]. The common substrate materials used for epitaxial growth of AlN crystals mainly include Si, SiC [57], sapphire, etc.

At present, the research based on AlN film detectors is mainly focused on the MSM type [66–71]. For instance, Chen et al. deposited AlN thin films directly on c-plane sapphire substrates [66]. According to the evaluation of atomic force microscope, the films showed a smooth surface with a root mean square (RMS) roughness as small as 0.7 nm, and the spectral response of MSM photodetectors constructed with AlN/sapphire revealed peak responsivity at 200 nm and a UV/visible rejection ratio about  $10^2$ . Using the hydride vapor phase epitaxial (HVPE) technique, Murtaza et al. successfully deposited 200 nm thick AlN films onto an n-type silicon wafer [67]. Electrical and electro-optic characterization was conducted on different circuit configurations of AlN/silicon under various biases and temperatures, and it was found that reverse-biased silicon coupled with the interdigitated AlN scheme can provide the maximum response rate in photovoltaic and photoconductive modes.

Conventional MSM UV detectors have the shortcomings of a long carrier path, a finite electrical field, and difficult-to-adjust structural parameters. Li et al. demonstrated a 3D-MSM structural AlN-based DUV detector [70]. Compared with conventional MSM devices, 3D-MSM devices exhibited higher responsiveness and response speed. The enhanced performance was to be attributed to the intensified electrical field from the 3D metal electrode configuration and the inhibition of the carrier vertical transport, which unambiguously increased the carrier collection efficiency and migration speed. After that, the same group investigated the effect of asymmetric electrode materials (Figure 7a–c) on MSM device performance [69], and the Ni-Al device had better responsivity. Without applied voltage, a photoelectric response current increased from a dark current of 2.6 pA to 10 nA after UV illumination.

AlN was plagued with a large density of electronic surface states about  $10^{13}$  to  $10^{14}$  eV<sup>-1</sup> cm<sup>-2.5</sup>, which modified the current transport mechanisms and led to a large leakage current in the device [72]. Kaushik et al. used ZnTPP(OH) for passivation of the electronic surface states of AlN, forming a self-assembled monolayer, as shown in Figure 7d [71]. The surface modification of AlN effectively reduced the dark current of the photodetector without deteriorating the photocurrent. Based on the surface-modified AlN photodetector, the ratio of photocurrent to dark current was enhanced from 930 to 7835 at –2 V, and the responsivity doubled from 0.3 to 0.6 mA/W at 5 V (Figure 7e,f).

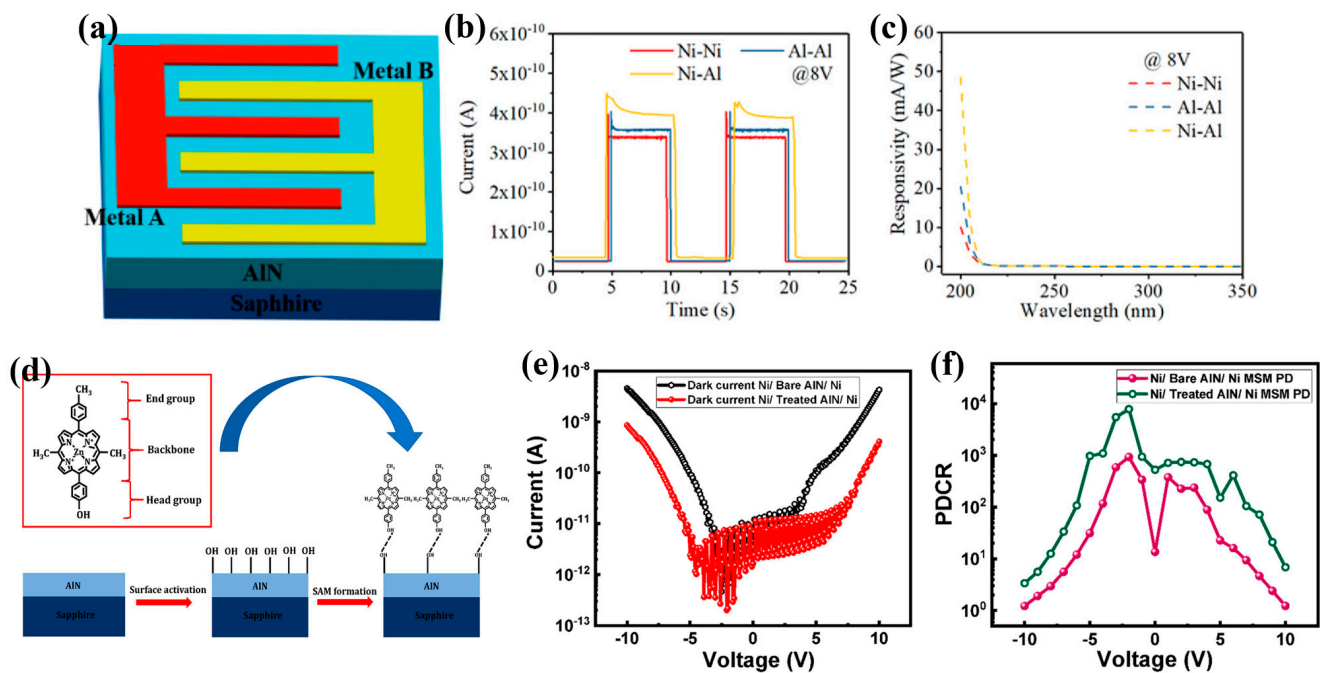


**Figure 7.** (a) Sketch of the asymmetric MSM device. Time-dependent photoresponse under 8 V bias for UV on and off (b), and responsivity (c) for different electrodes with Ni–Ni, Al–Al, and Ni–Al [69]. (d) Process of obtaining a self-assembled monolayer on an AlN epitaxial film. (e) Variation of dark current. (f) Photo-to-dark current ratio (PDCR) with voltage before and after surface modification [71].

### 3.3. AlN Heterostructures

AlN has been combined with a AlGaN film for DUV photodiode application [73]. DUV photodetectors based on AlN/AlGaN heterostructures grown on sapphire by MOCVD offered good performance at a wavelength of 240 nm. A simple-structure n-AlGaN/AlN phototransistor with a self-depleted full channel was reported, which was implemented by utilizing the strong polarization-induced electric field as a virtual photogate [74]. The complete depletion of the n-Al<sub>0.5</sub>Ga<sub>0.5</sub>N channel layer and the high optical gain of  $1.3 \times 10^5$  resulted in a very low dark current of 1.7 pA and a high photo-to-dark current ratio of  $10^8$  (Figure 8a,b). In addition, an ultrahigh responsivity of  $1.6 \times 10^5$  A/W and an ultrafast response speed of 537.5 ps were obtained (Figure 8c). AlN can combine with Ga<sub>2</sub>O<sub>3</sub> as a lateral heterojunction in order to perform solar-blind photodetection [75]. Under zero-bias conditions, the dark current, UV light switching ratio, linear dynamic region, photoresponsivity, specific detectivity, and rise and decay time were  $1.45 \times 10^{-13}$  A,  $2.14 \times 10^4$ , 86.74 dB,  $95.95 \mu\text{A W}^{-1}$ ,  $5.98 \times 10^{10}$  Jones, and 90/116 ms, respectively. The heterojunction with a staggered type-II band alignment was established successfully, which could be self-powered because of the built-in electric field formation. High-quality AlN films via the MOCVD technique were prepared by Li et al. [76], as shown in Figure 8d. A p-graphene/i-AlN/n-GaN photovoltaic far ultraviolet (FUV) detector was constructed, and Figure 8e shows the I-V characteristics of the device under 185 nm light and dark conditions, which indicates that there was an open-circuit voltage of ~1.15 V and an ultrahigh switching ratio at different voltages. The high responsivity of 25 mA/W and the sharp cutoff edge at 206 nm of the device are shown in Figure 8f.

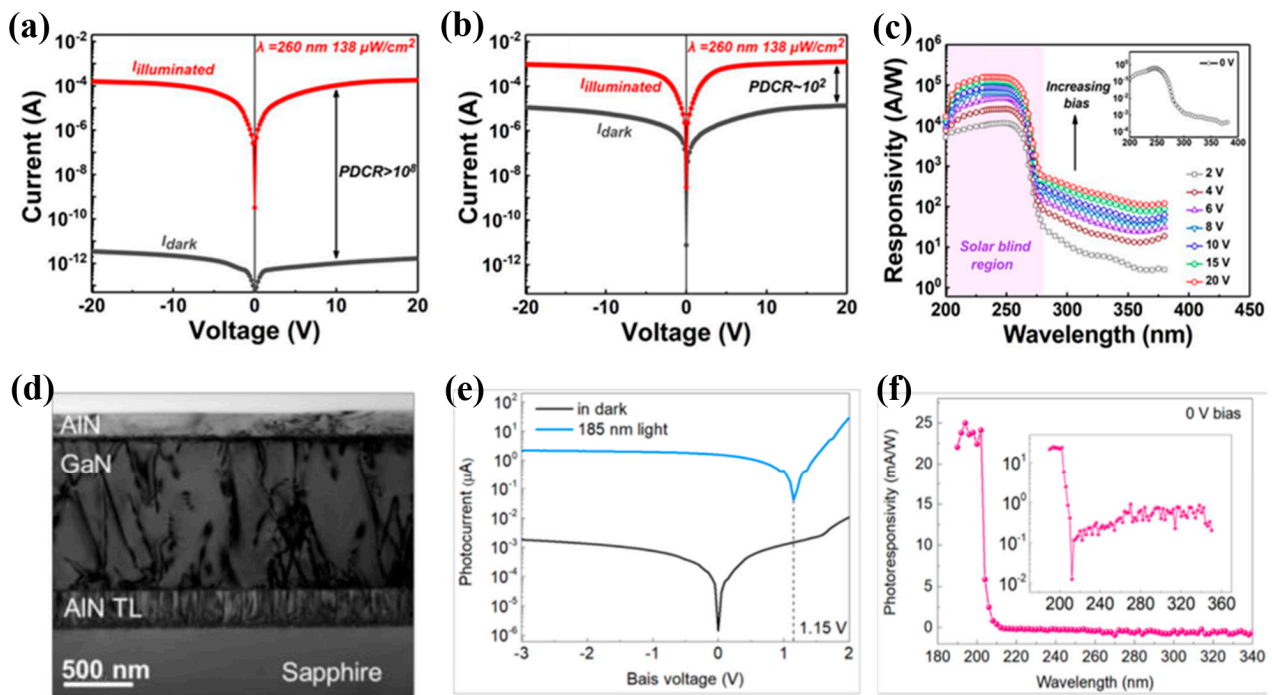


**Figure 8.** Dark and illuminated I–V curves of the n-Al<sub>0.5</sub>Ga<sub>0.5</sub>N/AlN photodetectors with different channel layer: (a) 70 nm and (b) 100 nm. (c) Spectral responses at different bias voltages of the FCSD phototransistor [74]. (d) Brightfield cross-sectional TEM images of AlN/GaN heterojunctions. (e) I–V characteristic of the devices under dark conditions and 185 nm light of 30.6 μW/cm<sup>2</sup>. (f) Spectral responsivity ( $R_\lambda$ ) curves of PDs illuminated by different-wavelength light. Inset:  $R_\lambda$ – $\lambda$  curve in logarithmic coordinates [76].

To conclude, AlN has obtained good response results in the DUV shortwave region due to the ultrawide bandgap. However, the responsivity of detectors based on AlN thin films is generally low, at the level of mA W<sup>−1</sup>. The responsivity of AlN micro/nanowires is higher than films due to their small body–surface ratio. AlN materials usually form heterojunction photodetectors with AlGa<sub>0.5</sub>N and GaN. These devices have excellent performance in dark current, on/off ratio, responsivity, and response speed, and have great development potential. Table 4 summarizes the performance parameters of AlN-based DUV photodetectors.

**Table 4.** Summary of performance parameters of DUV photodetectors based on AlN.

Device Structure	Fabrication Method	Light of Detection/nm	Dark Current	On/Off Ratio	Rejection Ratio	Specific Detectivity/Jones	EQE	Responsivity	Rise Time/Decay Time	Ref.
AlN nanowire photoconductor	CVD	325		20				$2.7 \times 10^6$ A/W @40 V	~1 ms	[49]
AlN nanowire photoconductor	LPCVD	254							7.7 s/ 11.5 s	[51]
AlN micro/nanowire MSM	PVT	190	<100 fA@20 V		VUV/UV-C ~10 <sup>4</sup>		254	0.39 A/W @50 V	<0.1 s/ <0.2 s	[52]
AlN nanowire MSM	LPCVD	254						2.43 mA/W @15 V	0.27 s/ 0.41 s	[53]
AlN nanowire Schottky	LPCVD	254				$2.32 \times 10^{12}$	584	1187.5 mA/W @30 V		[54]
AlN film 3D-MSM	MOCVD	200	2.6 pA					1.51 mA/W @0 V		[69]
AlN film 3D-MSM	MOCVD	200	4.2 pA@8 V					8 mA/W@2 V	2.61 ns/ 3 ns	[70]

Table 4. Cont.

Device Structure	Fabrication Method	Light of Detection/nm	Dark Current	On/Off Ratio	Rejection Ratio	Specific Detectivity/Jones	EQE	Responsivity	Rise Time/Decay Time	Ref.
AlN film FC-3DMSM	MOCVD	200	5.96 pA@8 V					9.6 mA/W @2 V	2.90 ns/ 2.92 ns	[70]
AlN film MSM	PVD	200	14.6 pA@5 V	7835@−2 V				0.6 mA/W @5 V	0.9 s/ 1.8 s	[71]
AlN/AlGaN Heterostructures MSM	MOCVD	240	10 pA@20 V							[73]
AlN/AlGaN Het- erostructuresTFT	LP- MOCVD	240	1.7 pA@20 V	>10 <sup>8</sup>	240/280 >10 <sup>2</sup>	1.5 × 10 <sup>18</sup> @20 V		1.6 × 10 <sup>5</sup> A/W @20 V	537.5 ps 3.1 us	[74]
Ga <sub>2</sub> O <sub>3</sub> /AlN heterojunction p-n	sputter	253	0.145 pA	2.14 × 10 <sup>4</sup>		5.98 × 10 <sup>10</sup>		95.95 μA/W @0 V	90 ms/ 116 ms	[75]
Gr/AlN/GaN Heterostructures p-i-n	MOCVD	194			194/212 >10 <sup>3</sup>		16	25 mA/W @0 V		[76]

#### 4. DUV PDs Based on Aluminum Gallium Nitride Material

The bandgap width of ternary alloy aluminum gallium nitride (AlGaN) material can continuously change from 3.4 eV of GaN to 6.2 eV of AlN due to the change in Al composition, and the corresponding cutoff wavelength is 365 nm to 200 nm. Because of its advantages of high breakdown field strength, high thermal conductivity, high-temperature resistance, and anti-illumination, the ultraviolet detector made of AlGaN material is particularly suitable for military, chemical, and other special environments [77,78]. Since the 1990s, people have successfully developed different types of lGaN-based UV detectors, which have been improved and innovated in device design, epitaxial growth, chip technology, and other aspects. As a result, the performance of AlGaN-based UV detectors has made great progress.

##### 4.1. AlGaN Nanostructures

As self-powered photodetectors, photoelectrochemical (PEC) PDs exhibit a series of advantages, including easy manufacturing process, low cost, excellent responsiveness, and fast photoresponse. Therefore, it has been widely studied to construct efficient self-powered PDs [79,80]. Wang et al. demonstrated a self-powered DUV photodetector in a PEC cell configuration, as schematically shown in Figure 9a, adopting n-type AlGaN nanowires (NWs) grown by the MBE technique as a photoelectrode [81]. Ru co-catalysts were used to modify the surface of NWs to ensure the excellent performance of the devices. The XPS analysis in Figure 9b unambiguously proved the strong interaction between Ru and AlGaN NWs. The self-powered DUV photodetector exhibited a large photocurrent density of 55 μA cm<sup>−2</sup>, excellent responsivity of 48.8 mA W<sup>−1</sup> at 254 nm illumination, and extraordinary fast response time of 83 ms (recover time was 19 ms) (Figure 9c). These results can be attributed to two sides. One is the highly uniform and defect-free n-type AlGaN nanowires. The other is the boosted carrier separation and collection efficiency through Ru modification.

Kang et al. demonstrated UV-C photodetectors based on Si-doped n-type Al<sub>0.45</sub>Ga<sub>0.55</sub>N nanorods via the MOCVD technique. Field-emission scanning electron microscopy (FE-SEM) showed that vertically arranged n-AlGaN nanorods were uniformly distributed on GaN seed crystals (Figure 9d). Compared with the corresponding dark current, the photocurrent (I<sub>p</sub>) of the manufactured photoconductive device is significantly higher in the UV-C region (Figure 9e). The optical responsiveness and sensitivity of the designed photodetectors are estimated to be ~115 mA/W and ~64%, respectively [82].

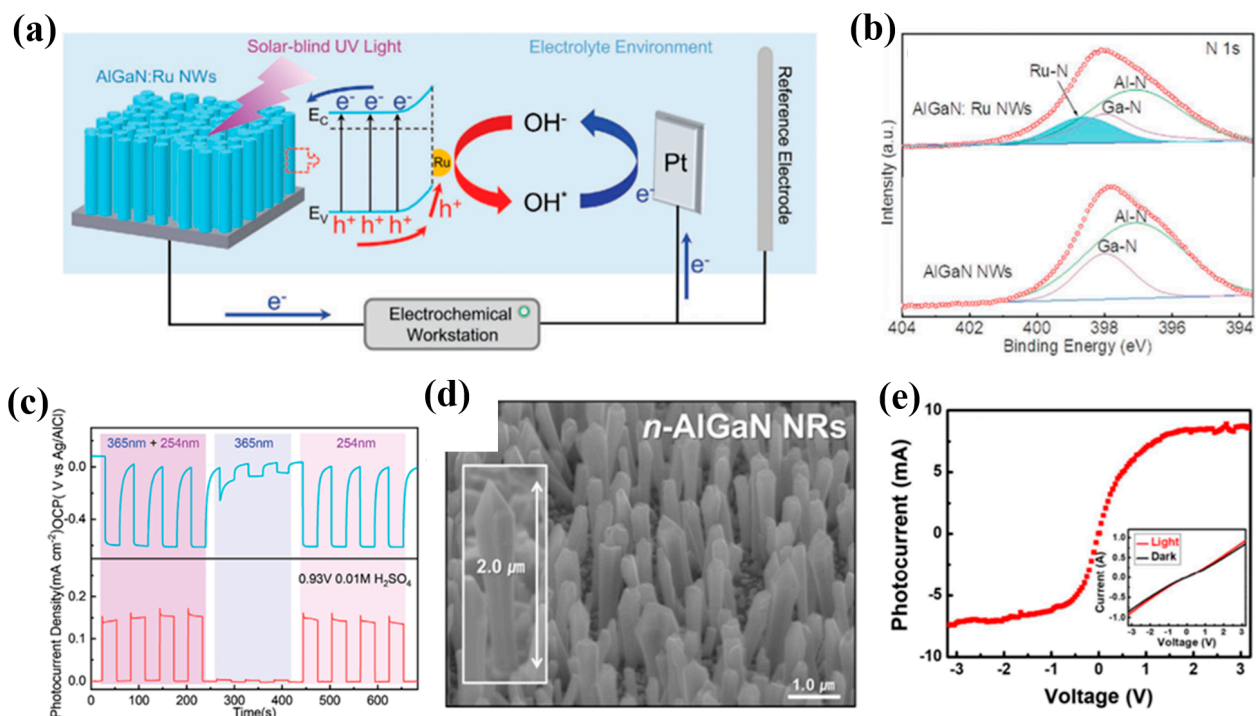


**Figure 9.** (a) Test system for the AlGaIn:Ru NW PEC PDs. (b) XPS spectra for N 1s of AlGaIn:Ru NWs and bare AlGaIn NWs. (c) Time-dependent (top) open-circuit potential and (bottom) photocurrent density under different irradiations [81]. (d) FE-SEM images of the n-AlGaIn nanorods. Insets: a single nanorod. (e) I–V characteristics of the photoconductive device measured in dark and under UV illumination [82].

#### 4.2. AlGaIn Thin Films

The localized surface plasmon resonance (LSPR) of metal nanoparticles (NPs) has attracted widespread attention due to its advantages of strong absorption, light efficiency, light trapping, and improved sensitivity. Moreover, due to the interaction between surface plasmon and light occurring at the interface between metal and dielectric, surface plasmon is also an effective method to improve the performance of photodetectors. Al NPs have been proven to be the efficient choice for plasmon-enhanced AlGaIn-based UV photodetectors [83–86]. For example, Lu et al. fabricated a Al<sub>0.4</sub>Ga<sub>0.6</sub>N MSM solar-blind ultraviolet photodetector with Al NPs, which exhibited high responsivity and low dark current [84]. Wu et al. realized AlGaIn-based PD with enhanced light response by in situ growth of Al NPs surface plasma [86]. The dark current and the spectral responsivity with different in situ Al NPs growth times at 10 V bias are shown in Figure 10a,b. All PDs with in situ grown Al NPs obtained a higher responsivity and enhanced peak responsivity.

Rathkanthiwar et al. demonstrated the enhancement effect of surface-terminated V-pits in tuning the dark current and spectral responsivity of Al<sub>0.25</sub>Ga<sub>0.75</sub>N-based photodetectors with MSM geometry on a Si (111) substrate [87] (Figure 10c). A sharp band edge at ~315 nm and responsivity of 2575 A/W at 20 V can be observed in Figure 10d. Temperature-dependent carrier transport analysis under dark and UV illumination revealed the observed large photocurrents came from the cumulative contributions of pit-induced thermionic field emission and hole-trapping-induced gain (Figure 10e,f). Ultrafast UV photodetectors based on AlGaIn were successfully developed with an MSM structure [88], the response time and low dark current of which were less than 25 ps and 20 pA, respectively. C-oriented AlGaIn grown on polycrystalline Mo substrate was also used as a DUV detector, the temperature effect of which could be decreased by 50% under high drive voltage [89].

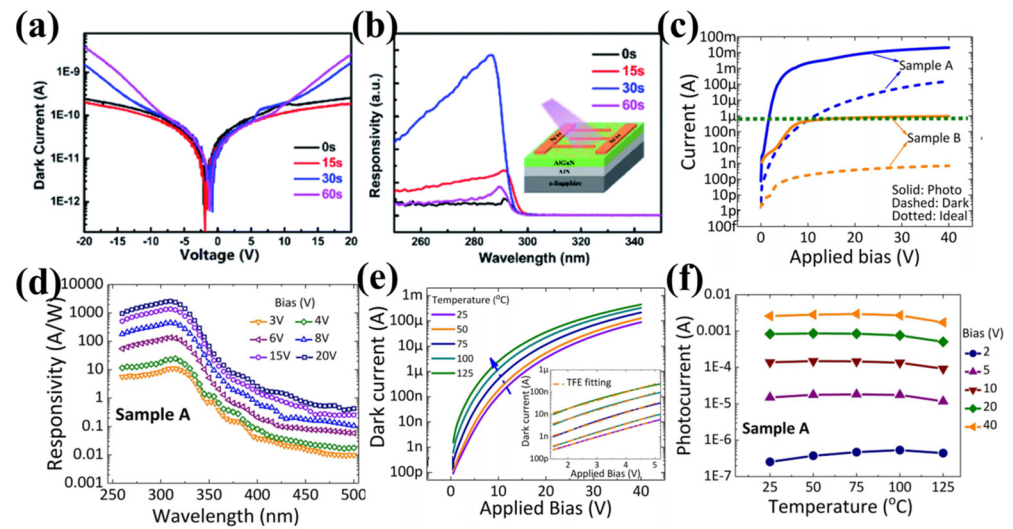


**Figure 10.** (a) Dark current–voltage curves. (b) Responsivity of AlGaN MSM detectors. Inset: structural schematic diagram of the device [86]. (c) Variation of dark and photocurrent with (sample A) and without (sample B) surface-terminated V-pits. (d) Variation of spectral responsivity with wavelength for Sample A of surface-terminated V-pits. (e) Temperature-dependent variation of dark current. Inset: TFE fitting of the dark current at different temperatures. (f) Variation of photocurrent with temperature at different applied biases for sample A under 280 nm light [87].

AlGaN p-i-n photodetectors composed of junctions with opposite doping types have been widely explored because it is feasible to optimize their quantum efficiency and response speed by tailoring their depletion layer thickness (the intrinsic layer). Back-illuminated  $\text{Al}_{0.40}\text{Ga}_{0.60}\text{N}$  p-i-n UV photodetectors with a high zero-bias EQE of 92% have been reported by Kalra et al. [90], which demonstrated a 10 orders of magnitude rectification, a low reverse leakage current density of  $1 \text{ nA/cm}^2$  at 10 V, a high  $R_0A$  product of  $1.3 \times 10^{11} \Omega \cdot \text{cm}^2$ , and supported fields exceeding  $5 \text{ MV/cm}$  (Figure 11a). The light-to-dark current ratio and the UV-to-visible rejection ratio for the detectors exceeded  $10^6$ , with a responsivity of  $211 \text{ mA/W}$  (0 V at 289 nm) and a thermal noise limited detectivity ( $D^*$ ) of  $6.1 \times 10^{14} \text{ cmHz}^{1/2}\text{W}^{-1}$  (Figure 11b). A p-i-n photodetector based on AlGaN epi-layers grown by low-pressure MOCVD on c-plane sapphire substrates was achieved by the same group [91], which exhibited a dark current density of  $4 \text{ nA cm}^{-2}$ , a zero-bias EQE of 74.7%, a UV-to-visible rejection ratio exceeding  $10^7$ , and a thermal noise detectivity measuring  $4.2 \times 10^{14} \text{ cm Hz}^{1/2} \text{ W}^{-1}$ . In addition, through a reduction in the screw dislocation density, the dark current was reduced by 2 orders of magnitude, and the EQE was also significantly increased.

AlN epitaxial layer containing conductive spontaneous via holes (v-AlN) could be prepared on n+-Si substrates using MOCVD in a process that turns the insulating AlN epitaxial layer into a conductive AlN layer. The size and density of the via holes were controlled by the crystal growth conditions used for the layer, and this enabled the control of the conductivity of the layer [92]. A vertical UV solar-blind photodetector was fabricated by growing an i-AlGaN layer and a p-GaN layer on v-AlN, as shown in Figure 11c. Gautam and collaborators compared and analyzed the performance differences between AlGaN-based detectors grown on AlN and sapphire substrates [93]. The low defect density at the AlN substrate/AlN buffer ( $\sim 10^4 \text{ cm}^{-2}$ ) interface led to the DUV photodetectors on AlN substrates achieving a 4 orders of magnitude lower dark current. Figure 10d–f shows the device structure and results.

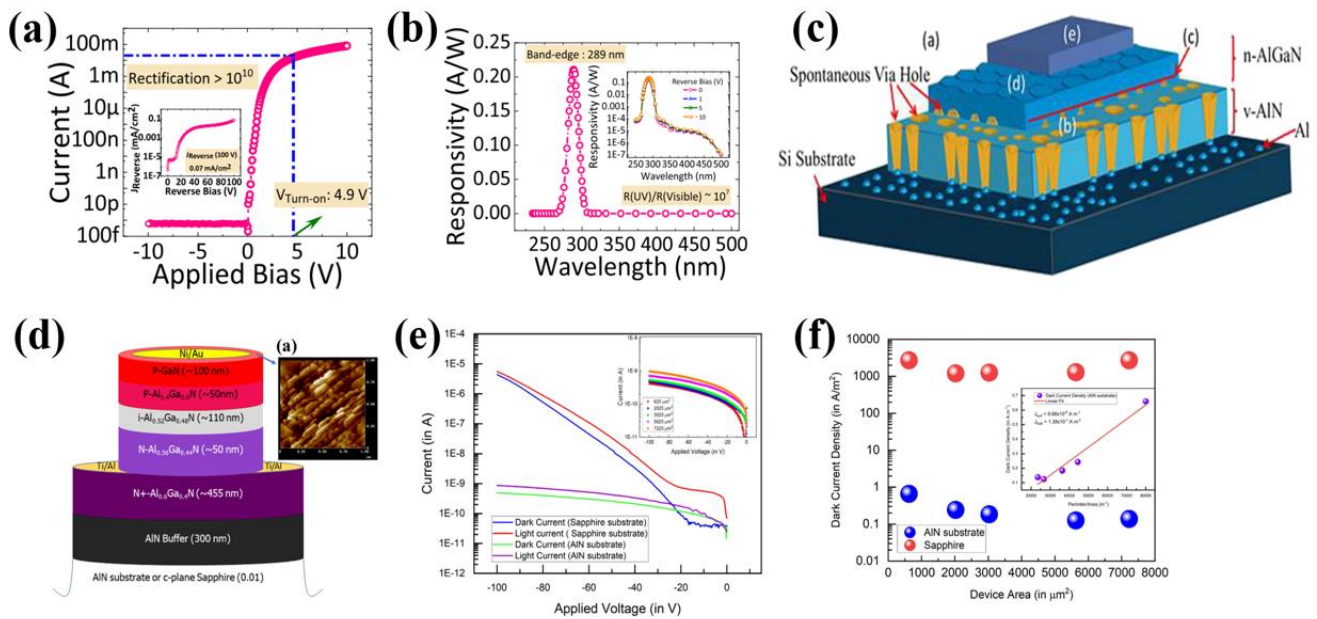


**Figure 11.** (a) I–V characteristics of the detectors. Inset:  $J_{\text{Reverse}}$  variation with bias, until 100 V. (b) Responsivity variation for the p–i–n detectors. Inset: Responsivity plot in the semi–log scale for 0 to 10 V reverse bias [90]. (c) Schematic diagram of epitaxial layers [92]. (d) Structure of UV detector. Inset: showing AFM image of the p–GaIn capping layer. (e) I–V curves under broadband UV light illumination and dark conditions. Inset: dark current scaling for different diode areas. (f) Dark current density under 100 V reverse bias with different device areas. Inset: dark current density as function of perimeter/area [93].

#### 4.3. AlGaIn Heterostructures

A novel UV photodetector structure based on graphene electrodes and silicon substrates with vertical AlGaIn nanowires was demonstrated [94]. The rectification characteristics of the I–V curve were formed through a graphene/vertical AlGaIn nanowire array heterojunction, at a dark current of 54 nA (@–2 V), as shown in Figure 12a. The manufactured device exhibits a response of 0.176 mA W<sup>–1</sup> with a bias voltage of –2 V and stable switching characteristics (Figure 12b). It has been proposed that photogenerated electrons and holes can reach the positive and negative electrodes through diffusion or tunneling effects, even in the thick AlN region.

Avalanche photodiodes (APDs) based on AlGaIn heterojunctions have shown superphotoresponse properties. However, the large polarization-induced charge formed at the hetero interface is detrimental to device operation in that it confines the electric field to the SiC multiplication region and results in poor carrier collection from the SiC multiplication region and the AlGaIn absorption layer. Rodak et al. used thin AlN layers inserted at the AlGaIn/SiC hetero interface as nitride interface charge control layers (NICCLs), as shown in Figure 12c. This was an effective method to reduce the total positive charge at the interface and increase the field in the AlGaIn absorption region [95]. AlGaIn/SiC separate absorption and multiplication avalanche photodiodes (SAM-APDs) were proven to have high-gain photodetectors with tunable absorption in the DUV regime (Figure 12d). Sood et al. developed GaN/AlGaIn UV-APDs with large pixel sizes [96]. Figure 12e depicts the schematic diagram of p–i–p–i–n APDs, which were fabricated through the MOCVD method on GaN substrates with optimized material growth and doping parameters. In the spectral range of 320–400 nm, through a strong avalanche multiplication process, a high optical gain of  $5 \times 10^6$  and enhanced quantum efficiency were demonstrated (Figure 12f).

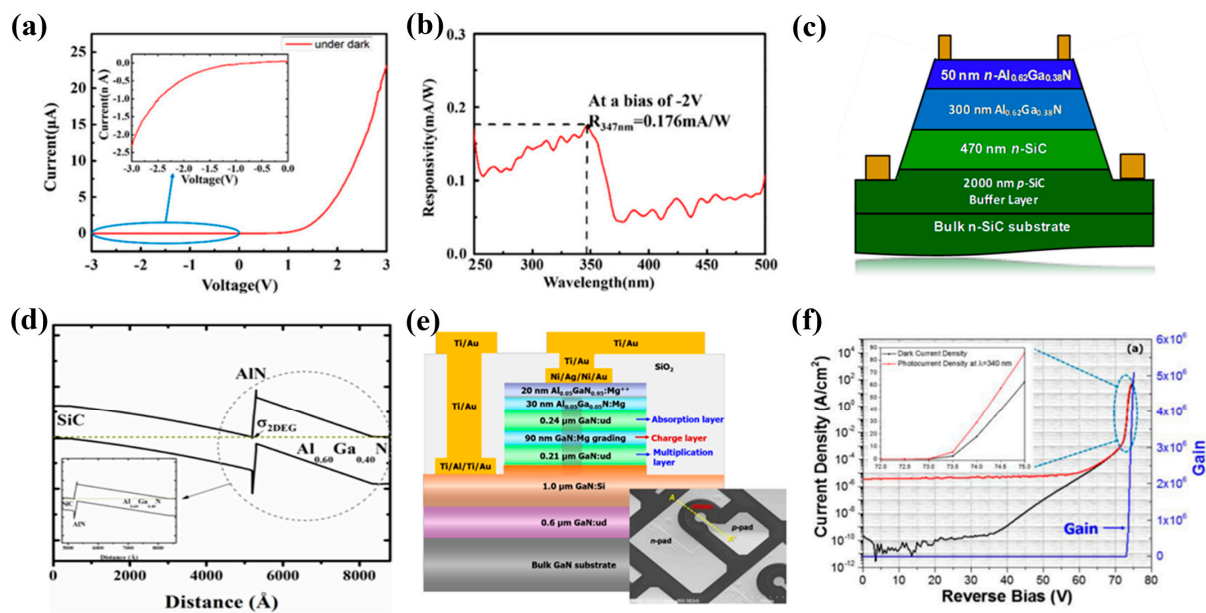


**Figure 12.** (a) Current–voltage characteristics, (b) Spectral response of device [94]. (c) Schematic of AlGaN/SiC SAM APD device. (d) Band diagram of the NICCL APD [95]. (e) Schematic cross-sectional structure of the device. Inset: SEM image of APD physical layout. (f) Reverse-bias J–V characteristics under dark conditions and 340 nm UV illumination [96].

Nguyen et al. reported AlGaN/GaN two-dimensional electron gas (2DEG)-based photodetectors employing a simple one-mask fabrication technique [97]. The I–V characteristics of the photodetector are shown in Figure 13a, which illustrates the perfect Ohmic contacts between the metal and AlGaN surface. Figure 13b shows the response current of the photodetector under different light power densities. Research on phototransistors based on AlGaN/GaN heterojunction has also made good progress [98–100]. For instance, Gao et al. prepared a graphene/AlGaN/GaN DUV photodetector with an ultrahigh responsivity of  $3.4 \times 10^5$  A/W at 261 nm light [98]. To optimize the trade-off between responsivity and response speed, a back-gate electrode was designed in the AlGaN/GaN 2DEG region, which eliminated the persistent photocurrent effect and shortened the recovery time from several hours to several milliseconds. Sun et al. micro-fabricated a suspended  $\text{WO}_3$ -gate AlGaN/GaN heterostructure photodetector integrated with a micro-heater for ultraviolet photodetection (Figure 13c) [100]. The device exhibited a high responsivity of  $1.67 \times 10^4$  A  $\text{W}^{-1}$  at 240 nm and a sharp cutoff wavelength of 275 nm (Figure 13d). More importantly, the persistent photoconductivity (PPC) effect can be eliminated through a mono-pulse heating reset (MHR), which involves applying an appropriate pulse voltage to the micro-heater right after the removal of the UV illumination. The recovery time was reduced from hours to just seconds without reducing the high responsivity and stability of the photodetector (Figure 13e,f).

In summary, high-quality AlGaN is mostly prepared by the MOCVD method, and various material morphologies have been studied with great responsivity and response speed. Table 5 summarizes the performance parameters of AlGaN-based DUV photodetectors. The research on p–i–n-type structures is the most extensive, and the related preparation techniques are the most mature. The research on AlGaN APD is also very early, with avalanche multiplication gain reaching the fourth order of ten. Recently, AlGaN photodetectors with a three-terminal TFT structure have attracted the attention of researchers, which exhibited excellent responsivity ranging from  $10^3$  to  $10^5$  A  $\text{W}^{-1}$ .

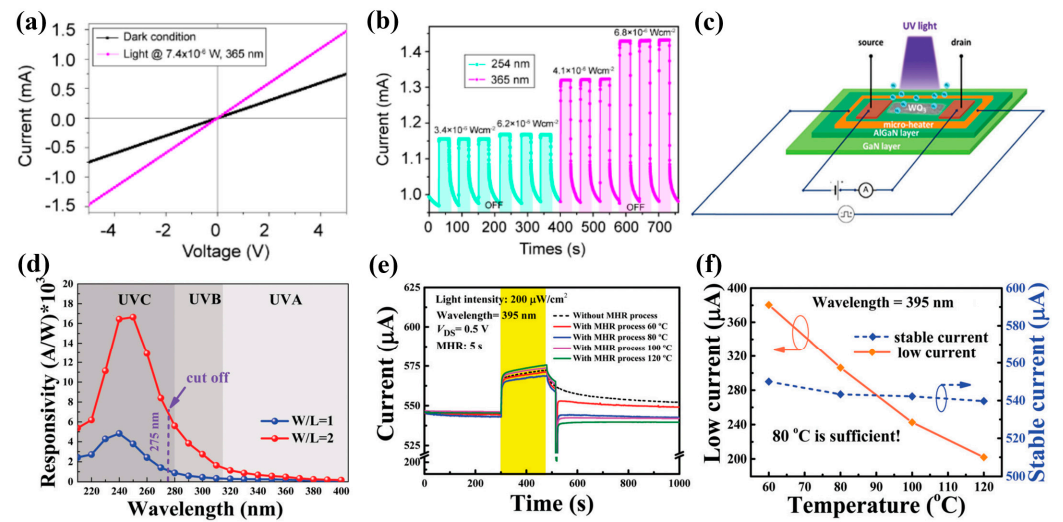


**Figure 13.** (a) I-V characteristics of the detector in dark conditions and under UV illumination. (b) Current response at different illumination conditions [97]. (c) Schematic illustration of the WO<sub>3</sub>/AlGaIn/GaN heterostructure photodetector. (d) Spectral response. (e) Transient photocurrent response. (f) Low drain current and stable current of the heterostructure detector [100].

**Table 5.** Summary of performance parameters of DUV photodetectors based on AlGaIn.

Device Structure	Fabrication Method	Light of Detection/nm	Dark Current	On/Off Ratio	Rejection Ratio	Specific Detectivity/Jones	EQE	Responsivity	Rise Time/Decay Time	Ref.
AlGaIn nanowires	MBE	254						48.8 mA/W @0 V	83/19 ms	[81]
PEC AlGaIn Nanorods	MOCVD	250–276						115 mA/W @3 V		[82]
AlGaIn Film MSM	MOCVD	275	$J < 2 \times 10^{-9}$ A/cm <sup>2</sup> @−10 V		UV/vis >10 <sup>6</sup>		80	176 mA/W @0 V		[101]
AlGaIn Film MSM	MOCVD			$1.2 \times 10^4$	UV/vis $2 \times 10^3$		$5 \times 10^4$	2575 A/W @20 V		[87]
AlGaIn Film MSM	MOCVD	266						$1.7 \times 10$ mA/W @−1 V	1.37 s/1.87 s	[89]
AlGaIn Film p-i-n	MOCVD	289	$J = 1 \times 10^{-9}$ A/cm <sup>2</sup> @10 V	>10 <sup>6</sup>	DUV/vis >10 <sup>6</sup>	$6.1 \times 10^{14}$	92	211 mA/W @0 V	<13 ms/ <13 ms	[90]
AlGaIn Film p-i-n	MOCVD	289	4.2 pA		DUV/vis >10 <sup>6</sup>	$4 \times 10^{14}$	74.7 @0 V		<13 ms/ <13 ms	[91]
AlGaIn Film p-i-n	MOCVD			$1.2 \times 10^4$	$2.3 \times 10^3$		$5 \times 10^4$	2575 A/W @20 V		[92]
AlGaIn/GaN heterostructure APD	MOCVD	240						$1.67 \times 10^4$ A/W @0.5 V	- /7 s	[96]
AlGaIn/GaN heterostructure photoconductive	MOCVD	254						$1.5 \times 10^4$ A/W@10 V		[97]
AlGaIn/GaN Heterostructure TFT	MOCVD	261						$3.4 \times 10^5$ A/W @1 V	100 ms	[98]
AlGaIn/GaN heterostructure TFT	MOCVD	240						$4.6 \times 10^3$ A/W @0.5 V	8.4 s/170 s	[99]
AlGaIn/GaN heterostructure TFT	MOCVD	240	55.4 nA					$1.67 \times 10^4$ A/W @0.5 V	- /7 s	[100]

### 5. DUV PDs Based on Gallium Oxide Material

Gallium oxide (Ga<sub>2</sub>O<sub>3</sub>) is a direct wide-bandgap (4.8–5.2 eV) semiconductor material that has high dielectric constant, thermal stability, and chemical stability, making it a great application prospect in solar-blind UV, gas sensors, solar cells, catalysis, and other fields [102]. Ga<sub>2</sub>O<sub>3</sub> has seven corundum (α-), monoclinic (β-), defective spinel (γ-),

orthorhombic ( $\delta$ -), orthorhombic ( $\epsilon$ -), polycrystalline, and amorphous phases. In these different structures, the  $\beta$ - phase is the most stable, and other phases will change into  $\beta$ - mutually [103,104]. At present,  $\text{Ga}_2\text{O}_3$  materials used to prepare solar-blind detectors mainly include  $\beta$ - $\text{Ga}_2\text{O}_3$  crystals, crystal epitaxial films, and nanostructures, among which thin-film devices are widely used because of their convenient preparation [105]. However, the  $\text{Ga}_2\text{O}_3$  thin films usually prepared are amorphous, and post-annealing treatment is required to achieve crystals.

### 5.1. $\text{Ga}_2\text{O}_3$ Nanostructures

As an ideal building block for solar-blind DUV photodetectors, low-dimensional  $\text{Ga}_2\text{O}_3$  nanostructures, including nanowires (NWs) [106–109], nanobelts (NBs) [110,111], nanoflowers (NFs) [112], and nanosheets/nanoflakes [113–116], have been explored by many groups. For example, Weng et al. reported a solar-blind  $\beta$ - $\text{Ga}_2\text{O}_3$  nanowire photodetector [106], which was solar blind with a sharp cutoff at 255 nm and a high responsivity of  $8 \times 10^{-4}$  A/W (255 nm at 10 V). Chen et al. used metal Ga as a raw material to grow a  $\text{Ga}_2\text{O}_3$  nanowire array by the simple thermal oxidation method and prepared a photodetector with a Schottky-type vertical structure of Au/ $\text{Ga}_2\text{O}_3$  nanowires, as shown in Figure 14a [108]. The maximum optical response value was obtained at about 258 nm, and the corresponding responsivity was 0.6 mA/W at the bias voltage of  $-10$  V (Figure 14b). Additionally, the device exhibited a low dark current of 10 pA at  $-30$  V (Figure 14c), a fast response time of about 64  $\mu$ s, and the characteristic of self-power supply.

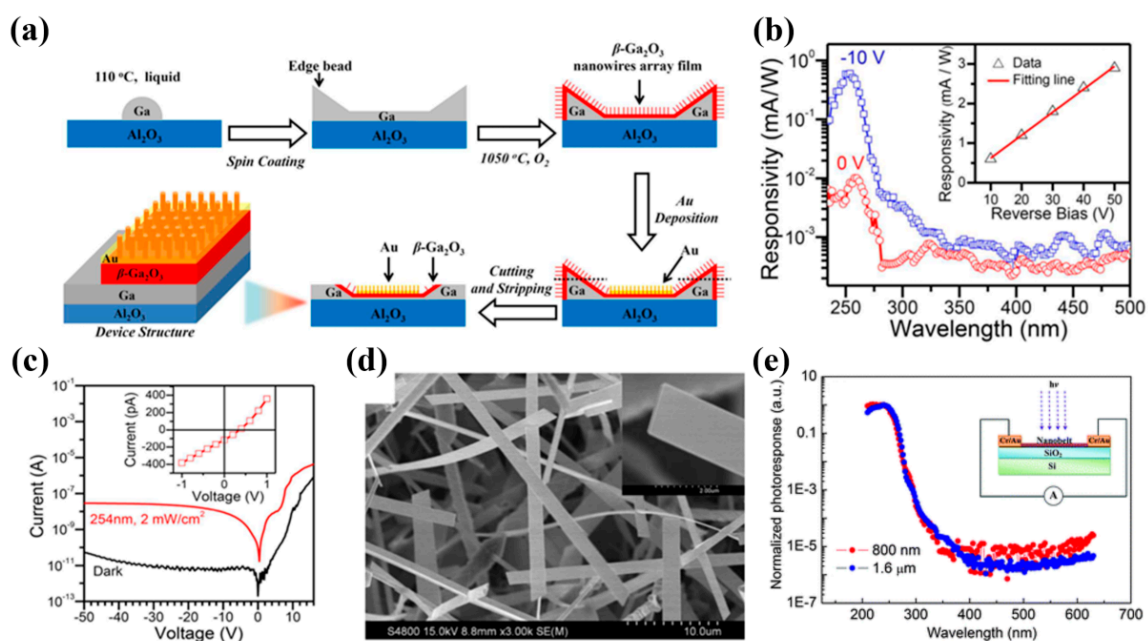


**Figure 14.** (a) Schematic illustration of the fabrication of  $\beta$ - $\text{Ga}_2\text{O}_3$  nanowires array film and its vertical Schottky photodiode. (b) Spectral responses of the device at 0 V and  $-10$  V. Inset: responsivity at 254 nm illumination. (c) I–V characteristics of device in dark and under 254 nm light. Inset: photovoltaic characteristic [108]. (d) SEM image of  $\text{Ga}_2\text{O}_3$  nanobelt. (e) Spectral response of the devices. Inset: schematic configuration of a photoconductive measurement [110].

Using individual  $\text{Ga}_2\text{O}_3$  nanobelts, Li et al. designed solar-blind semiconductor photodetectors [110]. The high-magnification SEM image in Figure 14d shows the smooth surface and uniform thickness of each nanobelt. The photodetector exhibited high selectivity towards 250 nm light, with a response time of less than 0.3 s and a ratio of photocurrent to dark current of up to 4 orders of magnitude (Figure 14e). Zhong et al. prepared single-crystal  $\beta$ - $\text{Ga}_2\text{O}_3$  nanobelts by the CVD method [111]. The response speed of the detector based on nanoribbons to 254 nm light was less than 20 ms, the response was 19.31 A/W,

and the EQE was 9427%. Teng et al. prepared the metastable phase of  $\gamma$ -Ga<sub>2</sub>O<sub>3</sub> nanoflower by the hydrothermal method [112]. The acquisition of the metastable phase of  $\gamma$  was closely related to the PH value in the solution. The detector made of  $\gamma$ -Ga<sub>2</sub>O<sub>3</sub> nanoflower exhibited excellent solar-blind photoelectric performance.

Recently, 2D or quasi-2D  $\beta$ -Ga<sub>2</sub>O<sub>3</sub> nanosheets/nanoflakes have been successfully prepared by oxidizing 2D GaSe or directly peeling from  $\beta$ -Ga<sub>2</sub>O<sub>3</sub> bulk crystals. Feng et al. prepared 2D Ga<sub>2</sub>O<sub>3</sub> nano-sheets by thermal oxidation of GaSe nanosheets [113]. The nanosheets were polycrystalline and less than 10 nm thick. The photodetector based on Ga<sub>2</sub>O<sub>3</sub> nano-panel had a fast response to 254 nm light, with a response of 3.3 A/W and an EQE of 1600%. Sooyeoun et al. fabricated solar-blind photodetectors based on exfoliated quasi-2D  $\beta$ -Ga<sub>2</sub>O<sub>3</sub> flakes, and then the photoresponsive properties were characterized systematically. The device structure manufactured was based on a back-gate field-effect transistor, which exhibited extraordinary photoresponsive properties, including the highest responsivity ( $1.8 \times 10^5$  A W<sup>-1</sup>) among reported semiconductor thin-film solar-blind photodetectors [114]. Considering that the thickness of the mechanically peeled  $\beta$ -Ga<sub>2</sub>O<sub>3</sub> sheet was relatively thick and uncontrollable, Kwon et al. used the reactive ion-etching technique to thin it [116]. By plasma etching with SF<sub>6</sub>,  $\beta$ -Ga<sub>2</sub>O<sub>3</sub> flakes with a thickness of 60 nm were achieved.

### 5.2. Ga<sub>2</sub>O<sub>3</sub> Thin Films

The fundamental correlation between gain mechanisms and leakage carrier transport in MSM Ga<sub>2</sub>O<sub>3</sub> photodetectors was not clear in the early days. To understand the carrier transport and gain mechanisms, Xu et al. investigated the reverse leakage and photocurrent behaviors based on Ga<sub>2</sub>O<sub>3</sub>-based MSM PDs at different biases and operation temperatures in detail [117]. The carrier transport mechanisms were ascribed to different tunneling processes, including thermionic field emissions and Poole–Frenkel emissions at low and high fields, respectively [118]. Under 255 nm illumination, MSM photodetectors fabricated on PLD  $\beta$ -Ga<sub>2</sub>O<sub>3</sub> thin films were operated up to 250 °C temperature. The obtained activation energies from the Arrhenius plot of the rise and decay times corresponded to the energy of electron–phonon interaction and the transition of self-trapped holes (STHs) to mobile holes in  $\beta$ -Ga<sub>2</sub>O<sub>3</sub>. Therefore, it was found that the generation and recombination mechanisms of charge carriers occur through electron–phonon interaction and STH.

Deep-level defects were also investigated in  $\beta$ -Ga<sub>2</sub>O<sub>3</sub> films [119,120]. Using the fractional emptying thermally stimulated current (TSC) method, several deep-level traps having activation energies were identified. The most dominant trap level with activation energy of 1.03 eV was found, potentially because of the persistent photocurrent in PLD-grown  $\beta$ -Ga<sub>2</sub>O<sub>3</sub> thin films.

To further improve the performances of the Ga<sub>2</sub>O<sub>3</sub> films, the post-thermal treatment was used [121–124]. Using a plasma-enhanced atomic layer deposition system, Ga<sub>2</sub>O<sub>3</sub> films were deposited on sapphire substrates and annealed in an O<sub>2</sub> ambient furnace system for 15 min at different temperatures [121]. Figure 15a,b shows the XRD spectra and photoluminescence (PL) spectra of Ga<sub>2</sub>O<sub>3</sub> films annealed at various temperatures. MSM UVC PDs with various Ga<sub>2</sub>O<sub>3</sub> active layers were fabricated and studied, and the PDs with the 800 °C-annealed layers exhibited better performances, with high photoresponsivity of 22.19 A/W (@5 V) and excellent UV/visible rejection ratio of  $5.98 \times 10^4$  (Figure 15c). Li et al. investigated the effects of thermal treatments, including furnace annealing and rapid thermal annealing (RTA) on Ga<sub>2</sub>O<sub>3</sub> films [122]. With the increase in treatment temperature, a quasi-single-crystalline structure of the Ga<sub>2</sub>O<sub>3</sub> film could be achieved PDs based on this Ga<sub>2</sub>O<sub>3</sub> film have a photo/dark current ratio of  $1.78 \times 10^5$  at 5 V under 230 nm light and a responsivity of 0.55 A/W (Figure 15d,e). Zhou et al. demonstrated MSM photoconductors with high responsivity and gain over a wide spectral range of DUV to NIR based on  $\alpha$ -Ga<sub>2</sub>O<sub>3</sub> thin films grown by the laser MBE technique [123]. It was found that a “thermal relaxation” (TR) process (short-time heating) could reduce the dark current

and improve the response recovery time without reducing the gain of the  $\alpha$ -Ga<sub>2</sub>O<sub>3</sub> detector (Figure 15f).

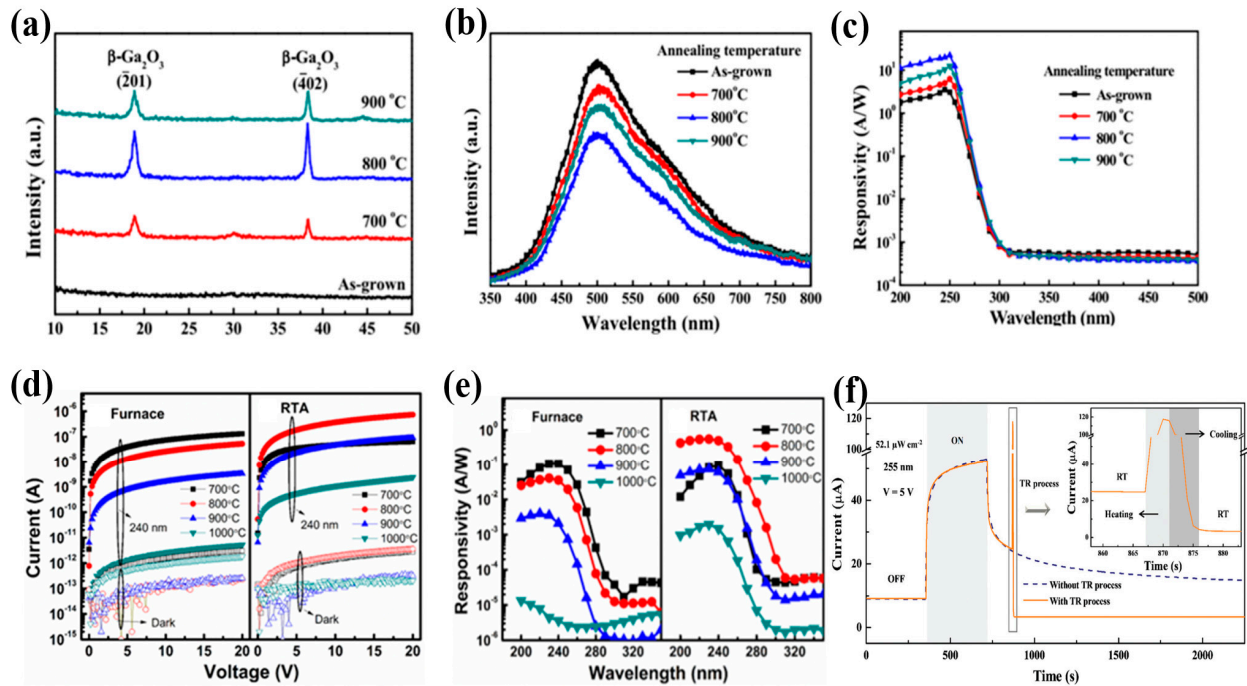


**Figure 15.** (a) XRD spectra and (b) room-temperature PL spectra of Ga<sub>2</sub>O<sub>3</sub> films annealed at different temperatures. (c) Photoresponsivity spectra of various Ga<sub>2</sub>O<sub>3</sub>-based MSM UVC PDs [121]. (d) I–V characteristics. (e) Spectral response of the Ga<sub>2</sub>O<sub>3</sub> MSM photodetectors with various thermal treatments (240 nm @5 V) [122]. (f) Time-dependent photoresponse of the  $\alpha$ -Ga<sub>2</sub>O<sub>3</sub> photodetector, Inset: short-time heating application process [123].

Most  $\beta$ -Ga<sub>2</sub>O<sub>3</sub> PDs have difficulties in acquiring both a peak response at wavelengths shorter than 254 nm and a slow responsivity drop from 250 to 200 nm [125]. By doping Al [125–127], Zr [128], Sn [129,130], Cd [131], and other elements in Ga<sub>2</sub>O<sub>3</sub> thin films, the intrinsic bandwidth can be adjusted to modulate the cutoff wavelength of MSM DUV photodetectors. For instance, Yuan et al. discussed the effects of the trace Al on the performance of PDs based on cosputtered aluminum gallium oxide (AGO) material after thermal annealing at 900 °C [125]. The AGO PD with the Al/(Al + Ga) ratio of 1.8% showed excellent performance, the peak responsivity, photocurrent, dark current, and detectivity of which were improved 53.61, 46.4, 0.83, and 96.5 times, respectively, at 230 nm under 5 V than that of the Ga<sub>2</sub>O<sub>3</sub> PDs. (Figure 16a–c). Guo et al. prepared tunable bandgap ZrGaO films on n-GaN substrates via RF magnetron sputtering [128]. The bandgap of ZrGaO film deposited was broadened to 5.4 eV with a Zr target sputtering power of 70 W (Figure 16d). Then, a p–i–n photodetector was fabricated based on the ZrGaO film, which had typical I–V characteristics, as shown in Figure 16e. Responsivity of the device at different wavelengths under 0 V bias is measured in Figure 16f, with a high responsivity of 0.035 A/W under 185 nm light. Li et al. investigated the preparation of Sn-doped  $\beta$ -Ga<sub>2</sub>O<sub>3</sub> films using sol–gel method under ambient condition [129]. Compared with the undoped films, MSM detectors based on Sn-doped films with needle-like grains obtained a low dark current of 0.76 nA, a responsivity of 164 mA/W, and a detectivity of  $3.21 \times 10^{12}$  Jones at 30 V.

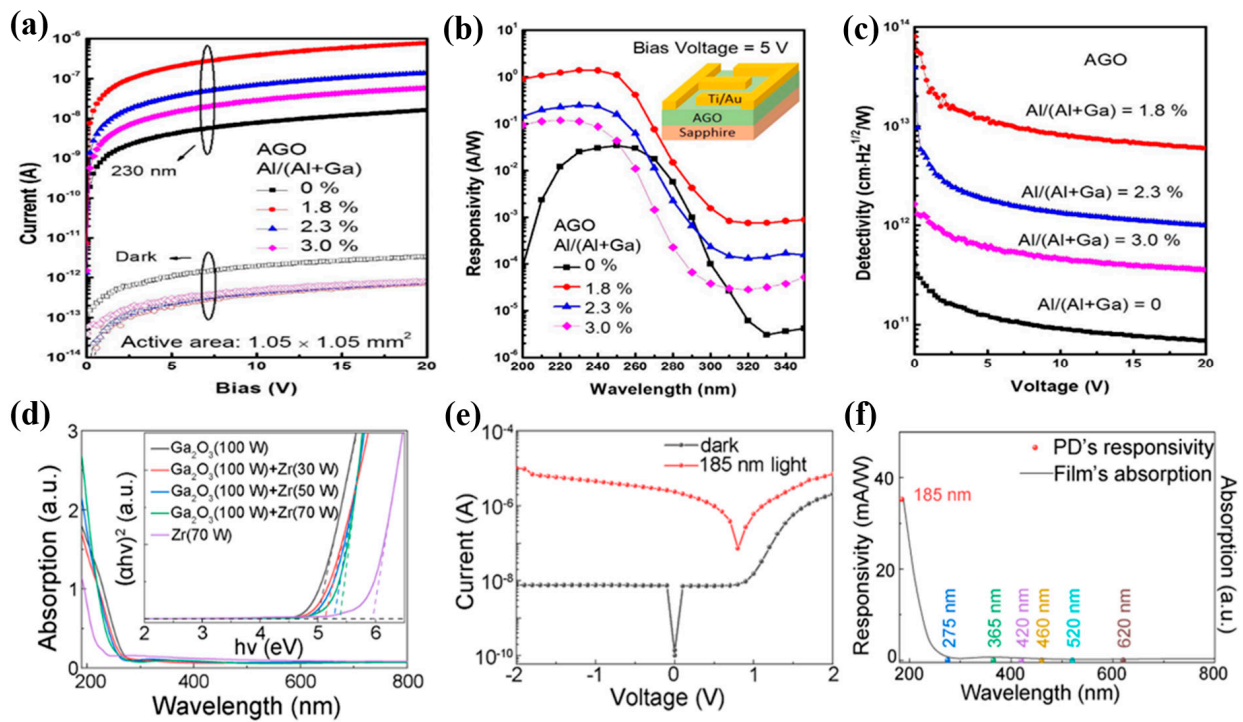


**Figure 16.** (a) I–V characteristics and (b) spectral response of the AGO PDs. Inset: device configuration of the MSM PD. (c) Relationship between detectivities and voltage of the AGO PDs under 230 nm light [125]. (d) Absorption spectra of ZrGaO films with different Zr doping contents. Inset: relationship between  $(\alpha hv)^2$  and photon energy ( $hv$ ). (e) I–V characteristics of PD in dark state and under 185 nm illumination. (f) Responsivity of the ZrGaO-film-based DUV PD at different wavelengths under 0 V bias [128].

Recently, thin-film transistor (TFT) photodetectors have received more attention because of their self-amplification of photocurrent through gate control function and easier integration with other devices in the circuit [131–135]. For instance,  $\alpha$ - $\text{Ga}_2\text{O}_3$ : CdO thin films and their TFT photodetectors were fabricated by the spin-coating method [131]. The optical bandgap of the film could be regulated by the Cd content ( $C_{\text{Cd}}$ ). The corresponding TFT devices demonstrated a large negative shift in turn-on voltage due to the increase in the electron concentration (Figure 17a,b). The optimized device at 15%  $C_{\text{Cd}}$  exhibited a responsivity of 2.17 A/W, a high UV/vis. rejection of  $1.88 \times 10^4$ , and an EQE of 1036% under 260 nm at  $V_{\text{GS}} = 0.2$  V and  $V_{\text{DS}} = 1$  V (Figure 17c). Li et al. demonstrated high-performance  $\beta$ - $\text{Ga}_2\text{O}_3$  phototransistors with a local back-gate structure [134]. The phototransistors had a high responsivity of  $1.01 \times 10^7$  A/W, a high EQE of  $5.02 \times 10^9\%$ , a sensitive detectivity of  $2.98 \times 10^{15}$  Jones, and a fast rise time of 0.2 s under 250 nm illumination. In addition, first-principle calculations indicated that  $\beta$ - $\text{Ga}_2\text{O}_3$  nanosheets had good stability in terms of oxidation and moisture resistance, without significant performance degradation. Vieira et al. improved the performance by adding a third metal electrode to a traditional Schottky diode, resulting in a two-Schottky-diode-coupled device (Figure 17d) [135]. This device exhibited good properties with a low dark current, a rectification ratio of  $1.7 \times 10^7$ , and a high forward current of 2 mA (Figure 17e,f).

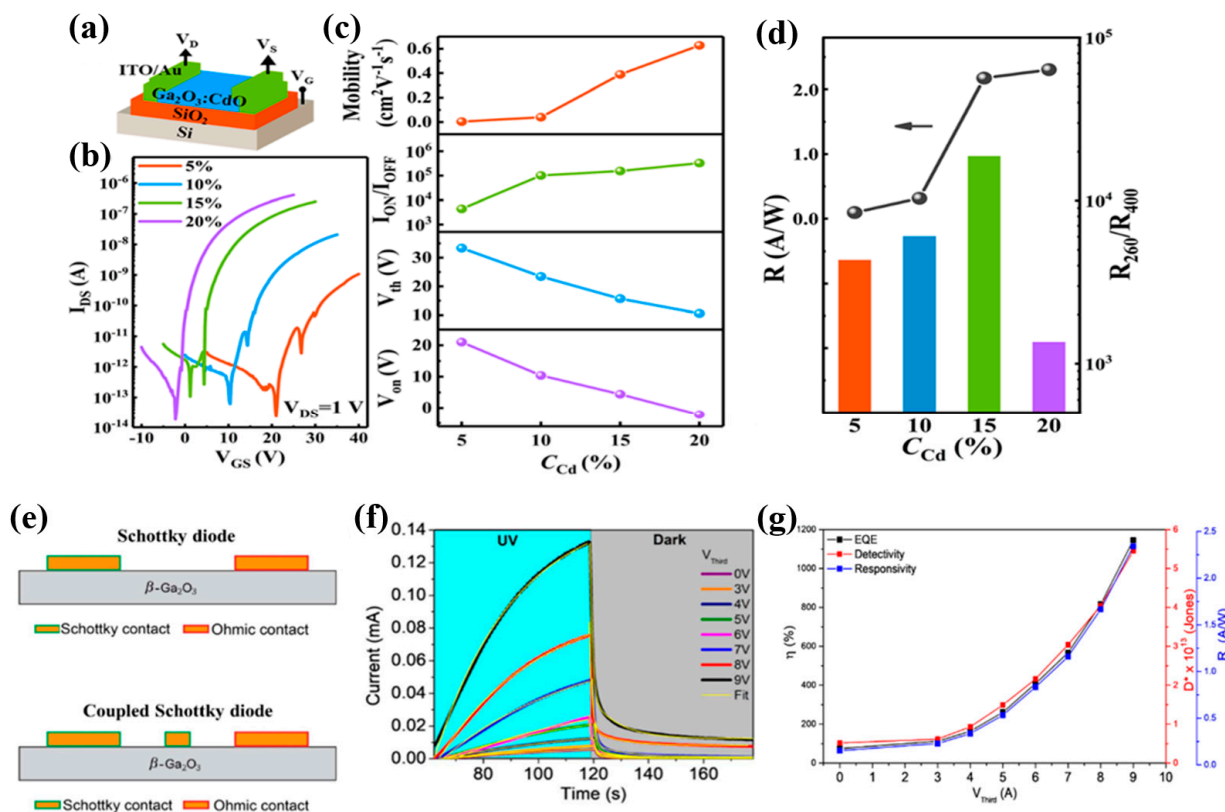


**Figure 17.** (a) Schematic structure of TFT photodetector. (b) Transfer curves of Ga<sub>2</sub>O<sub>3</sub>:CdO TFTs with C<sub>Cd</sub> value of 5–20% at V<sub>DS</sub> = 1 V. (c) Electrical parameters, (d) responsivity of Ga<sub>2</sub>O<sub>3</sub>:CdO TFTs with different C<sub>Cd</sub> [131]. (e) Cross-section of the β-Ga<sub>2</sub>O<sub>3</sub> devices of the conventional Schottky diode (top) and coupled Schottky diode (below). (f) Rise and decay curves for photocurrent of the coupled Schottky diode in the dark and under UV for different voltages bias at the third electrode. (g) Responsivity, EQE, and detectivity as a function of the third electrode voltage for the coupled Schottky diodes [135].

### 5.3. Ga<sub>2</sub>O<sub>3</sub> Heterostructures

Heterojunction devices by combining Ga<sub>2</sub>O<sub>3</sub> with other materials such as SnO<sub>2</sub> [136], ZnO [137], graphene [138,139], CuO [140], V<sub>2</sub>O<sub>5</sub> [141], NiO [142], CFP [143], and PANI [144] have been fabricated to optimize the performance of Ga<sub>2</sub>O<sub>3</sub> based photodetectors. For instance, Sn-doped Ga<sub>2</sub>O<sub>3</sub> incorporated with SnO<sub>2</sub> nanostructures was grown on a c-plane sapphire substrate, followed by the fabrication of an MSM photodetector using Pt as electrodes [136]. Under 254 nm UV illumination, the photodetector possessed a low dark current of 21 nA at 50 V bias, an ultrahigh photo-to-dark current ratio of  $9 \times 10^4$ , and a high responsivity of 1532 A/W. Kong et al. reported a simple DUV photodetector that was fabricated by directly transferring a layer of multilayer graphene (MLG) film on an n-type Ga<sub>2</sub>O<sub>3</sub> wafer (Figure 18a) [138]. The Raman spectrum of the MLG film and the β-Ga<sub>2</sub>O<sub>3</sub> wafer is shown in Figure 18b. The MLG/Ga<sub>2</sub>O<sub>3</sub> heterojunction device presented pronounced rectifying characteristics under DUV light illumination (Figure 18c). Wang et al. fabricated high-responsivity DUV photodetectors based on a nitrogen-doped graphene (NGr)/β-Ga<sub>2</sub>O<sub>3</sub> microwire p-n heterojunction, as shown in Figure 18d [139]. The photodetector exhibited an ultrahigh responsivity of 360 mA/W and an ultrahigh light-to-dark ratio of 10<sup>4</sup> under 0 V and 235 nm illumination with a light intensity of 12.2 μW/cm<sup>2</sup> (Figure 18e,f).

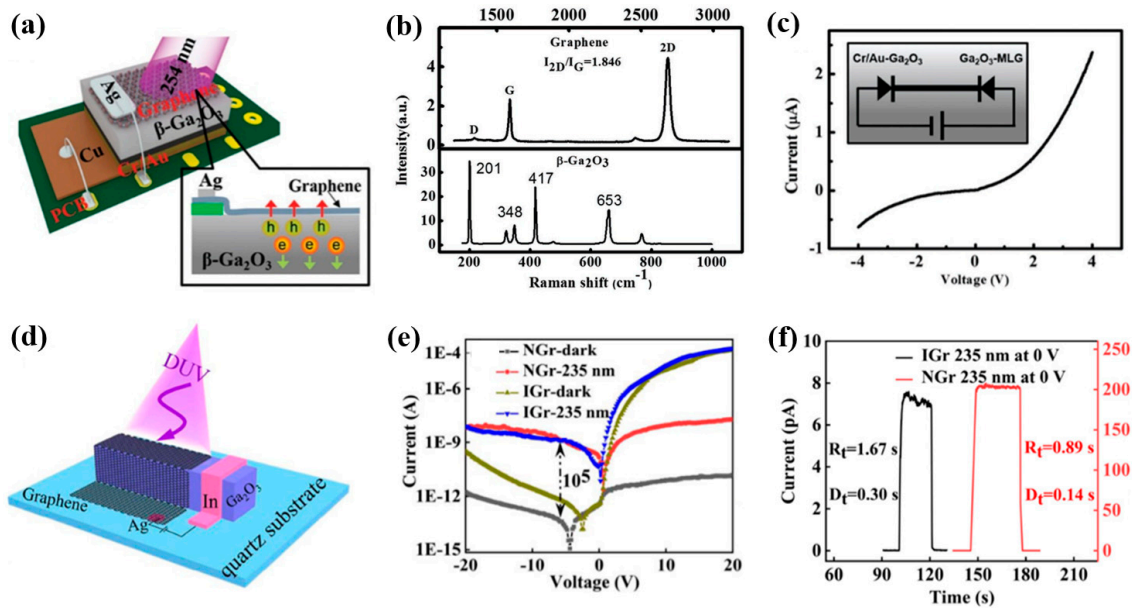


**Figure 18.** (a) Schematic diagram of the MLG/ $\beta$ -Ga<sub>2</sub>O<sub>3</sub> wafer photodetector. (b) Raman spectrum of the MLG film and  $\beta$ -Ga<sub>2</sub>O<sub>3</sub> wafer. (c) I–V characteristics of the photodetector. Inset: device model of two back-to-back Schottky diodes [138]. (d) Device schematic of NGr/ $\beta$ -Ga<sub>2</sub>O<sub>3</sub> microwires heterojunction. (e) I–V curves of the NGr/ $\beta$ -Ga<sub>2</sub>O<sub>3</sub> and IGr/ $\beta$ -Ga<sub>2</sub>O<sub>3</sub> heterojunction photodetectors under dark and 235 nm illumination. (f) Time response of  $\beta$ -Ga<sub>2</sub>O<sub>3</sub>/IGr and  $\beta$ -Ga<sub>2</sub>O<sub>3</sub>/NGr heterojunction photodetector [139].

Kumar et al. fabricated n-Ga<sub>2</sub>O<sub>3</sub>/p-CuO quasi-heterostructure-based DUV photodetectors that exhibited extraordinary photodetection characteristics, such as a very low dark current of  $6.94 \times 10^{-14}$  A, a high responsivity of  $6.33 \times 10^3$  A W<sup>-1</sup>, a very high detectivity of  $4.44 \times 10^{14}$  mHz<sup>0.5</sup>W<sup>-1</sup>, and an exceptional EQE of  $3.1 \times 10^6\%$  at 5 V [140]. An obvious photovoltaic effect with an open-circuit voltage of 0.4 V was demonstrated in the Ga<sub>2</sub>O<sub>3</sub>/V<sub>2</sub>O<sub>5</sub> heterostructure [141]. Following irradiation with 254 nm DUV light, the device displayed a dark current of 2 fA, a high PDCR of  $2.6 \times 10^7$ , a fast rise/decay time of 67/26 ms, a responsivity of 19.8 mA/W, a detectivity of  $7.8 \times 10^{13}$  Jones, and an  $R_{240}/R_{400}$  of  $6.02 \times 10^4$  under 0 V bias (Figure 19a,b). Yu et al. fabricated a self-powered photodetector based on the  $\beta$ -Ga<sub>2</sub>O<sub>3</sub>/NiO heterojunction and used synthesized platinum (Pt) NPs for surface modification of the device [142]. The device exhibited an ultralow dark current of 1.09 nA at –15 V and a large  $I_{\text{photo}}/I_{\text{dark}}$  ratio of 9153, together with a detectivity of  $4.2 \times 10^9$  Jones, an ultrahigh linear dynamic range of 79 dB, and a responsivity of 4.27 mA/W, (Figure 19c–f).

By constructing a solid/liquid heterojunction based on 3D a-Ga<sub>2</sub>O<sub>3</sub>/CFP core–shell structures, a new type of solar-blind PEC-PD was fabricated [143]. The built-in electric field could effectively separate electron–hole pairs, promoting the self-powered ability of this PEC-type photodetector. The device exhibited a maximum responsivity of about 12.90 mA W<sup>-1</sup> and a fast photoresponse time of approximately 0.15/0.13 s without external bias potential. The heterojunction formed by Ga<sub>2</sub>O<sub>3</sub> microwires and organic materials polyaniline (PANI) was also studied [144]. In the absence of an external power source, the self-powered DUV photodetector manufactured exhibited an ultrahigh response of 21 mA W<sup>-1</sup> at 246 nm, with a sharp cutoff wavelength of 272 nm. In addition, the dark current is 0.08 pA, which was smaller than almost all previous metal-oxide-based solar-blind photodetectors.

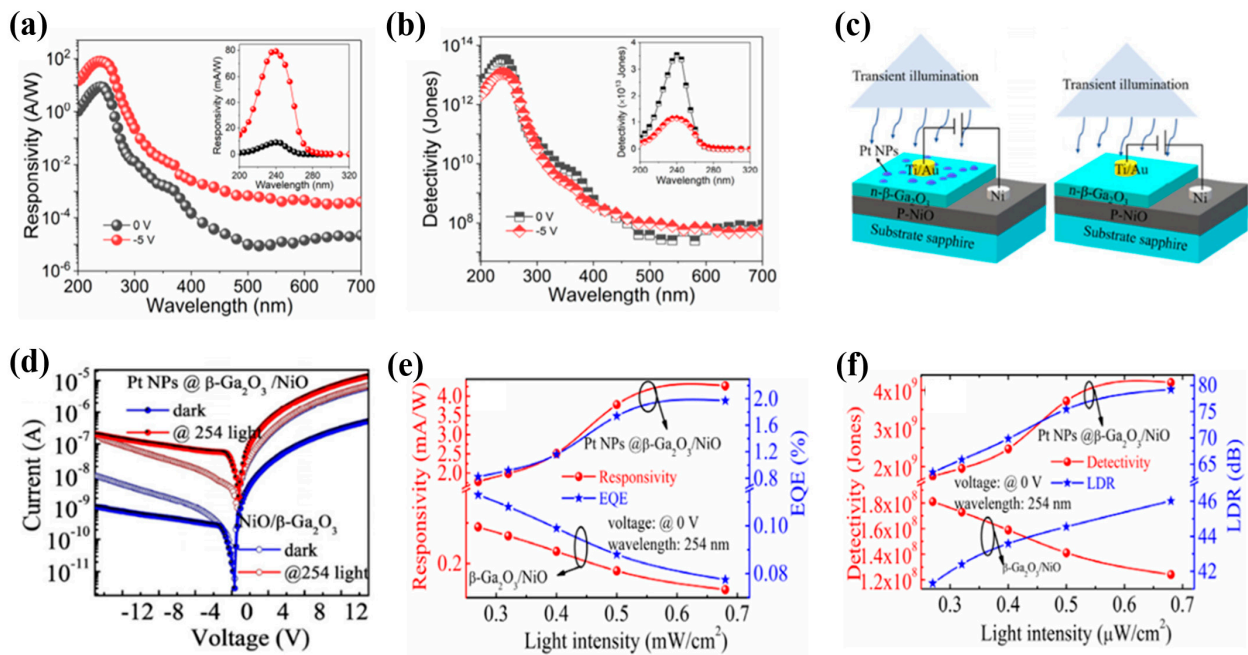


**Figure 19.** (a) Responsivity and (b) detectivity of Ga<sub>2</sub>O<sub>3</sub>/V<sub>2</sub>O<sub>5</sub> heterostructure under biases of 0 and −5 V. Inset: high-resolution linear spectral responsivity and detectivity [141]. (c) Schematic of the β-Ga<sub>2</sub>O<sub>3</sub>/NiO heterojunction with and without Pt NPs. (d) I–V curves of the heterojunction photodetectors with and without Pt NPs. (e) Light–intensity–dependent responsivity and EQE detectivity. (f) LDR of β-Ga<sub>2</sub>O<sub>3</sub>/NiO heterojunction photodetectors without and with Pt NPs [142].

In conclusion, nanostructures, thin films, and heterostructures of Ga<sub>2</sub>O<sub>3</sub> material have been extensively studied. There are many studies on Ga<sub>2</sub>O<sub>3</sub> defects, conductive mechanisms, doping, annealing, and heterojunction formation. To date, most DUV detection studies have been based on β-Ga<sub>2</sub>O<sub>3</sub> and made good progress. Other phases, especially amorphous gallium oxide, have gradually attracted attention due to their cost and performance. Table 6 summarizes the performance parameters of Ga<sub>2</sub>O<sub>3</sub> DUV photodetectors.

**Table 6.** Summary of performance parameters of DUV photodetectors based on Ga<sub>2</sub>O<sub>3</sub>.

Device Structure	Fabrication Method	Light of Detection/nm	Dark Current	On/Off Ratio	Rejection Ratio	Specific Detectivity/Jones	EQE	Responsivity	Rise Time/Decay Time	Ref.
β-Ga <sub>2</sub> O <sub>3</sub> nanowires	CVD	255	2.44 × 10 <sup>-10</sup>	~10 <sup>2</sup>			0.39	0.8 mA/W @10 V		[106]
β-Ga <sub>2</sub> O <sub>3</sub> nanowires	CVD	255		~10 <sup>2</sup>				3.4 mA/W @5 V		[107]
β-Ga <sub>2</sub> O <sub>3</sub> nanowires	Thermal oxidation	254	10 <sup>-11</sup> @-30 V	~10 <sup>2</sup>				0.6 mA/W @10 V	1 μs/64 μs	[108]
β-Ga <sub>2</sub> O <sub>3</sub> nanowires	CVD	250	10 <sup>-11</sup>	10 <sup>3</sup>			2 × 10 <sup>5</sup>	377 A/W	0.21 s/7.11 s	[109]
Ga <sub>2</sub> O <sub>3</sub> nanobelts	CVD	250		1.1 × 10 <sup>4</sup>	UV/vis 10 <sup>6</sup>		187	37.6 A/W	11.8 s <0.3 s	[110]
Ga <sub>2</sub> O <sub>3</sub> nanobelts	CVD	254	10 <sup>-10</sup>	10 <sup>4</sup>			9.4 × 10 <sup>3</sup>	19.3 A/W @1 V	<0.02 s	[111]
β-Ga <sub>2</sub> O <sub>3</sub> microbelts	Mechanical exfoliation	254	7.75 uA		254/365 2.93	7.05 × 10 <sup>11</sup>	8.8 × 10 <sup>5</sup>	1.8 × 10 <sup>5</sup> A/W @-30 V	0.76 s/1.78 s @0 V	[114]
β-Ga <sub>2</sub> O <sub>3</sub> nanosheets	CVD	254				4 × 10 <sup>12</sup>	1600	3.3 A/W @10 V	30 ms/60 ms	[113]

Table 6. Cont.

Device Structure	Fabrication Method	Light of Detection/nm	Dark Current	On/Off Ratio	Rejection Ratio	Specific Detectivity/Jones	EQE	Responsivity	Rise Time/Decay Time	Ref.
$\beta$ -Ga <sub>2</sub> O <sub>3</sub> flakes MSM	Mechanical exfoliation	254	0.28 pA	$1.37 \times 10^3$	254/365 $1.92 \times 10^3$	$3.73 \times 10^{10}$		1.68 A/W @30 V	1.76 s/ 0.53 s	[115]
Ga <sub>2</sub> O <sub>3</sub> film MSM	MBE	266		50	UVC/vis >10 <sup>3</sup>			0.21 A/W @5 V	0.48 s/ 0.58 s	[117]
Ga <sub>2</sub> O <sub>3</sub> film MSM	PLD	255		10 <sup>4</sup>	UV/vis 10 <sup>4</sup>			0.7 A/W @5 V	2.4 s/ 1.6 s	[118]
Ga <sub>2</sub> O <sub>3</sub> film MSM	PE-ALD	250			UV/vis $5.97 \times 10^4$	$8.74 \times 10^{12}$		22.19 A/W @5 V		[121]
Ga <sub>2</sub> O <sub>3</sub> film MSM	Sputter	230		$1.78 \times 10^5$				0.553 A/W @5 V	2 s/0.1 s	[122]
Al: Ga <sub>2</sub> O <sub>3</sub> film MSM	Sputter	230				$1.2 \times 10^{13}$	708	1.38 A/W @5 V		[125]
Al: Ga <sub>2</sub> O <sub>3</sub> film MSM	Sputter	230			UV/vis $1.55 \times 10^3$	$1.37 \times 10^{11}$		70 mA/W @5 V		[126]
Zr: Ga <sub>2</sub> O <sub>3</sub> film p-i-n	Sputter	185			10 <sup>4</sup>		23.6	35 mA/W @0 V	0.12 s/ 0.08 s	[128]
Sn: Ga <sub>2</sub> O <sub>3</sub> film MSM	Sol-gel preparation	254	0.76 nA	$6 \times 10^3$		$3.21 \times 10^{12}$		164 mA/W @30 V	0.42 s/ 0.20 s	[129]
Cd: a-Ga <sub>2</sub> O <sub>3</sub> film TFT	Spin-coating	260			UV/vis $1.88 \times 10^4$	$1.71 \times 10^{12}$	1036	2.17 A/W @0.2 V		[131]
a-Ga <sub>2</sub> O <sub>3</sub> film TFT	Sputter	250			UV/vis 10 <sup>3</sup>	10 <sup>15</sup>		10 <sup>4</sup> A/W@6 V		[133]
$\beta$ -Ga <sub>2</sub> O <sub>3</sub> film TFT	Mechanical exfoliation	250				$2.98 \times 10^{15}$	$5.02 \times 10^9$	$1.01 \times 10^7$ A/W @0.5 V	0.2 s/	[134]
$\beta$ -Ga <sub>2</sub> O <sub>3</sub> film TFT	-	254				$5.45 \times 10^{13}$	$1.15 \times 10^3$	2.34 A/W @9 V	29.38 s/	[135]
$\beta$ -Ga <sub>2</sub> O <sub>3</sub> /SnO <sub>2</sub> Heterojunction MSM	LPCVD	254	21 nA	$9 \times 10^4$		$1.7 \times 10^{15}$	$7.4 \times 10^5$	1532 A/W @50 V	0.5 s/ 0.2 s	[136]
$\beta$ -Ga <sub>2</sub> O <sub>3</sub> /SnO <sub>2</sub> Heterojunction MSM	LPCVD	302				$2.97 \times 10^{14}$	$1 \times 10^5$	262 A/W @50 V	26 s/ 3 s	[136]
Gr/ $\beta$ -Ga <sub>2</sub> O <sub>3</sub> heterojunction	CVD	254				$5.92 \times 10^{13}$	$1.96 \times 10^4$	39.3 A/W @20 V	94.83 s/ 219.19 s	[138]
N: Gr/ $\beta$ -Ga <sub>2</sub> O <sub>3</sub> heterojunction	CVD	235		10	235/280 $1.5 \times 10^2$	$4 \times 10^{10}$	8.8	12 mA/W @0 V	1.67 s 0.3 s	[139]
N: Gr/ $\beta$ -Ga <sub>2</sub> O <sub>3</sub> heterojunction	CVD	235		10 <sup>4</sup>	DUV/UV $6.4 \times 10^2$	$1.3 \times 10^{12}$	190	360 mA/W @0 V	0.89 s 0.14 s	[139]
$\beta$ -Ga <sub>2</sub> O <sub>3</sub> /CuO heterojunction p-n	Electro spraying	254	$6.94 \times 10^{-14}$	$2.99 \times 10^6$		$4.44 \times 10^{14}$	$3.1 \times 10^6$	$6.33 \times 10^3$ A/W @5 V		[140]
Ga <sub>2</sub> O <sub>3</sub> /V <sub>2</sub> O <sub>5</sub> heterostructure p-n	MOCVD	254	2 fA	$2.6 \times 10^7$	240/400 $6.02 \times 10^4$	$7.8 \times 10^{13}$	9.7	19.8 mA/W @0 V	67 ms/ 26 ms	[141]
$\beta$ -Ga <sub>2</sub> O <sub>3</sub> /NiO heterojunction p-n	PLD	254	1.09 nA	$9.15 \times 10^3$		$4.2 \times 10^9$		4.27 mA/W @-15 V	4.6 ms/ 7.6 ms	[142]
a-Ga <sub>2</sub> O <sub>3</sub> /CFP core-shell composites PEC	Sputter	254						12.9 mA/W @0 V	0.15 s/ 0.13 s	[143]
$\beta$ -Ga <sub>2</sub> O <sub>3</sub> /PANI heterojunction	CVD	246	0.08 pA		UV/vis 10 <sup>2</sup>			21 mA/W @0 V		[144]

## 6. DUV PDs Based on Diamond Material

Diamond is divided into natural diamond and artificial diamond. Natural diamonds are limited in quantity and expensive. In order to reduce the cost, a series of synthetic methods have been developed to prepare synthetic diamonds. In 1955, Bundy and others of the General Electric Company adopted the high-temperature and high-pressure (HPHT) method to synthesize synthetic diamond for the first time [145]. The preparation of diamond by the CVD method has also been studied, and the real breakthrough of the CVD method came from the discovery of Angus et al. in the late 1960s: atomic hydrogen in the deposition atmosphere can selectively etch graphite [146,147]. At present, the research on the growth of diamond film has reached a certain level, and the deposition theory has also been improved. Diamond is an indirect-bandgap (5.5 eV) semiconductor with high resistivity, thermal conductivity, breakdown voltage, and carrier mobility, which has great potential in making radiation detectors. Radiation detectors made from diamond have high charge collection

efficiency and can work normally under high working voltages and high temperatures without an additional refrigeration device [148].

### 6.1. Diamond Thin Films

The successful development of high-quality CVD diamond film has opened up a new path for the research and development of diamond radiation detectors [13]. To date, a number of diamond-based photoconductors have been fabricated by choosing Ti, Ti/Au, and tungsten carbide (WC) as electrode materials, which can form Ohms contacts with diamond [149–153]. For example, Liao et al. reported high-performance planar photoconductors based on unintentionally doped homoepitaxial diamond thin films [150]. At the applied voltage of 20 V, the dark current was 1 pA; when irradiated with light at a 220 nm wavelength, the photoconductors exhibited a high responsivity of about 6 A/W, a non/off ratio of  $10^4$ , and a photoconductivity gain of 33. The effect of passivation treatment of a single-crystal diamond (SCD) substrate on detection performance was studied by Bevilacqua et al. [151]. The passivation treatment led to highly effective photoconductive devices, which displayed 6 orders of discrimination between DUV and visible light and a responsivity as high as 100 A/W.

MSM photodetectors based on diamond films have also received wide research interest [154–162]. For example, Feng et al. fabricated an MSM-structured diamond DUV photodetector with a large active area of  $3.093 \text{ mm}^2$  [154], the I-V characteristics, responsivity, and EQE of which were  $56.3 \text{ A W}^{-1}$  and 328, respectively (Figure 20a,b), at 50 V bias under 213 nm illumination. Liao et al. investigated the influence of electrode spacing on MSM devices [156]. Photodetectors were fabricated on a homoepitaxial diamond thin film grown on an Ib-type diamond substrate, the DUV responsiveness of which was increased significantly by reducing the electrode spacing. The reduction in the electrode spacing enabled the full depletion of the spacing at low biases, providing a higher responsivity. Single-crystal diamond samples with asymmetric Schottky contacts were used for the fabrication of vertical MSM for DUV radiation [155], which had an ultraviolet to visible-light rejection ratio of  $6.8 \times 10^3$ .

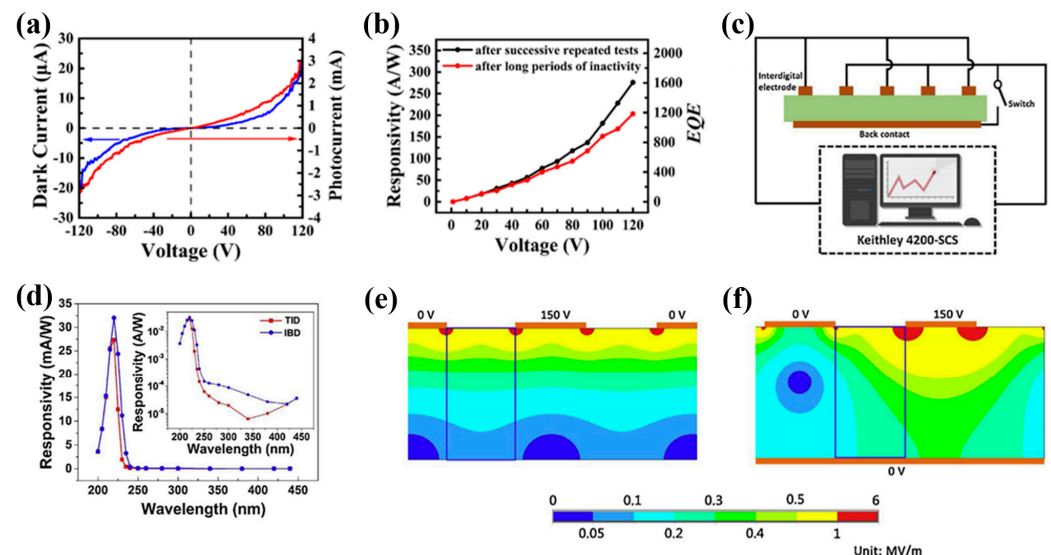


**Figure 20.** (a) I–V characteristics of MSM-structured diamond DUV photodetector under dark condition and 213 nm illumination ( $3.125 \mu\text{W mm}^{-2}$ ). (b) Stable responsivity and EQE of the photodetector [154]. (c) Circuit diagram of the interdigitated electrode with back-contact diamond detector. (d) Spectral responsivities. Inset: logarithmic view of the spectral responsivities. Simulations of the electric field strength: (e) traditional planar interdigitated detector (TID). (f) Interdigitated electrode with back-contact detector (IBD). Blue-outlined rectangles in (e,f) indicate photosensitive area [157].

To improve the detectivity, a diamond DUV detector with an interdigitated electrode structure accompanying a back electrode with switch-controlled connectivity was fabricated (Figure 20c) [157]. After activation of the back-electrode contact, higher responsivity and detectivity were observed (Figure 20d). The results of the electrical field simulation shown in Figure 20e,f demonstrate that a stronger electrical field formed over the diamond region in the device with the back electrode, leading to higher carrier collection efficiency. The extrinsic photoresponse could be suppressed through post-treatment in a plasma of oxygen and carbon tetrafluoride at room temperature [158]. The photoresponsivity between the UV and visible-light regions could be improved because of the effective removal of the  $sp^2$ -bonded carbon impurities and the passivation of the silicon-vacancy defects in the diamond.

In order to homogenize the electric field spatial distribution of the planar structure, 3D electrode structures have been developed recently [159–162]. For instance, Liu et al. fabricated a photovoltaic 3D diamond UV detector using the bottom-up method [159]. The fabrication process of the 3D diamond PDs is depicted in Figure 21a. At a reverse bias of 10 V, the dark current was 14.2 pA, indicating a  $10^5$  reduction compared with that of the photoconductive detector shown in Figure 21b. The transient response measurement indicated that the decay time of the photovoltaic detector was approximately 590 ms, and the PPC phenomenon was weak (Figure 21c). The significant reduction of the dark current and PPC can be attributed to the formation of a Schottky barrier between W and oxygen-terminated diamond. Another group designed and fabricated an ultraviolet detector on a single-crystal CVD diamond with 3D metal electrodes [160]. Figure 21d shows the schematic view of UV detector geometries. The dark current revealed almost identical behavior, symmetric to polarity, while the groove-shaped structure demonstrated an enhanced sensitivity of 36% compared with the planar structure (Figure 21e,f).

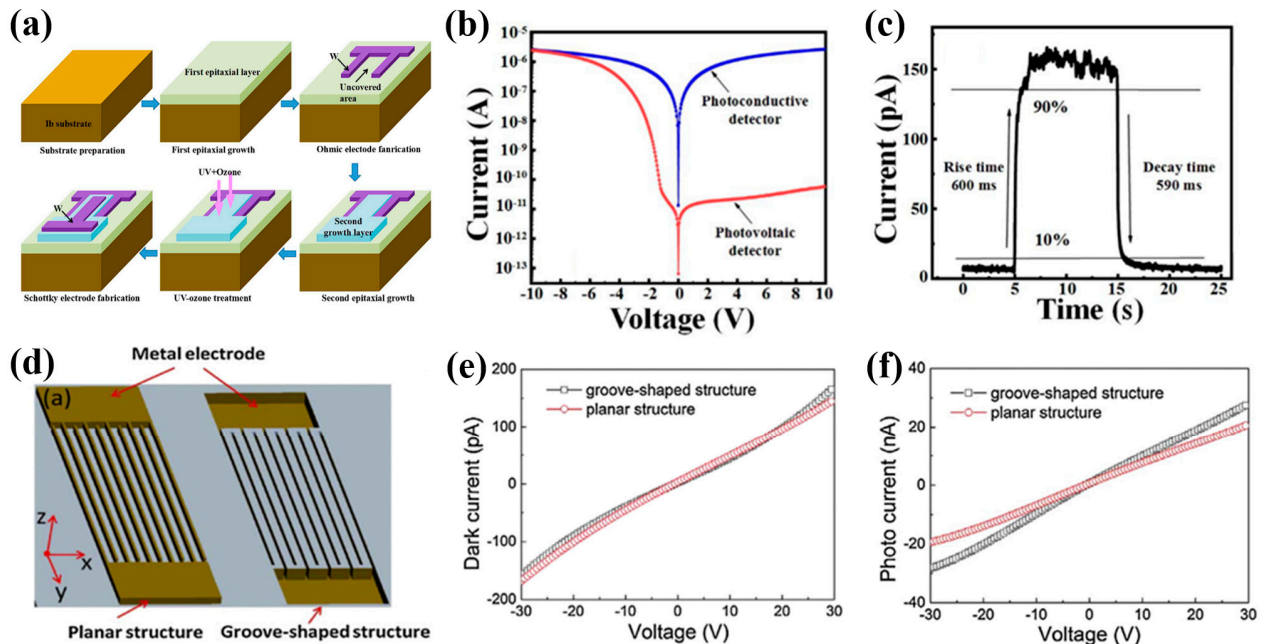


**Figure 21.** (a) Fabrication process of the 3D diamond photovoltaic detector. (b) I–V characteristics of photovoltaic and photoconductive detector under dark conditions. (c) Time-dependent photocurrent of the detector under 5 V and 210 nm illumination [159]. (d) Schematic view of UV detector geometries with groove-shaped electrode (right) and the in-plane electrode structure (left). (e) Dark current and (f) photocurrent (220 nm) vs. voltage for planar and groove-shaped electrode structures [160].

The diamond-based Schottky photodiode is one of the most studied device geometries for solar-blind DUV photodetection. The effects of the photocurrent gain mechanism of Schottky devices and the trap state color center on the response have been studied [163–170].

Lin et al. constructed all-carbon solar-blind photodetectors based on diamond with interdigitated graphite as electrodes [163]. Graphite electrodes were made by laser-induced graphitization of diamond (Figure 22a). The peak responsivity of the photodetector was  $21.8 \text{ A W}^{-1}$ , and the detectivity was  $1.39 \times 10^{12} \text{ cm Hz}^{1/2} \text{ W}^{-1}$  when the bias voltage was 50 V (Figure 22b,c). Liu et al. fabricated self-powered DUV detectors using high-quality Ru/diamond Schottky diodes [170]. Oxygen-terminated diamond was used because of its stable property and surface band bending. A dark current of 0.007 pA without an applied bias was obtained, and a rectification ratio of  $5.7 \times 10^8$  indicated the good quality of the Schottky diode.

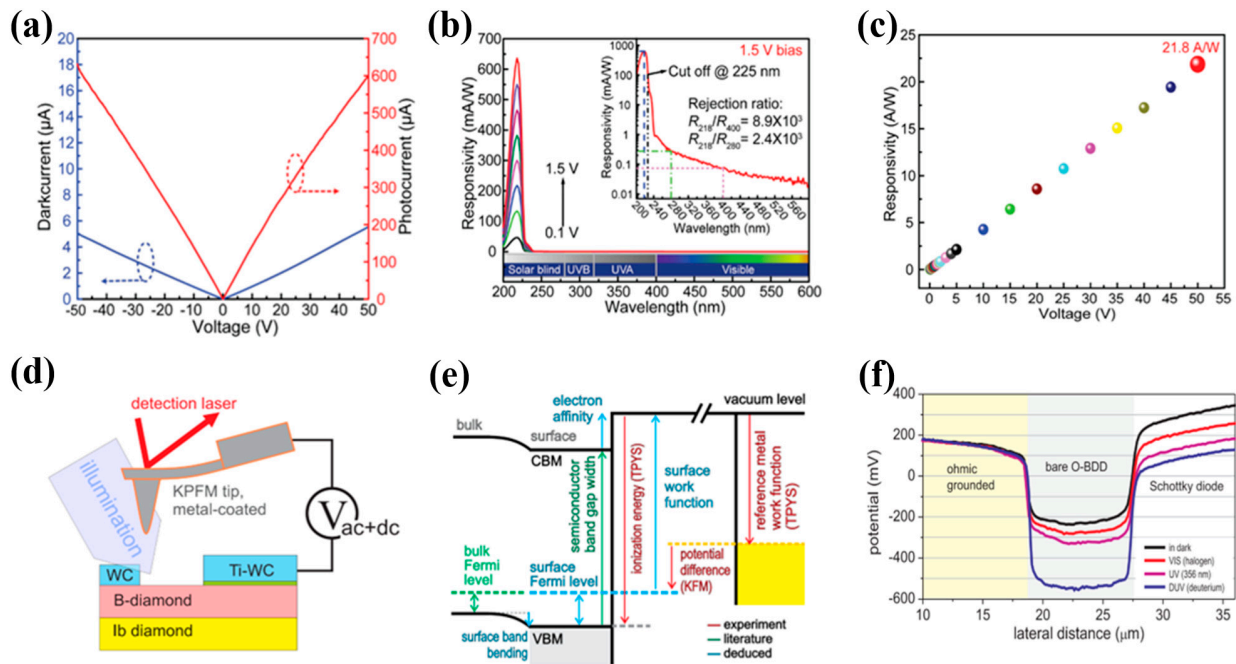


**Figure 22.** (a) Dark current and photocurrent under the illumination of a 150 W xenon lamp. (b) Photoresponse of the diamond photodetector. Inset: response spectrum under 1.5 V bias. (c) Dependence of the maximum responsivity of the photodetector on the bias applied [163]. (d) Schematic diagram of the experimental equipment. (e) Schematic guideline for construction of surface and sub-surface energetic band. (f) KPFM potential profiles across the diamond Schottky photodiode [167].

As shown in Figure 22d, a Schottky photo-diode made of a tungsten carbide (WC) layer on an oxygen-terminated boron-doped diamond epitaxial layer (O-BDD) [167]. From the Kelvin probe force microscopy (KPFM) data in dark and under illumination, it can be found that the photovoltage on the electrically floating Schottky contact was directly corresponding to the shift of Fermi level inside the BDD channel below the contact, and the reason for how this small photovoltages ( $\leq 210 \text{ mV}$ ) led to orders of magnitude difference in photocurrents was explained (Figure 22e,f). A homoepitaxial diamond photodetector with two non-Ohmic contacts connected back-to-back was fabricated [168]. The photocurrent gain was observed to originate from a metal/diamond interface trap center. The DUV light illumination produced a thin interface barrier layer at the metal/diamond interface due to the existence of interface traps. Mohapatra et al. correlated the DUV current response of single-crystal diamond photodetectors to the lifetimes of nitrogen-induced color centers [169]. The relationship between the charge carrier dynamics of the dominant color centers and the response was analyzed quantitatively through DUV response, PL, and time-resolved photoluminescence (TR-PL) measurements. The faster component of the decay can be associated with the Shockley–Read–Hall nonradiative recombination, which decreased with the increase in nitrogen concentration.

Liu et al. fabricated a (001)-oriented single-crystal diamond p-i-n junction DUV detector [171], which exhibited a clear, rectifying I–V characteristic with a rectification ratio of 223 at 5 V. At a reverse bias of 5 V, the responsivity was 1.69 A/W under 210 nm light, and the UV-to-visible rejection ratio reached  $10^3$ . The time response characteristic showed a long rise time and decay time, which were mainly caused by the carrier trapping in the n-type diamond layer. Lei et al. used the microwave plasma CVD method to homoepitaxially epitaxial diamond film on an HPHT diamond substrate, and a metal–semiconductor field-effect transistor (MESFET) solar-blind detector was fabricated based on the prepared films [172]. The typical output characteristic curve of the diamond MESFET device is shown in Figure 23a. The detector exhibited a light-to-dark ratio greater than 3 orders of magnitude.

## 6.2. Diamond Heterostructures

A vertical graphene/microcrystalline diamond (MCD)/metal structure was constructed as the photodiode device for solar-blind ultraviolet detection [173]. The I–V characteristics were measured both in dark and under illumination at different wavelengths. The results showed the device presented high responsivity under UV illumination and a high UV/solar rejection ratio. Nitrogen-doped (3%) ultrananocrystalline diamond/hydrogenated amorphous carbon (UNCD/a-C:H) films were grown by coaxial arc plasma deposition, and a heterojunction with a p-type Si substrate was fabricated [174]. C–V measurements assured the expansion of a depletion region into the film side (Figure 23b). The relationship between detectivity and temperature was also researched, as shown in Figure 23c. Chen et al. combined  $\text{Ga}_2\text{O}_3$  with diamond to obtain a self-driven DUV photodetector [175]. Figure 23d,e shows the I–V characteristic and response spectrum. The photodetector exhibited a peak responsivity of 0.2 mA/W, a sharp cutoff wavelength at 270 nm, and a UV/visible rejection ratio of more than 2 orders of magnitude. By using the self-powered photodetector as the sensing pixel of the imaging system, high-quality images were obtained, indicating that the device may be used for desorption areas without a power supply (Figure 23f).

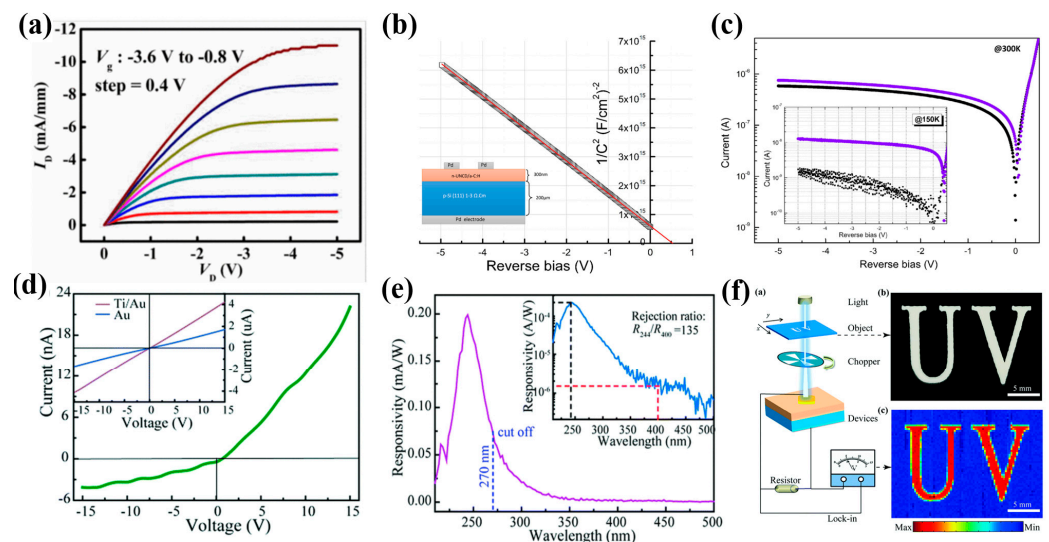


**Figure 23.** (a) Diamond MESFET device output characteristic curve [172]. (b)  $1/C^2$  of heterojunction against reverse bias. Inset: schematic diagram of the heterojunction. (c) I–V characteristics in the dark and under illumination at 300 K and 150 K (inset) [174]. (d) I–V characteristics of the device under dark conditions. Inset: I–V curve of the Au contact on the diamond and the Ti/Au contact on the  $\beta\text{-Ga}_2\text{O}_3$ . (e) Photoresponse spectra of the diamond/ $\beta\text{-Ga}_2\text{O}_3$  photodetector at 0 V bias. Inset: photoresponse spectrum in a logarithmic scale. (f) Schematic illustration of the imaging system and images employing the diamond/ $\beta\text{-Ga}_2\text{O}_3$  heterojunction photodetector as sensing pixel under 0 V bias [175].

In summary, diamonds used for DUV detection are mostly synthesized by CVD methods and are mostly thin-film materials. Diamond has great potential in the field of space detection due to its radiation resistance and high thermal conductivity. The performance parameters of DUV photodetectors based on diamond are summarized in Table 7. It can be found that these photodetectors can achieve a dark current of pA and a response time of ns, with the responsivity ranging from  $10^{-4}$  to  $10$  A W $^{-1}$ .

**Table 7.** Summary of performance parameters of DUV photodetectors based on diamond.

Device Structure	Fabrication Method	Light of Detection/nm	Dark Current	On/Off Ratio	Rejection Ratio	Specific Detectivity/Jones	EQE	Responsivity	Rise Time/Decay Time	Ref.
B: diamond film Photoconductor	CVD	220	<1 pA	>10 <sup>7</sup>	210/630 >10 <sup>6</sup>					[149]
diamond film Photoconductor	PECVD	220	1 pA		DUV/vis 10 <sup>8</sup>			6 A/W@3 V	<10 ns	[150]
diamond film MSM	CVD	210	0.368 pA		UV/vis 50			7.86 mA/W @8 V		[176]
diamond film MSM	MPCVD	213			UV/vis 9.6 × 10 <sup>3</sup>	1.26 × 10 <sup>13</sup>	328	56.3 A/W @50 V	1.03 ns/1.05 ns	[154]
diamond film MSM	CVD	225			225/400 6.8 × 10 <sup>3</sup>	1.91 × 10 <sup>12</sup>	1029 @470 V	0.19 mA/W @9 V	2 ns/20 ns	[155]
diamond film 3D-MSM	MPCVD	210	14.2 pA @5 V		215/400 276				600 ms/590 ms	[159]
diamond film 3D-MSM	HPHT	215			215/600 2 × 10 <sup>3</sup>			5.32 mA/W @2 V		[161]
diamond film Schottky	MPCVD	218			UV/vis 218/400 8.9 × 10 <sup>3</sup>	1.39 × 10 <sup>12</sup>		21.8 A/W @50 V		[163]
diamond film Schottky	MPCVD	220			DUV/vis 10 <sup>6</sup> @30 V 10 <sup>8</sup> @−23 V		20@30 V 10,000@−23 V	37 mA/W @30 V 18 A/W @−23 V 10 A/W @100 V	<0.3 s @30 V ~10 s @−23 V	[164]
diamond film Schottky	CVD	UV			UV/vis 10 <sup>4</sup> ~10 <sup>5</sup>			16.2 mA/W@0 V	1~10 ms	[165]
B: diamond film p-i-n	MPCVD	220	7 fA	2 × 10 <sup>5</sup>	UV/vis 10 <sup>3</sup>	3.8 × 10 <sup>12</sup>		1.69 A/W @5 V		[170]
UNCD/a-C:H heterojunctions p-n	Plasma deposition	254				5.11 × 10 <sup>10</sup>	65	134 mA/W @−5 V		[174]
diamond/β-Ga <sub>2</sub> O <sub>3</sub> heterojunctions p-n	MPCVD	244		37@0 V	UV/vis 1.4 × 10 <sup>2</sup>	6.9 × 10 <sup>9</sup>		0.2 mA/W @0 V		[175]

## 7. Conclusions and Challenges

Inorganic materials such as III-nitride compounds, Ga<sub>2</sub>O<sub>3</sub>, diamond, etc., have good deep ultraviolet light absorption properties, making them ideal DUV detection materials. DUV detection materials with various morphologies, such as bulk, thin films, nanowires, nanoribbons, and two-dimensional single-crystal films, have been obtained by using different growth techniques. Based on these materials, various types of DUV detectors have been developed, which have achieved good results in light sensitivity, dark current, responsivity, detection rate, photoresponse rejection ratio, response cutoff, response speed, etc. Although DUV materials have made some breakthroughs in the field of DUV detection, some properties are far from meeting the requirements of practical applications, which requires further development of DUV detection materials.

The field of boron nitride-based photodetectors is still in a very early stage of development, mainly because of insufficient h-BN thin-film quality. A lot of work remains to be carried out to achieve the commercial detection of materials. In addition, methods for intentional doping of BN films, in particular n-type, are still somewhat immature, preventing the fabrication of high-quality p-n junctions. Further progress towards practical BN-based electronic devices requires serious efforts in the development of thin-film deposition and doping techniques.

Aluminum nitride is similar to boron nitride, and it is difficult to achieve n-type doping, which limits the heterojunction formation. Many fundamental questions and

phenomena related to the growth mechanism of AlN nanowires and films are still not well understood and need further investigations, affecting the growth quality of materials.

AlGaN-based DUV detectors have been successfully explored and commercialized at present, but the materials are expensive to prepare, and the optical band gap needs to be adjusted by accurately doping other elements to reach the expected absorption wavelength range. A high Al component of  $\text{Al}_x\text{Ga}_{1-x}\text{N}$  alloying epitaxial film requires a high growth temperature. Due to current technology, the dislocation density in heteroepitaxial-grown AlGaN materials is still very high. The excessive high dislocation density generates high noise, which will reduce the voltage withstand properties and life of devices, thus limiting the improvement of all aspects of AlGaN-based DUV detection performance.

DUV photodetectors based on  $\text{Ga}_2\text{O}_3$ , including nanostructures, single crystals, and thin films, have been widely studied and have achieved good detection performance. However, the area of a single nanomaterial is very small, and only a small part of the light shines on the nanomaterial. At the same time, the fabrication process of detectors based on nanomaterials is complex, which is not conducive to industrialization. It is still an important challenge to prepare  $\text{Ga}_2\text{O}_3$  single crystals with a large diameter and high quality. Little research exists on the formation mechanism of dislocations and other defects in single crystals. Compared with the single-crystal structure, the preparation process of  $\text{Ga}_2\text{O}_3$  thin films is more mature, and current technology can deposit large area high-quality films, but the p-type conductivity of films is still an important challenge, which limits the application of  $\text{Ga}_2\text{O}_3$  thin films in p-n junction devices.

The problem with the diamond ultraviolet detector is that the preparation technology is not yet mature, which leads to the high cost of materials. Commercially available single-crystal diamond substrates are not much larger than 8–10 mm square, far below the needs of the semiconductor industry. In addition, n-type doping remains a bottleneck problem for diamond because it limits its application in the semiconductor field. The intrinsic mechanisms of the PPC phenomenon, space charge effect, excitation effect, and carrier transport mechanism have not been clarified. There are still challenging issues in the field of diamond material synthesis and device manufacturing.

In conclusion, the prominent problems of inorganic DUV detection materials are mainly manifested in two aspects. On the one hand, the single-crystal film size of materials is small, which is not conducive to device processing and integration. On the other hand, the electrical and photoelectric properties of materials are difficult to control. Therefore, the key research fields and directions of deep ultraviolet detection materials in the future are as follows:

(1) Research on the preparation technology of high-quality large-sized film. At present, although many UV detection materials can obtain a single-crystal morphology, most of their sizes are micrometers or even nanometers, which adds difficulties to the utilization and processing of materials. Therefore, the preparation technology of detection materials is one of the key problems to be solved in the future.

(2) Research on the control process of material photoelectric performance, including material doping and surface modification technology. Doping technology can not only improve the electrical properties of the material itself but also obtain n-type and p-type materials. The doping of ultraviolet materials is a difficult problem, especially the n-type doping of h-BN and diamond, the high component Al doping of Ga-N-based materials, and the p-type doping of  $\text{Ga}_2\text{O}_3$ . In addition, new surface modification technologies need to be developed to improve the UV response of materials, such as using the plasmon effect to increase the UV detection performance of materials, and surface-plasma-enhanced UV detection performance based on different materials.

(3) Research on structural optimization technology. In addition to the material itself, the multi-level structure of the material will also have an important impact on device performance. For example, using the built-in electric field of the p-n junction itself can improve the separation efficiency of photogenerated carriers and can also be used to prepare zero-power devices. Based on the p-n junction, a band-matching material is selected as the

tunneling layer, which can also realize the tunneling mechanism and enhance the effect. Recently, some works have shown a dramatic reduction of reverse currents in nanograting Schottky junctions, which can be utilized to reduce the dark current of photodetectors.

**Author Contributions:** Methodology, Q.L.; investigation, Q.L., J.L., Y.L., Q.Z., R.C. and M.W.; writing—original draft preparation, W.F.; writing—review and editing, Q.L.; supervision, Q.L., F.Y. and T.W.; project administration, Q.L.; funding acquisition, Q.L. All authors have read and agreed to the published version of the manuscript.

**Funding:** This research was funded by [the National Key R&D Program of China] grant number [2021YFB3602000] and [the Fundamental Research Funds for the Central Universities] grant number [xyz012022088, xzd012022065].

**Data Availability Statement:** The data that support the findings of this study are available within the article.

**Conflicts of Interest:** The authors declare no conflict of interest.

## References

1. Yu, X.; Marks, T.J.; Facchetti, A. Metal oxides for optoelectronic applications. *Nat. Mater.* **2016**, *15*, 383–396. [[CrossRef](#)] [[PubMed](#)]
2. Lin, Q.; Armin, A.; Burn, P.L.; Meredith, P. Filterless narrowband visible photodetectors. *Nat. Photon* **2015**, *9*, 687–694. [[CrossRef](#)]
3. Monroy, E.; Omnès, F.; Calle, F.J. Wide-bandgap semiconductor ultraviolet photodetectors. *Semicond. Sci. Technol.* **2003**, *18*, R33–R51. [[CrossRef](#)]
4. Razeghi, M. Short-wavelength solar-blind detectors—Status, prospects, and markets. *Proc. IEEE* **2002**, *90*, 1006–1014. [[CrossRef](#)]
5. Xie, C.; Lu, X.; Tong, X.; Zhang, Z.; Liang, F.; Liang, L.; Luo, L.; Wu, Y. Recent Progress in Solar-Blind Deep-Ultraviolet Photodetectors Based on Inorganic Ultrawide Bandgap Semiconductors. *Adv. Funct. Mater.* **2019**, *29*, 1806006. [[CrossRef](#)]
6. Shang, H.; Dai, M.; Gao, F.; Yang, H.; Hu, P.; Jia, D.; Zhou, Y.; Chen, H. Progress in Inorganic Ultraviolet Photoelectric Materials. *Mater. China* **2019**, *38*, 875–886.
7. Yang, J.; Liu, K.; Chen, X.; Shen, D. Recent advances in optoelectronic and microelectronic devices based on ultrawide-bandgap semiconductors. *Prog. Quantum Electron.* **2022**, *83*, 100397. [[CrossRef](#)]
8. Izyumskaya, N.; Demchenko, D.O.; Das, S.; Özgür, Ü.; Avrutin, V.; Morkoç, H. Recent Development of Boron Nitride towards Electronic Applications. *Adv. Electron. Mater.* **2017**, *3*, 1600485. [[CrossRef](#)]
9. Feng, W.; Jin, Z.; Yuan, J.; Zhang, J.; Jia, S.; Dong, L.; Yoon, J.; Zhou, L.; Vajtai, R.; Tour, J.M.; et al. A fast and zero-biased photodetector based on GaTe-InSe vertical 2D p-n heterojunction. *2D Mater.* **2018**, *5*, 025008. [[CrossRef](#)]
10. Dai, M.; Chen, H.; Feng, R.; Feng, W.; Hu, Y.; Yang, H.; Liu, G.; Chen, X.; Zhang, J.; Xu, C.-Y.; et al. A Dual-Band Multilayer InSe Self-Powered Photodetector with High Performance Induced by Surface Plasmon Resonance and Asymmetric Schottky Junction. *ACS Nano* **2018**, *12*, 8739–8747. [[CrossRef](#)]
11. Zou, Y.; Zhang, Y.; Hu, Y.; Gu, H. Ultraviolet Detectors Based on Wide Bandgap Semiconductor Nanowire: A Review. *Sensors* **2018**, *18*, 2072. [[CrossRef](#)] [[PubMed](#)]
12. Feng, W.; Zheng, W.; Cao, W.; Hu, P. Back Gated Multilayer InSe Transistors with Enhanced Carrier Mobilities via the Suppression of Carrier Scattering from a Dielectric Interface. *Adv. Mater.* **2014**, *26*, 6587–6593. [[CrossRef](#)] [[PubMed](#)]
13. Lu, Y.-J.; Lin, C.-N.; Shan, C.-X. Optoelectronic Diamond: Growth, Properties, and Photodetection Applications. *Adv. Opt. Mater.* **2018**, *6*, 1800359. [[CrossRef](#)]
14. Liu, H.; Meng, J.; Zhang, X.; Chen, Y.; Yin, Z.; Wang, D.; Wang, Y.; You, J.; Gao, M.; Jin, P. High-performance deep ultraviolet photodetectors based on few-layer hexagonal boron nitride. *Nanoscale* **2018**, *10*, 5559–5565. [[CrossRef](#)]
15. Ma, K.Y.; Kim, M.; Shin, H.S. Large-Area Hexagonal Boron Nitride Layers by Chemical Vapor Deposition: Growth and Applications for Substrates, Encapsulation, and Membranes. *Accounts Mater. Res.* **2022**, *3*, 748–760. [[CrossRef](#)]
16. Hou, X.; Yu, Z.; Chou, K.-C. Facile synthesis of hexagonal boron nitride fibers with uniform morphology. *Ceram. Int.* **2013**, *39*, 6427–6431. [[CrossRef](#)]
17. Khan, M.H.; Huang, Z.; Xiao, F.; Casillas, G.; Chen, Z.; Molino, P.J.; Liu, H.K. Synthesis of Large and Few Atomic Layers of Hexagonal Boron Nitride on Melted Copper. *Sci. Rep.* **2015**, *5*, 7743. [[CrossRef](#)]
18. Aldalbahi, A.; Rivera, M.; Rahaman, M.; Zhou, A.F.; Alzurairi, W.M.; Feng, P. High-Performance and Self-Powered Deep UV Photodetectors Based on High Quality 2D Boron Nitride Nanosheets. *Nanomaterials* **2017**, *7*, 454. [[CrossRef](#)]
19. Sajjad, M.; Jadwisieniczak, W.M.; Feng, P. Nanoscale structure study of boron nitride nanosheets and development of a deep-UV photo-detector. *Nanoscale* **2014**, *6*, 4577–4582. [[CrossRef](#)]
20. Aldalbahi, A.; Feng, P. Development of 2-D Boron Nitride Nanosheets UV Photoconductive Detectors. *IEEE Trans. Electron Devices* **2015**, *62*, 1885–1890. [[CrossRef](#)]
21. Aldalbahi, A.; Velázquez, R.; Zhou, A.F.; Rahaman, M.; Feng, P.X. Bandgap-Tuned 2D Boron Nitride/Tungsten Nitride Nanocomposites for Development of High-Performance Deep Ultraviolet Selective Photodetectors. *Nanomaterials* **2020**, *10*, 1433. [[CrossRef](#)] [[PubMed](#)]

22. Aldalbahi, A.; Yang, R.; Li, E.Y.; Sajjad, M.; Chen, Y.; Feng, P. Low Temperature, Digital Control, Fast Synthesis of 2-D BNNSs and Their Application for Deep UV Detectors. *Mater. Res. Soc. Symp. Proc.* **2015**, *1726*, 49–55. [[CrossRef](#)]
23. Zhou, A.F.; Aldalbahi, A.; Feng, P. Vertical metal-semiconductor-metal deep UV photodetectors based on hexagonal boron nitride nanosheets prepared by laser plasma deposition. *Opt. Mater. Express* **2016**, *6*, 3286–3292. [[CrossRef](#)]
24. Rivera, M.; Velázquez, R.; Aldalbahi, A.; Zhou, A.F.; Feng, P.X. UV photodetector based on energy bandgap shifted hexagonal boron nitride nanosheets for high-temperature environments. *J. Phys. D Appl. Phys.* **2018**, *51*, 045102. [[CrossRef](#)]
25. Gao, M.; Meng, J.; Chen, Y.; Ye, S.; Wang, Y.; Ding, C.; Li, Y.; Yin, Z.; Zeng, X.; You, J.; et al. Catalyst-free growth of two-dimensional hexagonal boron nitride few-layers on sapphire for deep ultraviolet photodetectors. *J. Mater. Chem. C* **2019**, *7*, 14999–15006. [[CrossRef](#)]
26. Wang, Y.; Meng, J.; Tian, Y.; Chen, Y.; Wang, G.; Yin, Z.; Jin, P.; You, J.; Wu, J.; Zhang, X. Deep Ultraviolet Photodetectors Based on Carbon-Doped Two-Dimensional Hexagonal Boron Nitride. *ACS Appl. Mater. Interfaces* **2020**, *12*, 27361–27367. [[CrossRef](#)]
27. Li, D.; Gao, W.; Sun, X.; Yu, H.; Liu, C.; Yin, H. Direct Growth of Hexagonal Boron Nitride Thick Films on Dielectric Substrates by Ion Beam Assisted Deposition for Deep-UV Photodetectors. *Adv. Opt. Mater.* **2021**, *9*, 2100342. [[CrossRef](#)]
28. Zhang, N.; Song, Y.; Zhou, K.; Wang, W. Enhanced performance of solar-blind photodetector of hexagonal boron nitride with bottom-contact electrodes. *AIP Adv.* **2020**, *10*, 085013. [[CrossRef](#)]
29. Zheng, W.; Lin, R.; Zhang, Z.; Huang, F. Vacuum-Ultraviolet Photodetection in Few-Layered h-BN. *ACS Appl. Mater. Interfaces* **2018**, *10*, 27116–27123. [[CrossRef](#)]
30. Chen, X.; Tan, C.; Liu, X.; Luan, K.; Guan, Y.; Liu, X.; Zhao, J.; Hou, L.; Gao, Y.; Chen, Z. Growth of hexagonal boron nitride films on silicon substrates by low-pressure chemical vapor deposition. *J. Mater. Sci. Mater. Electron.* **2021**, *32*, 3713–3719. [[CrossRef](#)]
31. Feng, Y.; Zhang, Y.; Liu, J.; Zhang, Y.; Xie, Y. Large-Scale Synthesis h-BN Films on Copper-Nickel Alloy by Atmospheric Pressure Chemical Vapor Deposition. *Crystals* **2022**, *12*, 985. [[CrossRef](#)]
32. Tan, B.; Yang, H.; Hu, Y.; Gao, F.; Wang, L.; Dai, M.; Zhang, S.; Shang, H.; Chen, H.; Hu, P. Synthesis of High-Quality Multilayer Hexagonal Boron Nitride Films on Au Foils for Ultrahigh Rejection Ratio Solar-Blind Photodetection. *ACS Appl. Mater. Interfaces* **2020**, *12*, 28351–28359. [[CrossRef](#)] [[PubMed](#)]
33. Yang, H.; Wang, L.; Gao, F.; Dai, M.; Hu, Y.; Chen, H.; Zhang, J.; Qiu, Y.; Jia, D.C.; Zhou, Y.; et al. Shape evolution of two dimensional hexagonal boron nitride single domains on Cu/Ni alloy and its applications in ultraviolet detection. *Nanotechnology* **2019**, *30*, 245706. [[CrossRef](#)]
34. Li, J.; Majety, S.; Dahal, R.; Zhao, W.P.; Lin, J.Y.; Jiang, H.X. Dielectric strength, optical absorption, and deep ultraviolet detectors of hexagonal boron nitride epilayers. *Appl. Phys. Lett.* **2012**, *101*, 171112. [[CrossRef](#)]
35. Li, X.; Jordan, M.B.; Ayari, T.; Sundaram, S.; El Gmili, Y.; Alam, S.; Alam, M.; Patriarche, G.; Voss, P.L.; Salvestrini, J.P.; et al. Flexible metal-semiconductor-metal device prototype on wafer-scale thick boron nitride layers grown by MOVPE. *Sci. Rep.* **2017**, *7*, 786. [[CrossRef](#)]
36. Prakash, A.; Nehate, S.D.; Sundaram, K.B. Boron carbon nitride based metal-insulator-metal UV detectors for harsh environment applications. *Opt. Lett.* **2016**, *41*, 4249–4252. [[CrossRef](#)] [[PubMed](#)]
37. Jang, A.-R.; Hong, S.; Hyun, C.; Yoon, S.I.; Kim, G.; Jeong, H.Y.; Shin, T.J.; Park, S.O.; Wong, K.W.; Kwak, S.K.; et al. Wafer-Scale and Wrinkle-Free Epitaxial Growth of Single-Orientated Multilayer Hexagonal Boron Nitride on Sapphire. *Nano Lett.* **2016**, *16*, 3360–3366. [[CrossRef](#)]
38. Veeralingam, S.; Durai, L.; Yadav, P.; Badhulika, S. Record-High Responsivity and Detectivity of a Flexible Deep-Ultraviolet Photodetector Based on Solid State-Assisted Synthesized hBN Nanosheets. *ACS Appl. Electron. Mater.* **2021**, *3*, 1162–1169. [[CrossRef](#)]
39. Garimella, S.V.; Fleischer, A.S.; Murthy, J.Y.; Keshavarzi, A.; Prasher, R.; Patel, C.; Bhavnani, S.H.; Venkatasubramanian, R.; Mahajan, R.; Joshi, Y.; et al. Thermal Challenges in Next-Generation Electronic Systems. *IEEE Trans. Compon. Packag. Technol.* **2008**, *31*, 801–815. [[CrossRef](#)]
40. Lin, C.-H.; Fu, H.-C.; Cheng, B.; Tsai, M.-L.; Luo, W.; Zhou, L.; Jang, S.-H.; Hu, L.; He, J.-H. A flexible solar-blind 2D boron nitride nanopaper-based photodetector with high thermal resistance. *Npj 2D Mater. Appl.* **2018**, *2*, 23. [[CrossRef](#)]
41. Zhang, W.; Bello, I.; Lifshitz, Y.; Lee, S.T. Recent Advances in Cubic Boron Nitride Deposition. *MRS Bull.* **2003**, *28*, 184–188. [[CrossRef](#)]
42. Zhang, W.J.; Chong, Y.M.; Bello, I.; Lee, S.T. Nucleation, growth and characterization of cubic boron nitride (cBN) films. *J. Phys. D Appl. Phys.* **2007**, *40*, 6159–6174. [[CrossRef](#)]
43. Soltani, A.; Barkad, H.A.; Mattalah, M.; Benbakhti, B.; De Jaeger, J.-C.; Chong, Y.M.; Zou, Y.S.; Zhang, W.J.; Lee, S.T.; BenMoussa, A.; et al. 193nm deep-ultraviolet solar-blind cubic boron nitride based photodetectors. *Appl. Phys. Lett.* **2008**, *92*, 053501. [[CrossRef](#)]
44. Mballo, A.; Srivastava, A.; Sundaram, S.; Vuong, P.; Karrakchou, S.; Halfaya, Y.; Gautier, S.; Voss, P.L.; Ahaitouf, A.; Salvestrini, J.P.; et al. Towards P-Type Conduction in Hexagonal Boron Nitride: Doping Study and Electrical Measurements Analysis of hBN/AlGaN Heterojunctions. *Nanomaterials* **2021**, *11*, 211. [[CrossRef](#)]
45. Briegleb, F.; Geuther, A. Ueber das Stickstoffmagnesium und die Affinitäten des Stickgases zu Metallen. *Eur. J. Org. Chem.* **1862**, *123*, 228–241. [[CrossRef](#)]
46. Taylor, K.M.; Lenie, C. Some Properties of Aluminum Nitride. *J. Electrochem. Soc.* **1960**, *107*, 308. [[CrossRef](#)]

47. Cox, G.; Cummins, D.; Kawabe, K.; Tredgold, R. On the preparation, optical properties and electrical behaviour of aluminium nitride. *J. Phys. Chem. Solids* **1967**, *28*, 543–548. [[CrossRef](#)]
48. Alaie, Z.; Nejad, S.M.; Yousefi, M. Recent advances in ultraviolet photodetectors. *Mater. Sci. Semicond. Process.* **2015**, *29*, 16–55. [[CrossRef](#)]
49. Liu, F.; Li, L.; Guo, T.; Gan, H.; Mo, X.; Chen, J.; Deng, S.; Xu, N. Investigation on the photoconductive behaviors of an individual AlN nanowire under different excited lights. *Nanoscale Res. Lett.* **2012**, *7*, 454. [[CrossRef](#)]
50. Kenry; Yong, K.T.; Yu, S.F. AlN nanowires: Synthesis, physical properties, and nanoelectronics applications. *J. Mater. Sci.* **2012**, *47*, 5341–5360. [[CrossRef](#)]
51. Teker, K. Dielectrophoretic Assembly of Aluminum Nitride (AlN) Single Nanowire Deep Ultraviolet Photodetector. *J. Nano Res.* **2019**, *60*, 86–93. [[CrossRef](#)]
52. Zheng, W.; Huang, F.; Zheng, R.; Wu, H. Low-Dimensional Structure Vacuum-Ultraviolet-Sensitive ( $\lambda < 200$  nm) Photodetector with Fast-Response Speed Based on High-Quality AlN Micro/Nanowire. *Adv. Mater.* **2015**, *27*, 3921–3927.
53. Ali, Y.A.; Teker, K. Fabrication of ultraviolet photodetector with aluminum nitride nanowire networks via direct transfer method. *Microelectron. Eng.* **2019**, *211*, 26–28. [[CrossRef](#)]
54. Ozdemir, Y.B.; Teker, K.; Yildirim, M.A. High-responsivity flexible ultraviolet photodetector via single aluminum nitride nanowire. *Opt. Eng.* **2021**, *60*, 057104. [[CrossRef](#)]
55. Hartmann, C.; Wollweber, J.; Dittmar, A.; Irmscher, K.; Kwasniewski, A.; Langhans, F.; Neugut, T.; Bickermann, M. Preparation of Bulk AlN Seeds by Spontaneous Nucleation of Freestanding Crystals. *Jpn. J. Appl. Phys.* **2013**, *52*, 08JA06. [[CrossRef](#)]
56. Wang, Q.; Lei, D.; He, G.; Gong, J.; Huang, J.; Wu, J. Characterization of 60 mm AlN Single Crystal Wafers Grown by the Physical Vapor Transport Method. *Phys. Status Solidi* **2019**, *216*, 1900118. [[CrossRef](#)]
57. Hu, W.; Guo, L.; Guo, Y.; Wang, W. Growing AlN crystals on SiC seeds: Effects of growth temperature and seed orientation. *J. Cryst. Growth* **2020**, *541*, 125654. [[CrossRef](#)]
58. Knauer, A.; Mogilatenko, A.; Hagedorn, S.; Enslin, J.; Wernicke, T.; Kneissl, M.; Weyers, M. Correlation of sapphire off-cut and reduction of defect density in MOVPE grown AlN. *Phys. Status Solidi* **2016**, *253*, 809–813. [[CrossRef](#)]
59. Claudel, A.; Blanquet, E.; Chaussende, D.; Audier, M.; Pique, D.; Pons, M. Thermodynamic and experimental investigations on the growth of thick aluminum nitride layers by high temperature CVD. *J. Cryst. Growth* **2009**, *311*, 3371–3379. [[CrossRef](#)]
60. Kumagai, Y.; Kubota, Y.; Nagashima, T.; Kinoshita, T.; Dalmau, R.; Schlessner, R.; Moody, B.; Xie, J.; Murakami, H.; Koukitsu, A.; et al. Preparation of a Freestanding AlN Substrate from a Thick AlN Layer Grown by Hydride Vapor Phase Epitaxy on a Bulk AlN Substrate Prepared by Physical Vapor Transport. *Appl. Phys. Express* **2012**, *5*, 055504. [[CrossRef](#)]
61. Mansurov, V.; Nikitin, A.; Galitsyn, Y.; Svitashcheva, S.; Zhuravlev, K.; Osvath, Z.; Dobos, L.; Horvath, Z.; Pecz, B. AlN growth on sapphire substrate by ammonia MBE. *J. Cryst. Growth* **2007**, *300*, 145–150. [[CrossRef](#)]
62. Shukla, G.; Khare, A. Dependence of N<sub>2</sub> pressure on the crystal structure and surface quality of AlN thin films deposited via pulsed laser deposition technique at room temperature. *Appl. Surf. Sci.* **2008**, *255*, 2057–2062. [[CrossRef](#)]
63. Szekeres, A.; Fogarassy, Z.; Petrik, P.; Vlaikova, E.; Cziraki, A.; Socol, G.; Ristoscu, C.; Grigorescu, S.; Mihailescu, I. Structural characterization of AlN films synthesized by pulsed laser deposition. *Appl. Surf. Sci.* **2011**, *257*, 5370–5374. [[CrossRef](#)]
64. Li, T.; Han, J.; Xing, Y.; Deng, X.; Li, J.; Zhang, L.; Shi, F.; Yu, L.; Sun, C.; Zhang, X.; et al. Influence of pressure on the properties of AlN deposited by DC reactive magnetron sputtering on Si (100) substrate. *Micro Nano Lett.* **2019**, *14*, 146–149. [[CrossRef](#)]
65. Xiao, S.; Suzuki, R.; Miyake, H.; Harada, S.; Ujihara, T. Improvement mechanism of sputtered AlN films by high-temperature annealing. *J. Cryst. Growth* **2018**, *502*, 41–44. [[CrossRef](#)]
66. Chen, M.-R.; Chen, H.-G.; Kao, H.-L.; Wu, M.-G.; Tzou, A.-J.; Chen, J.S.; Chou, H. Structural and optical properties of low temperature grown AlN films on sapphire using helicon sputtering system. *J. Vac. Sci. Technol. A* **2015**, *33*, 031503. [[CrossRef](#)]
67. Murtaza, S.H.; Ahmed, S.; Ali, M. Investigation of AlN/Si based heterogeneous Junction using inter-digitated electrodes for enhanced UV light detection. *Optik* **2022**, *265*, 169534. [[CrossRef](#)]
68. Yang, R.Y.; Hsiung, C.M.; Chen, H.H.; Wu, H.W.; Shih, M.C. Effect of AlN film thickness on photo/dark currents of MSM UV photodetector. *Microw. Opt. Technol. Lett.* **2008**, *50*, 2863–2866. [[CrossRef](#)]
69. Li, T.; Song, W.; Zhang, L.; Yan, J.; Zhu, W.; Wang, L. Self-powered asymmetric metal–semiconductor–metal AlN deep ultraviolet detector. *Opt. Lett.* **2022**, *47*, 637–640. [[CrossRef](#)]
70. Li, T.; Long, L.; Hu, Z.; Wan, R.; Gong, X.; Zhang, L.; Yuan, Y.; Yan, J.; Zhu, W.; Wang, L.; et al. Three-dimensional metal–semiconductor–metal AlN deep-ultraviolet detector. *Opt. Lett.* **2020**, *45*, 3325–3328. [[CrossRef](#)]
71. Kaushik, S.; Naik, T.R.; Alka, A.; Garg, M.; Tak, B.R.; Ravikanth, M.; Rao, V.R.; Singh, R. Surface Modification of AlN Using Organic Molecular Layer for Improved Deep UV Photodetector Performance. *ACS Appl. Electron. Mater.* **2020**, *2*, 739–746. [[CrossRef](#)]
72. Eller, B.S.; Yang, J.; Nemanich, R.J. Electronic surface and dielectric interface states on GaN and AlGaN. *J. Vac. Sci. Technol. A* **2013**, *31*, 050807. [[CrossRef](#)]
73. Averin, S.V.; Kuznetsov, P.I.; Zhitov, V.A.; Alkeev, N.V.; Kotov, V.M.; Dorofeev, A.A.; Gladysheva, N.B. AlN/AlGaN heterostructures for selective ultraviolet MSM detectors. *Tech. Phys.* **2011**, *56*, 295–297. [[CrossRef](#)]
74. Lu, J.; Lv, Z.; Qiu, X.; Lai, S.; Jiang, H. Ultrasensitive and high-speed AlGaN/AlN solar-blind ultraviolet photodetector: A full-channel-self-depleted phototransistor by a virtual photogate. *Photon Res.* **2022**, *10*, 2229. [[CrossRef](#)]

75. Hao, Y.; Wang, X.; An, Y. A Ga<sub>2</sub>O<sub>3</sub>/AlN heterojunction for self-powered solar-blind photodetection with high photo-to-dark current ratio and fast response speed. *Phys. Scr.* **2021**, *96*, 125835. [[CrossRef](#)]
76. Li, T.; Lu, Y.; Chen, Z. Heteroepitaxy Growth and Characterization of High-Quality AlN Films for Far-Ultraviolet Photodetection. *Nanomaterials* **2022**, *12*, 4169. [[CrossRef](#)]
77. Cai, Q.; You, H.; Guo, H.; Wang, J.; Liu, B.; Xie, Z.; Chen, D.; Lu, H.; Zheng, Y.; Zhang, R. Progress on AlGaIn-based solar-blind ultraviolet photodetectors and focal plane arrays. *Light Sci. Appl.* **2021**, *10*, 94. [[CrossRef](#)]
78. Li, D.B.; Jiang, K.; Sun, X.J.; Guo, C.L. AlGaIn photonics: Recent advances in materials and ultraviolet devices. *Adv. Opt. Photonics* **2018**, *10*, 43–110. [[CrossRef](#)]
79. Su, L.; Yang, W.; Cai, J.; Chen, H.; Fang, X. Self-Powered Ultraviolet Photodetectors Driven by Built-In Electric Field. *Small* **2017**, *13*, 1701687. [[CrossRef](#)] [[PubMed](#)]
80. Tian, W.; Wang, Y.; Chen, L.; Li, L. Self-Powered Nanoscale Photodetectors. *Small* **2017**, *13*, 1701848. [[CrossRef](#)]
81. Wang, D.; Huang, C.; Liu, X.; Zhang, H.; Yu, H.; Fang, S.; Ooi, B.S.; Mi, Z.; He, J.H.; Sun, H. Highly Uniform, Self-Assembled AlGaIn Nanowires for Self-Powered Solar-Blind Photodetector with Fast-Response Speed and High Responsivity. *Adv. Opt. Mater.* **2021**, *9*, 2000893. [[CrossRef](#)]
82. Kang, S.; Chatterjee, U.; Um, D.Y.; Yu, Y.T.; Seo, I.S.; Lee, C.R. Ultraviolet-C Photodetector Fabricated Using Si-Doped n-AlGaIn Nanorods Grown by MOCVD. *ACS Photonics* **2017**, *4*, 2595–2603. [[CrossRef](#)]
83. Ouyang, W.; Teng, F.; He, J.; Fang, X. Enhancing the Photoelectric Performance of Photodetectors Based on Metal Oxide Semiconductors by Charge-Carrier Engineering. *Adv. Funct. Mater.* **2019**, *29*, 1807672. [[CrossRef](#)]
84. Lu, N.; Gu, Y.; Weng, Y.; Dai, Z.; Ding, Y. Localized surface plasmon enhanced photoresponse of AlGaIn MSM solar-blind ultraviolet photodetectors. *Mater. Res. Express* **2019**, *6*, 095033. [[CrossRef](#)]
85. Jia, C.; Li, X.; Xin, N.; Gong, Y.; Guan, J.; Meng, L.; Meng, S.; Guo, X. Interface-Engineered Plasmonics in Metal/Semiconductor Heterostructures. *Adv. Energy Mater.* **2016**, *6*, 1600431. [[CrossRef](#)]
86. Wu, Y.; Sun, X.; Shi, Z.; Jia, Y.; Jiang, K.; Ben, J.; Kai, C.; Wang, Y.; Lü, W.; Li, D. In situ fabrication of Al surface plasmon nanoparticles by metal-organic chemical vapor deposition for enhanced performance of AlGaIn deep ultraviolet detectors. *Nanoscale Adv.* **2020**, *2*, 1854–1858. [[CrossRef](#)]
87. Rathkantiwar, S.; Kalra, A.; Muralidharan, R.; Nath, D.N.; Raghavan, S. V-Pits-Induced Photoresponse Enhancement in AlGaIn UV-B Photodetectors on Si (111). *IEEE Trans. Electron Devices* **2020**, *67*, 4281–4287. [[CrossRef](#)]
88. Zhao, Y.; Donaldson, W.R. Ultrafast UV AlGaIn Metal–Semiconductor–Metal Photodetector With a Response Time Below 25 ps. *IEEE J. Quantum Electron.* **2020**, *56*, 1–7. [[CrossRef](#)]
89. Chen, Y.; Zang, H.; Ben, J.; Zhang, S.; Jiang, K.; Shi, Z.; Jia, Y.; Liu, M.; Sun, X.; Li, D. AlGaIn UV Detector with Largely Enhanced Heat Dissipation on Mo Substrate Enabled by van der Waals Epitaxy. *Cryst. Growth Des.* **2023**, *23*, 1162–1171. [[CrossRef](#)]
90. Kalra, A.; Rathkantiwar, S.; Muralidharan, R.; Raghavan, S.; Nath, D.N. Polarization-Graded AlGaIn Solar-Blind p-i-n Detector With 92% Zero-Bias External Quantum Efficiency. *IEEE Photonics Technol. Lett.* **2019**, *31*, 1237–1240. [[CrossRef](#)]
91. Kalra, A.; Rathkantiwar, S.; Muralidharan, R.; Raghavan, S.; Nath, D.N. Material-to-device performance correlation for AlGaIn-based solar-blind p-i-n photodiodes. *Semicond. Sci. Technol.* **2020**, *35*, 035001. [[CrossRef](#)]
92. Kurose, N.; Iwata, N.; Kamiya, I.; Aoyagi, Y. Formation of conductive spontaneous via holes in AlN buffer layer on n(+)/Si substrate by filling the vias with n-AlGaIn by metal organic chemical vapor deposition and application to vertical deep ultraviolet photo-sensor. *AIP Adv.* **2014**, *4*, 123007. [[CrossRef](#)]
93. Gautam, L.; Lee, J.; Brown, G.; Razeghi, M. Low Dark Current Deep UV AlGaIn Photodetectors on AlN Substrate. *IEEE J. Quantum Electron.* **2022**, *58*, 1–5. [[CrossRef](#)]
94. Zhou, M.; Qiu, H.; He, T.; Zhang, J.; Yang, W.; Lu, S.; Bian, L.; Zhao, Y. UV Photodetector Based on Vertical (Al, Ga)N Nanowires with Graphene Electrode and Si Substrate. *Phys. Status Solidi* **2020**, *217*, 2000061. [[CrossRef](#)]
95. Rodak, L.E.; Sampath, A.V.; Gallinat, C.S.; Enck, R.W.; Smith, J.; Shen, H.; Wraback, M.; Chen, Y.; Zhou, Q.; Campbell, J.C. Aluminum gallium nitride/silicon carbide separate absorption and multiplication avalanche photodiodes. In Proceedings of the 2012 Lester Eastman Conference on High Performance Devices, Providence, RI, USA, 7–9 August 2012.
96. Sood, A.K.; Zeller, J.W.; Ghuman, P.; Babu, S.; Dupuis, R.D. GaN/AlGaIn avalanche photodiode detector technology for high performance ultraviolet sensing applications. In Proceedings of the SPIE—The International Society for Optical Engineering, Online, 24 August–4 September 2020.
97. Nguyen, H.Q.; Faisal, A.R.; Nguyen, T.; Nguyen, H.; Vu, T.H.; Fastier-Wooler, J.; Aberoumand, S.; Phan, H.P.; Dao, D.V. Rapid Fabrication of High-responsivity Photodetectors Utilizing AlGaIn/GaN on Sapphire. In Proceedings of the IEEE Sensors, Sydney, Australia, 31 October–3 November 2021.
98. Gao, J.; Li, Y.; Hu, Y.; Wang, Z.; Hu, A.; Guo, X. A 2DEG back-gated graphene/AlGaIn deep-ultraviolet photodetector with ultrahigh responsivity. *Chin. Phys. B* **2020**, *29*, 128502. [[CrossRef](#)]
99. Sun, J.; Zhan, T.; Liu, Z.; Wang, J.; Yi, X.; Sarro, P.M.; Zhang, G. Suspended tungsten trioxide (WO<sub>3</sub>) gate AlGaIn/GaN heterostructure deep ultraviolet detectors with integrated micro-heater. *Opt. Express* **2019**, *27*, 36405–36413. [[CrossRef](#)]
100. Sun, J.; Zhang, S.; Zhan, T.; Liu, Z.; Wang, J.; Yi, X.; Li, J.; Sarro, P.M.; Zhang, G. A high responsivity and controllable recovery ultraviolet detector based on a WO<sub>3</sub> gate AlGaIn/GaN heterostructure with an integrated micro-heater. *J. Mater. Chem. C* **2020**, *8*, 5409–5416. [[CrossRef](#)]

101. Cicek, E.; McClintock, R.; Cho, C.Y.; Rahnema, B.; Razeghi, M. Al<sub>x</sub>Ga<sub>1-x</sub>N-based back-illuminated solar-blind photodetectors with external quantum efficiency of 89%. *Appl. Phys. Lett.* **2013**, *103*, 191108. [[CrossRef](#)]
102. Higashiwaki, M.; Sasaki, K.; Kuramata, A.; Masui, T.; Yamakoshi, S. Gallium oxide (Ga<sub>2</sub>O<sub>3</sub>) metal-semiconductor field-effect transistors on single-crystal β-Ga<sub>2</sub>O<sub>3</sub> (010) substrates. *Appl. Phys. Lett.* **2012**, *100*, 013504. [[CrossRef](#)]
103. El-Sayed, E.I.; Al-Ghamdi, A.A.; Al-Heniti, S.; Al-Marzouki, F.; El-Tantawy, F. Synthesis of ultrafine β-Ga<sub>2</sub>O<sub>3</sub> nanopowder via hydrothermal approach: A strong UV “excimer-like” emission. *Mater. Lett.* **2011**, *65*, 317–321. [[CrossRef](#)]
104. Ruan, M.M.; Yang, Z.; Teng, Y.; Wang, Q.S.; Wang, Y.Q. Novel green synthesis and improved solar-blind detection performance of hierarchical γ-Ga<sub>2</sub>O<sub>3</sub> nanospheres. *J. Mater. Chem. C* **2017**, *5*, 7161–7166. [[CrossRef](#)]
105. Rafique, S.; Karim, M.R.; Johnson, J.M.; Hwang, J.; Zhao, H. LPCVD homoepitaxy of Si doped β-Ga<sub>2</sub>O<sub>3</sub> thin films on (010) and (001) substrates. *Appl. Phys. Lett.* **2018**, *112*, 052104. [[CrossRef](#)]
106. Weng, W.Y.; Hsueh, T.J.; Chang, S.J.; Huang, G.J.; Chang, S.P. A Solar-Blind β-Ga<sub>2</sub>O<sub>3</sub> Nanowire Photodetector. *IEEE Photonics Technol. Lett.* **2010**, *22*, 709–711. [[CrossRef](#)]
107. Wu, Y.L.; Chang, S.J.; Weng, W.Y.; Liu, C.H.; Tsai, T.Y.; Hsu, C.L.; Chen, K.C. Ga<sub>2</sub>O<sub>3</sub> Nanowire Photodetector Prepared on SiO<sub>2</sub>/Si Template. *IEEE Sens. J.* **2013**, *13*, 2368–2373. [[CrossRef](#)]
108. Chen, X.; Liu, K.; Zhang, Z.; Wang, C.; Li, B.; Zhao, H.; Zhao, D.; Shen, D. Self-Powered Solar-Blind Photodetector with Fast Response Based on Au/β-Ga<sub>2</sub>O<sub>3</sub> Nanowires Array Film Schottky Junction. *ACS Appl. Mater. Interfaces* **2016**, *8*, 4185–4191. [[CrossRef](#)] [[PubMed](#)]
109. Du, J.; Xing, J.; Ge, C.; Liu, H.; Liu, P.; Hao, H.; Dong, J.; Zheng, Z.; Gao, H. Highly sensitive and ultrafast deep UV photodetector based on a beta-Ga<sub>2</sub>O<sub>3</sub> nanowire network grown by CVD. *J. Phys. D-Appl. Phys.* **2016**, *49*, 425105. [[CrossRef](#)]
110. Li, L.; Auer, E.; Liao, M.; Fang, X.; Zhai, T.; Gautam, U.K.; Lugstein, A.; Koide, Y.; Bando, Y.; Golberg, D. Deep-ultraviolet solar-blind photoconductivity of individual gallium oxide nanobelts. *Nanoscale* **2011**, *3*, 1120–1126. [[CrossRef](#)]
111. Zhong, M.; Wei, Z.; Meng, X.; Wu, F.; Li, J. High-performance single crystalline UV photodetectors of β-Ga<sub>2</sub>O<sub>3</sub>. *J. Alloys Compd.* **2015**, *619*, 572–575. [[CrossRef](#)]
112. Teng, Y.; Song, L.X.; Ponchel, A.; Yang, Z.K.; Xia, J. Self-Assembled Metastable γ-Ga<sub>2</sub>O<sub>3</sub> Nanoflowers with Hexagonal Nanopetals for Solar-Blind Photodetection. *Adv. Mater.* **2014**, *26*, 6238–6243. [[CrossRef](#)]
113. Feng, W.; Wang, X.; Zhang, J.; Wang, L.; Zheng, W.; Hu, P.; Cao, W.; Yang, B. Synthesis of two-dimensional β-Ga<sub>2</sub>O<sub>3</sub> nanosheets for high-performance solar blind photodetectors. *J. Mater. Chem. C* **2014**, *2*, 3254–3259. [[CrossRef](#)]
114. Oh, S.; Kim, J.; Ren, F.; Pearton, S.J.; Kim, J. Quasi-two-dimensional b-gallium oxide solar-blind photodetectors with ultrahigh responsivity. *J. Mater. Chem. C* **2016**, *4*, 9245–9250. [[CrossRef](#)]
115. Oh, S.; Mastro, M.A.; Tadjer, M.J.; Kim, J. Solar-Blind Metal-Semiconductor-Metal Photodetectors Based on an Exfoliated β-Ga<sub>2</sub>O<sub>3</sub> Micro-Flake. *ECS J. Solid State Sci. Technol.* **2017**, *6*, Q79. [[CrossRef](#)]
116. Kwon, Y.; Lee, G.; Oh, S.; Kim, J.; Pearton, S.J.; Ren, F. Tuning the thickness of exfoliated quasi-two-dimensional β-Ga<sub>2</sub>O<sub>3</sub> flakes by plasma etching. *Appl. Phys. Lett.* **2017**, *110*, 131901. [[CrossRef](#)]
117. Xu, Y.; Chen, X.; Zhou, D.; Ren, F.; Zhou, J.; Bai, S.; Lu, H.; Gu, S.; Zhang, R.; Zheng, Y.; et al. Carrier Transport and Gain Mechanisms in β-Ga<sub>2</sub>O<sub>3</sub>-Based Metal-Semiconductor-Metal Solar-Blind Schottky Photodetectors. *IEEE Trans. Electron. Devices* **2019**, *66*, 2276–2281. [[CrossRef](#)]
118. Tak, B.R.; Garg, M.; Dewan, S.; Torres-Castaneda, C.G.; Li, K.H.; Gupta, V.; Li, X.; Singh, R. High-temperature photocurrent mechanism of β-Ga<sub>2</sub>O<sub>3</sub> based metal-semiconductor-metal solar-blind photodetectors. *J. Appl. Phys.* **2019**, *125*, 144501. [[CrossRef](#)]
119. Tak, B.R.; Yang, M.M.; Alexe, M.; Singh, R. Deep-Level Traps Responsible for Persistent Photocurrent in Pulsed-Laser-Deposited β-Ga<sub>2</sub>O<sub>3</sub> Thin Films. *Crystals* **2021**, *11*, 1046. [[CrossRef](#)]
120. Tak, B.R.; Alexe, M.; Singh, R. Investigation of Deep Level Traps Responsible for Persistent Photocurrent in Pulsed Laser Deposited β-Ga<sub>2</sub>O<sub>3</sub> Thin Films. In Proceedings of the 2020 5th IEEE International Conference on Emerging Electronics, Jaipur, India, 1–3 December 2020.
121. Chu, S.-Y.; Shen, M.-X.; Yeh, T.-H.; Chen, C.-H.; Lee, C.-T.; Lee, H.-Y. Investigation of Ga<sub>2</sub>O<sub>3</sub>-Based Deep Ultraviolet Photodetectors Using Plasma-Enhanced Atomic Layer Deposition System. *Sensors* **2020**, *20*, 6159. [[CrossRef](#)]
122. Li, H.; Chen, P.-W.; Yuan, S.-H.; Huang, T.-M.; Zhang, S.; Wu, D.-S. Improved Performance of Deep Ultraviolet Photodetector From Sputtered Ga<sub>2</sub>O<sub>3</sub> Films Using Post-Thermal Treatments. *IEEE Photonics J.* **2019**, *11*, 1–8. [[CrossRef](#)]
123. Zhou, H.; Cong, L.; Ma, J.; Li, B.; Chen, M.; Xu, H.; Liu, Y. High gain broadband photoconductor based on amorphous Ga<sub>2</sub>O<sub>3</sub> and suppression of persistent photoconductivity. *J. Mater. Chem. C* **2019**, *7*, 13149–13155. [[CrossRef](#)]
124. Zhang, T.; Guan, D.; Liu, N.; Zhang, J.; Zhang, J.; Guo, C.; Qiu, M.; Yuan, Q.; Zhang, W.; Ye, J. Room temperature fabrication and post-annealing treatment of amorphous Ga<sub>2</sub>O<sub>3</sub> photodetectors for deep-ultraviolet light detection. *Appl. Phys. Express* **2022**, *15*, 022007. [[CrossRef](#)]
125. Yuan, S.-H.; Wang, C.-C.; Huang, S.-Y.; Wu, D.-S. Improved Responsivity Drop From 250 to 200 nm in Sputtered Gallium Oxide Photodetectors by Incorporating Trace Aluminum. *IEEE Electron Device Lett.* **2018**, *39*, 220–223. [[CrossRef](#)]
126. Lee, H.Y.; Liu, J.T.; Lee, C.T. Modulated Al<sub>2</sub>O<sub>3</sub>-Alloyed Ga<sub>2</sub>O<sub>3</sub> Materials and Deep Ultraviolet Photodetectors. *IEEE Photonics Technol. Lett.* **2018**, *30*, 549–552. [[CrossRef](#)]
127. Chen, P.-W.; Huang, S.-Y.; Wang, C.-C.; Yuan, S.-H.; Wu, D.-S. Influence of oxygen on sputtering of aluminum-gallium oxide films for deep-ultraviolet detector applications. *J. Alloys Compd.* **2019**, *791*, 1213–1219. [[CrossRef](#)]

128. Guo, J.; Ma, M.; Li, Y.; Zhang, D.; Liu, Y.; Zheng, W. Bandgap Engineering of ZrGaO Films for Deep-Ultraviolet Detection. *IEEE Electron Device Lett.* **2021**, *42*, 895–898. [[CrossRef](#)]
129. Li, Y.; Li, Y.; Ji, Y.; Wang, H.; Zhong, D. Sol-gel preparation of Sn doped gallium oxide films for application in solar-blind ultraviolet photodetectors. *J. Mater. Sci.* **2022**, *57*, 1186–1197. [[CrossRef](#)]
130. Mukhopadhyay, P.; Schoenfeld, W.V. High responsivity tin gallium oxide Schottky ultraviolet photodetectors. *J. Vac. Sci. Technol. A* **2020**, *38*, 013403. [[CrossRef](#)]
131. Xiao, X.; Liang, L.; Pei, Y.; Yu, J.; Duan, H.; Chang, T.C.; Cao, H. Solution-processed amorphous Ga<sub>2</sub>O<sub>3</sub>: CdO TFT-type deep-UV photodetectors. *Appl. Phys. Lett.* **2020**, *116*, 192102. [[CrossRef](#)]
132. Yu, J.; Javaid, K.; Liang, L.; Wu, W.; Liang, Y.; Song, A.; Zhang, H.; Shi, W.; Chang, T.-C.; Cao, H. High-Performance Visible-Blind Ultraviolet Photodetector Based on IGZO TFT Coupled with p–n Heterojunction. *ACS Appl. Mater. Interfaces* **2018**, *10*, 8102–8109. [[CrossRef](#)]
133. Pintor-Monroy, M.I.; Reyes-Banda, M.G.; Avila-Avendano, C.; Quevedo-Lopez, M.A. Tuning Electrical Properties of Amorphous Ga<sub>2</sub>O<sub>3</sub> Thin Films for Deep UV Phototransistors. *IEEE Sens. J.* **2021**, *21*, 14807–14814. [[CrossRef](#)]
134. Li, X.X.; Zeng, G.; Li, Y.C.; Yu, Q.J.; Liu, M.Y.; Zhu, L.Y.; Liu, W.; Yang, Y.G.; Zhang, D.W.; Lu, H.L. Highly sensitive and stable β-Ga<sub>2</sub>O<sub>3</sub> DUV phototransistor with local back-gate structure and its neuromorphic application. *Nano Res.* **2022**, *15*, 9359–9367. [[CrossRef](#)]
135. Vieira, D.H.; Badiei, N.; Evans, J.E.; Alves, N.; Kettle, J.; Li, L. Improvement of the Deep UV Sensor Performance of a β-Ga<sub>2</sub>O<sub>3</sub> Photodiode by Coupling of Two Planar Diodes. *IEEE Trans. Electron. Devices* **2020**, *67*, 4947–4952. [[CrossRef](#)]
136. Mondal, A.; Nandi, S.; Yadav, M.K.; Nandi, A.; Bag, A. Broad Range (254–302 nm) and High Performance Ga<sub>2</sub>O<sub>3</sub>: SnO<sub>2</sub> Based Deep UV Photodetector. *IEEE Trans. Nanotechnol.* **2022**, *21*, 320–327. [[CrossRef](#)]
137. Zhao, B.; Wang, F.; Chen, H.; Wang, Y.; Jiang, M.; Fang, X.; Zhao, D. Solar-Blind Avalanche Photodetector Based On Single ZnO–Ga<sub>2</sub>O<sub>3</sub> Core–Shell Microwire. *Nano Lett.* **2015**, *15*, 3988–3993. [[CrossRef](#)]
138. Kong, W.Y.; Wu, G.A.; Wang, K.Y.; Zhang, T.F.; Zou, Y.F.; Wang, D.D.; Luo, L.B. Graphene-β-Ga<sub>2</sub>O<sub>3</sub> Heterojunction for Highly Sensitive Deep UV Photodetector Application. *Adv. Mater.* **2016**, *28*, 10725–10731. [[CrossRef](#)] [[PubMed](#)]
139. Wang, Y.; Fu, R.; Wang, Y.; Li, B.; Xu, H.; Shen, A.; Liu, Y. A High Responsivity Self-Powered Solar-Blind DUV Photodetector Based on a Nitrogen-Doped Graphene/β-Ga<sub>2</sub>O<sub>3</sub> Microwire p–n Heterojunction. *IEEE Electron Device Lett.* **2022**, *43*, 1073–1076. [[CrossRef](#)]
140. Kumar, A.; Nandi, A.; Bag, A. Exceptional Responsivity (>6 kA/W) and Dark Current (<70 fA) Tradeoff of n-Ga<sub>2</sub>O<sub>3</sub>/p-CuO Quasi-Heterojunction-Based Deep UV Photodetector. *IEEE Trans. Electron Devices* **2021**, *68*, 144–151.
141. Li, S.; Yan, Z.Y.; Tang, J.C.; Yue, J.Y.; Liu, Z.; Li, P.G.; Guo, Y.F.; Tang, W.H. Ga<sub>2</sub>O<sub>3</sub>/V<sub>2</sub>O<sub>5</sub> Oxide Heterojunction Photovoltaic Photodetector With Superhigh Solar-Blind Spectral Discriminability. *IEEE Trans. Electron Devices* **2022**, *69*, 2443–2448. [[CrossRef](#)]
142. Yu, J.; Yu, M.; Wang, Z.; Yuan, L.; Huang, Y.; Zhang, L.; Zhang, Y.; Jia, R. Improved Photoresponse Performance of Self-Powered beta-Ga<sub>2</sub>O<sub>3</sub>/NiO Heterojunction UV Photodetector by Surface Plasmonic Effect of Pt Nanoparticles. *IEEE Trans. Electron Devices* **2020**, *67*, 3199–3204. [[CrossRef](#)]
143. Huang, L.; Hu, Z.; Zhang, H.; Xiong, Y.; Fan, S.; Kong, C.; Li, W.; Ye, L.; Li, H. A simple, repeatable and highly stable self-powered solar-blind photoelectrochemical-type photodetector using amorphous Ga<sub>2</sub>O<sub>3</sub> films grown on 3D carbon fiber paper. *J. Mater. Chem. C* **2021**, *9*, 10354–10360. [[CrossRef](#)]
144. Wang, Y.; Li, L.; Wang, H.; Su, L.; Chen, H.; Bian, W.; Ma, J.; Li, B.; Liu, Z.; Shen, A. An ultrahigh responsivity self-powered solar-blind photodetector based on a centimeter-sized β-Ga<sub>2</sub>O<sub>3</sub>/polyaniline heterojunction. *Nanoscale* **2020**, *12*, 1406–1413. [[CrossRef](#)]
145. Bundy, F.P.; Hall, H.T.; Strong, H.M.; Wentorf, R.H. Man-Made Diamonds. *Nature* **1955**, *176*, 51–55. [[CrossRef](#)]
146. Derjaguin, B.; Fedoseev, D.; Lukyanovich, V.; Spitzin, B.; Ryabov, V.; Lavrentyev, A. Filamentary diamond crystals. *J. Cryst. Growth* **1968**, *2*, 380–384. [[CrossRef](#)]
147. Angus, J.C.; Will, H.A.; Stanko, W.S. Growth of Diamond Seed Crystals by Vapor Deposition. *J. Appl. Phys.* **1968**, *39*, 2915–2922. [[CrossRef](#)]
148. Wang, S.F.; Li, D.M.; Xiao, Y.H.; Yang, Z.C.; Li, J.P.; Hao, J. Diamond Radiation Detector Used for Space Radiation Detection: A State-of-Art Review. *Mater. Rev.* **2018**, *32*, 1459–1468.
149. Alvarez, J.; Liao, M.; Koide, Y. Large deep-ultraviolet photocurrent in metal-semiconductor-metal structures fabricated on as-grown boron-doped diamond. *Appl. Phys. Lett.* **2005**, *87*, 113507. [[CrossRef](#)]
150. Liao, M.; Koide, Y. High-performance metal-semiconductor-metal deep-ultraviolet photodetectors based on homoepitaxial diamond thin film. *Appl. Phys. Lett.* **2006**, *89*, 113509. [[CrossRef](#)]
151. Bevilacqua, M.; Jackman, R.B. Extreme sensitivity displayed by single crystal diamond deep ultraviolet photoconductive devices. *Appl. Phys. Lett.* **2009**, *95*, 243501. [[CrossRef](#)]
152. Koide, Y.; Liao, M.; Imura, M. Mechanism of photoconductivity gain and persistent photoconductivity for diamond photodetector. *Diam. Relat. Mater.* **2010**, *19*, 205–207. [[CrossRef](#)]
153. Mendoza, F.; Makarov, V.; Weiner, B.R.; Morell, G. Solar-blind field-emission diamond ultraviolet detector. *Appl. Phys. Lett.* **2015**, *107*, 201605. [[CrossRef](#)]
154. Feng, M.; Jin, P.; Meng, X.; Xu, P.; Huo, X.; Zhou, G.; Qu, P.; Wu, J.; Wang, Z. Performance of metal-semiconductor-metal structured diamond deep-ultraviolet photodetector with a large active area. *J. Phys. D Appl. Phys.* **2022**, *55*, 404005. [[CrossRef](#)]

155. Girolami, M.; Serpente, V.; Mastellone, M.; Tardocchi, M.; Rebai, M.; Xiu, Q.; Liu, J.; Sun, Z.; Zhao, Y.; Valentini, V.; et al. Self-powered solar-blind ultrafast UV-C diamond detectors with asymmetric Schottky contacts. *Carbon* **2022**, *189*, 27–36. [[CrossRef](#)]
156. Liao, M.; Alvarez, J.; Imura, M.; Koide, Y. Submicron metal-semiconductor-metal diamond photodiodes toward improving the responsivity. *Appl. Phys. Lett.* **2007**, *91*, 163510. [[CrossRef](#)]
157. Liu, K.; Liu, B.; Zhao, J.; Shu, G.; Xu, X.; Yao, K.; Sun, M.; Zhang, X.; Yang, Y.; Su, Z.; et al. Application of back bias to interdigital-electrode structured diamond UV detector showing enhanced responsivity. *Sensors Actuators A Phys.* **2019**, *290*, 222–227. [[CrossRef](#)]
158. Wang, S.G.; Sellin, P.J.; Lohstroh, A.; Zhang, Q. Performance improvement of polycrystalline diamond ultraviolet photodetectors by room-temperature plasma treatment. *Appl. Phys. Lett.* **2005**, *86*, 093503. [[CrossRef](#)]
159. Liu, Z.; Zhao, D.; Min, T.; Wang, J.; Chen, G.; Wang, H.-X. Photovoltaic Three-Dimensional Diamond UV Photodetector With Low Dark Current and Fast Response Speed Fabricated by Bottom-Up Method. *IEEE Electron Device Lett.* **2019**, *40*, 1186–1189. [[CrossRef](#)]
160. Liu, K.; Dai, B.; Ralchenko, V.; Xia, Y.; Quan, B.; Zhao, J.; Shu, G.; Sun, M.; Gao, G.; Yang, L.; et al. Single crystal diamond UV detector with a groove-shaped electrode structure and enhanced sensitivity. *Sens. Actuators A Phys.* **2017**, *259*, 121–126. [[CrossRef](#)]
161. Liu, Z.; Zhao, D.; Min, T.; Wang, H. 3D TiO<sub>2</sub>/Diamond Ultraviolet Detector Using Back-to-Back Pd Schottky Electrode. *Phys. Status Solidi A-Appl. Mater. Sci.* **2020**, *217*, 2000218. [[CrossRef](#)]
162. Forneris, J.; Giudice, A.L.; Olivero, P.; Picollo, F.; Re, A.; Marinelli, M.; Pompili, F.; Verona, C.; Rinati, G.V.; Benetti, M.; et al. A 3-dimensional interdigitated electrode geometry for the enhancement of charge collection efficiency in diamond detectors. *EPL Europhys. Lett.* **2014**, *108*, 18001. [[CrossRef](#)]
163. Lin, C.-N.; Lu, Y.-J.; Yang, X.; Tian, Y.-Z.; Gao, C.-J.; Sun, J.-L.; Dong, L.; Zhong, F.; Hu, W.-D.; Shan, C.-X. Diamond-Based All-Carbon Photodetectors for Solar-Blind Imaging. *Adv. Opt. Mater.* **2018**, *6*, 1800068. [[CrossRef](#)]
164. Liao, M.; Sang, L.; Teraji, T.; Imura, M.; Alvarez, J.; Koide, Y. Comprehensive Investigation of Single Crystal Diamond Deep-Ultraviolet Detectors. *Jpn. J. Appl. Phys.* **2012**, *51*, 090115. [[CrossRef](#)]
165. Salvatori, S.; Pace, E.; Rossi, M.; Galluzzi, F. Photoelectrical characteristics of diamond UV detectors: Dependence on device design and film quality. *Diam. Relat. Mater.* **1997**, *6*, 361–366. [[CrossRef](#)]
166. Liao, M.; Koide, Y.; Alvarez, J. Single Schottky-barrier photodiode with interdigitated-finger geometry: Application to diamond. *Appl. Phys. Lett.* **2007**, *90*, 123507. [[CrossRef](#)]
167. Čermák, J.; Koide, Y.; Takeuchi, D.; Rezek, B. Spectrally dependent photovoltages in Schottky photodiode based on (100) B-doped diamond. *J. Appl. Phys.* **2014**, *115*, 053105. [[CrossRef](#)]
168. Liao, M.; Wang, X.; Teraji, T.; Koizumi, S.; Koide, Y. Light intensity dependence of photocurrent gain in single-crystal diamond detectors. *Phys. Rev. B* **2010**, *81*, 033304. [[CrossRef](#)]
169. Mohapatra, S.; Sahu, P.; Rath, S.; Sahoo, P.K.; Varma, S.; Murty, N.N. Impact of nitrogen induced defect dynamics on UV response of diamond photodetectors. *Superlattices Microstruct.* **2020**, *142*, 106504. [[CrossRef](#)]
170. Liu, B.; Liu, K.; Zhang, S.; Ralchenko, V.G.; Zhang, X.; Xue, J.; Wen, D.; Qiao, P.; Zhao, J.; Dai, B.; et al. Self-Powered Solar-Blind UV Detectors Based on O-Terminated Vertical Diamond Schottky Diode with Low Dark Current, High Detectivity, and High Signal-to-Noise Ratio. *ACS Appl. Electron. Mater.* **2022**, *4*, 5996–6003. [[CrossRef](#)]
171. Liu, Z.; Lin, F.; Zhao, D.; Min, T.; Wang, H. Fabrication and Characterization of (100)-Oriented Single-Crystal Diamond p-i-n Junction Ultraviolet Detector. *Phys. Status Solidi Appl. Mater. Sci.* **2020**, *217*, 2000207. [[CrossRef](#)]
172. Ge, L.; Peng, Y.; Wang, X.; Wang, D.; Xu, M.; Xu, X. Diamond Metal-Semiconductor Field-Effect-Transistor-based Solar Blind Detector. In Proceedings of the 2021 18th China International Forum on Solid State Lighting & 2021 7th International Forum on Wide Bandgap Semiconductors, Shenzhen, China, 6–8 December 2021.
173. Wei, M.; Yao, K.; Liu, Y.; Yang, C.; Zang, X.; Lin, L. A Solar-Blind UV Detector Based on Graphene-Microcrystalline Diamond Heterojunctions. *Small* **2017**, *13*, 1701328. [[CrossRef](#)]
174. Zkria, A.; Gima, H.; Yoshitake, T. Application of nitrogen-doped ultrananocrystalline diamond/hydrogenated amorphous carbon composite films for ultraviolet detection. *Appl. Phys. A* **2017**, *123*, 115102. [[CrossRef](#)]
175. Chen, Y.C.; Lu, Y.J.; Lin, C.N.; Tian, Y.Z.; Gao, C.J.; Dong, L.; Shan, C.X. Self-powered diamond/ $\beta$ -Ga<sub>2</sub>O<sub>3</sub> photodetectors for solar-blind imaging. *J. Mater. Chem. C* **2018**, *6*, 5727–5732. [[CrossRef](#)]
176. Liu, Z.C.; Li, F.; Wang, W.; Zhang, J.W.; Lin, F.; Wang, H.X. Effect of depth of Buried-In Tungsten Electrodes on Single Crystal Diamond Photodetector. *MRS Adv.* **2016**, *1*, 1099–1104. [[CrossRef](#)]

**Disclaimer/Publisher’s Note:** The statements, opinions and data contained in all publications are solely those of the individual author(s) and contributor(s) and not of MDPI and/or the editor(s). MDPI and/or the editor(s) disclaim responsibility for any injury to people or property resulting from any ideas, methods, instructions or products referred to in the content.